The taste of new physics: Flavour violation from TeV-scale phenomenology to Grand Unification

Björn Herrmann

The taste of new physics: Flavour violation from TeV-scale phenomenology to Grand Unification

Habilitation thesis presented by

Dr. BJÖRN HERRMANN

Laboratoire d'Annecy-le-Vieux de Physique Théorique
Communauté Université Grenoble Alpes
Université Savoie Mont Blanc – CNRS

and publicly defended on

JUNE 12, 2019

before the examination committee composed of

Dr.	GENEVIÈVE BÉLANGER	CNRS Annecy	President
Dr.	SACHA DAVIDSON	CNRS Montpellier	Examiner
Prof.	ALDO DEANDREA	Univ. Lyon	Referee
Prof.	ULRICH ELLWANGER	Univ. Paris-Saclay	Referee
Dr.	SABINE KRAML	CNRS Grenoble	Examiner
Prof.	FABIO MALTONI	Univ. Catholique de Louvain	Referee

July 12, 2019

"We shall not cease from exploration, and the end of all our exploring will be to arrive where we started and know the place for the first time."

T. S. Eliot

Abstract

The present manuscript, submitted as Habilitation Thesis in view of the *Habilitation à diriger la recherche*, presents an important part of my recent and current research work on the possibility of Non-Minimal Flavour Violation within supersymmetric theories.

The first part of this manuscript contains an introduction to the concept of flavour and its description, first within the Standard Model of particle physics, then in theories beyond the latter. A dedicated discussion of the Minimal Supersymmetric Standard Model (MSSM) allows to introduce the framework of Non-Minimal Flavour Violation.

The second part of this manuscript is composed of a selection of published work to which I have significantly contributed mainly between 2013 and 2018. I review in particuler work on experimental signatures of Non-Minimal Flavour Violation in the squark sector of the MSSM. In addition, I discuss the implementation of Non-Minimal Flavour Violation within Grand Unified frameworks including flavour symmetries.

In the third and last part of this manuscript, I briefly discuss ongoing and future projects, to be understood as perspectives stemming from the presented published work.

To all who have contributed – in whatever way – to this manuscript.

Acknowledgements

I would like to start by expressing my gratitude to the members of the examination committee for having accepted to evaluate the present manuscript and to participate to the habilitation defence. I am particularly thankful for the fruitful exchanges that we have had around this manuscript and the associated presentation.

Second, I have to thank my collaborators, including the students, for the enriching and fruitful work on our common projects, presented in this manuscript and beyond. Without our numerous discussions and exchange of knowledge, the presented results could not have been achieved and working in research would not be so much fun. Moreover, I am grateful for their kindness together with the relaxed and pleasant working atmosphere within the different collaborations.

Moreover, I am grateful to my colleagues at *Laboratoire d'Annecy-le-Vieux de Physique Théorique* for the inspiring working conditions and the pleasant atmosphere. I particularly acknowledge Fawzi Boudjema and Luc Frappat, successive directors of the institute, for their constant support of my activities and the preparation of my habilitation. Special thanks go to our admistrative team, Dominique Turc, Véronique Jonnery, and Virginie Malaval, for their availability, support, efficiency, and kindness.

Finally, I would like to thank my university colleagues, most of them not working in the same discipline, for their interest in my work, their support, and the numerous discussions about physics and life.

Last but not least, I thank my beloved wife Aurélie, who has been at my side during my whole research career, constantly inspiring me with her sympathy, her support, her curiosity, her humour, her zest for life, and, above all, her love.

Contents

Chapter 1

Flavour violation in particle physics

In elementary particle physics, the concept of *flavour* allows to classify the elementary particles. More precisely, flavour is orthogonal to the arrangement of elementary matter fields into *quarks* and *leptons*. There are three generations of matter fields, meaning that there are three flavours of up-type quarks (up, charm, top), down-type quarks (down, strange, bottom), charged leptons (electron, muon, tau), and neutrinos (associated to the three leptons). It is important to note that the physical eigenstates are not necessarily flavour eigenstates of the theory, meaning that a physical particle may carry more than one flavour. This is the central topic of the work presented in this manuscript.

This first Chapter is dedicated to a discussion of flavour, first within the Standard Model of particle physics, then within supersymmetric extensions of the latter. Particular attention will be paid to the concepts of *Minimal Flavour Violation* (MFV) as opposed to *Non-Minimal Flavour Violation* (NMFV). The latter will be at the centre of the present manuscript.

1.1 Flavour in the Standard Model

The Standard Model of particle physics [1, 2, 3, 4, 5, 6, 7] describes the subatomic particles known at present. It is based on the gauge group $SU(3)_C \times SU(2)_L \times U(1)_Y$, the three factors being relative to the strong, weak, and electromagnetic interactions, respectively. The associated gauge bosons are the gluon, denoted g, the W- and Z-bosons, denoted $W^{\pm}$ and Z^0, and the photon, denoted γ.

Matter is encompassed in the fermionic fields

$$\begin{aligned} q_L &= \begin{pmatrix} u_L \\ d_L \end{pmatrix}, \qquad u_R\,,\, d_R\,, \\ \ell_L &= \begin{pmatrix} \nu_L \\ e_L \end{pmatrix}, \qquad e_R\,, \end{aligned} \tag{1.1}$$

where $u^{(i)} = (u, c, t)$ contains the three up-type quark flavour eigenstates, $d^{(i)} = (d, s, b)$ the three down-type quark flavour eigenstates, $e^{(i)} = (e, \mu, \tau)$ the three lepton flavour eigenstates, and $\nu^{(i)} = (\nu_e, \nu_\mu, \nu_\tau)$ the three neutrino flavour eigenstates. The indices L and R refer to the chirality of the respective fermions. Moreover, the left-handed fields q_L and ℓ_L are $SU(2)$ doublets, while the right-handed fields are $SU(2)$ singlets. Note that, although the observation of neutrino oscillations [8, 9, 10, 11, 12, 13, 14, 15, 16, 17, 18, 19, 20, 21, 22] strongly suggests their existence, right-handed neutrinos are not part of the Standard Model particle content. The fermionic matter fields together with their quantum numbers regarding the strong, weak, and electromagnetic interactions, are summarized in Table 1.1.

	B	L	T	T_3	Y	Q
u_L	1/3	0	1/2	+1/2	1/3	2/3
d_L	1/3	0	1/2	-1/2	1/3	-1/3
u_R	1/3	0	0	0	4/3	2/3
d_R	1/3	0	0	0	-2/3	-1/3
ν_L	0	1	1/2	+1/2	1	0
e_L	0	1	1/2	-1/2	1	-1
e_R	0	1	0	0	-2	-1

TABLE 1.1: Quantum numbers of the fermions in the Standard Model of particle physics. B and L denote baryon and lepton numbers, T and T_3 refer to weak isospin, Y denotes weak hypercharge, and $Q = T_3 + Y/2$ is the electric charge.

The theory is completed by the complex scalar Higgs field [23, 24, 25, 26, 27, 28]

$$H = \begin{pmatrix} H^+ \\ H^0 \end{pmatrix} \quad \longrightarrow \quad H = \begin{pmatrix} G^+ \\ \frac{1}{\sqrt{2}}\left(v + h^0 + iG^0\right) \end{pmatrix}, \tag{1.2}$$

where the last part corresponds to the expansion of the neutral component around the vacuum expectation value $\langle H \rangle = v/\sqrt{2} \approx 174\,\text{GeV}$ upon electroweak symmetry breaking. The physical degree of freedom h^0, the so-called Higgs-boson[1], has been experimentally discovered by the ATLAS and CMS collaborations at the *Large Hadron Collider* [29, 30].

The matter fields acquire mass through the Yukawa interaction with the Higgs field. In the interaction eigenbasis, the corresponding Lagrangian reads

$$\mathcal{L}^{\text{SM}}_{\text{Yuk}} = \frac{v}{\sqrt{2}} \bar{u}^{(i)}_L Y_u u^{(i)}_R H + \frac{v}{\sqrt{2}} \bar{d}^{(i)}_L Y_d d^{(i)}_R H + \frac{v}{\sqrt{2}} \bar{\ell}^{(i)}_L Y_e \ell^{(i)}_R H\,, \tag{1.3}$$

where Y_u, Y_d, and Y_ℓ are the Yukawa matrices for up-type quarks, down-type quarks, and leptons, respectively. As they are strictly massless in the Standard Model, Eq. (1.3) does not contain a Yukawa term for the neutrinos.

The Higgs boson acquiring its vacuum expectation value leads to Dirac mass terms for the quarks and leptons. The corresponding mass matrices are given by

$$M^{(i)}_u = \frac{v}{\sqrt{2}} Y_u\,, \qquad M^{(i)}_d = \frac{v}{\sqrt{2}} Y_d\,, \qquad M^{(i)}_e = \frac{v}{\sqrt{2}} Y_e\,. \tag{1.4}$$

The quarks, leptons, and neutrinos interact with the gauge bosons of the electromagnetic, weak, and strong interactions. In terms of the fields defined in Eq. (1.1), i.e. in the interaction eigenbasis, the Lagrangian decribing the interaction of quarks and charged leptons with the photon A^0 reads

$$\mathcal{L}^{\text{SM}}_{ffA} = g_e \bar{q}^{(i)}_L \gamma_\mu q^{(i)}_L A^0_\mu + g_e \bar{u}^{(i)}_R \gamma_\mu u^{(i)}_R A^0_\mu + g_e \bar{d}^{(i)}_R \gamma_\mu d^{(i)}_R A^0_\mu + g_e \bar{e}^{(i)}_L \gamma_\mu e^{(i)}_L A^0_\mu + g_e \bar{e}^{(i)}_R \gamma_\mu e^{(i)}_R A^0_\mu\,, \tag{1.5}$$

where $g_e = eQ$ relates to the elementary charge e and the electric charge Q of the interacting fermion. The Lagrangian decribing the neutral-current interaction of quarks, charged leptons,

[1] Throughout the present manuscript I shall use the common name "Higgs field" and "Higgs boson", keeping in mind that a more correct name would be "Brout-Englert-Higgs field" and "Brout-Englert-Higgs" boson.

and neutrinos with the Z^0-boson reads

$$\mathcal{L}^{\rm SM}_{ffZ} = g_Z \bar{q}^{(i)}_L \gamma_\mu q^{(i)}_L Z^0_\mu + g_Z \bar{u}^{(i)}_R \gamma_\mu u^{(i)}_R Z^0_\mu + g_Z \bar{d}^{(i)}_R \gamma_\mu d^{(i)}_R Z^0_\mu + g_Z \bar{\ell}^{(i)}_L \gamma_\mu \ell^{(i)}_L Z^0_\mu + g_Z \bar{e}^{(i)}_R \gamma_\mu e^{(i)}_R Z^0_\mu \,, \tag{1.6}$$

the couplings constant $g_Z = g/\cos\theta_W$ being related to the weak coupling constant g and the weak mixing angle. Coming to the charged current interactions with the $W^\pm$-boson, the Lagrangian is given by

$$\mathcal{L}^{\rm SM}_{ffW} = g_W \bar{u}^{(i)}_L \gamma_\mu d^{(i)}_L W^+_\mu + g_W \bar{e}^{(i)}_L \gamma_\mu \nu^{(i)}_L W^+_\mu + \text{h.c.}\,, \tag{1.7}$$

where $g_W = g/\sqrt{2}$. Finally, the Lagrangian corresponding to the strong interaction of quarks with gluons g reads

$$\mathcal{L}^{\rm SM}_{qqg} = g_s T^a \bar{q}^{(i)}_L \gamma_\mu q^{(i)}_L g^a_\mu + g_s T^a \bar{u}^{(i)}_R \gamma_\mu u^{(i)}_R g^a_\mu + g_s T^a \bar{d}^{(i)}_R \gamma_\mu d^{(i)}_R g^a_\mu \,, \tag{1.8}$$

where g_s denotes the strong coupling constant, and T the colour matrices. For the sake of readibility, flavour and colour indices of the fermions have been omitted in the above equations, allowing to focus on the structure of the interaction terms.

In the following, I will discuss the sectors of quarks and leptons (including neutrinos) separately. For each sector, I will present the rotation to the basis of physical (i.e. mass) eigenstates, as well as the consequences of this rotation on the above interactions.

Quark sector

In order to obtain the quark mass eigenvalues and corresponding physical eigenstates, the above matrices $M^{(i)}_u$ and $M^{(i)}_d$, given in the interaction eigenbasis, have to be diagonalized. Given the structure of the Yukawa Lagrangian of Eq. (1.3), this is achieved by introducing four unitary rotation matrices, associated to the left- and right-handed up- and down-type quarks, such that

$$\begin{aligned} u^{(i)}_L &= V_{uL} u^{(m)}_L \,, \qquad & u^{(i)}_R &= V_{uR} u^{(m)}_R \,, \\ d^{(i)}_L &= V_{dL} d^{(m)}_L \,, \qquad & d^{(i)}_R &= V_{dR} d^{(m)}_R \,. \end{aligned} \tag{1.9}$$

Here, the introduced superscript (m) refers to the basis of physical mass eigenstates, as opposed to the interaction eigenstates carrying superscript (i). The corresponding rotation of the mass matrices of Eq. (1.4) occurs according to

$$M^{(m)}_u = \text{diag}\,(m_u, m_c, m_t) = V^\dagger_{uL} M^{(i)}_u V_{uR} \,, \tag{1.10}$$

$$M^{(m)}_d = \text{diag}\,(m_d, m_s, m_b) = V^\dagger_{dL} M^{(i)}_d V_{dR} \,. \tag{1.11}$$

Here, m_u, m_d, m_c, m_s, m_t, and m_b, denote the physical masses of the up, down, charm, strange, top, and bottom quarks, respectively.

Rotating the fields as in Eq. (1.9) leaves the corresponding parts of the Lagrangian parts associated to neutral current interactions invariant. More precisely, all occurencies of the rotation matrices vanish due to their unitarity, and we obtain for the interaction of quarks with the

photon, Z-boson, and gluon,

$$\begin{aligned}\mathcal{L}^{\text{SM}}_{qqA} &= g_e \bar{q}^{(m)}_L \gamma_\mu q^{(m)}_L A^0_\mu + g_e \bar{u}^{(m)}_R \gamma_\mu u^{(m)}_R A^0_\mu + g_e \bar{d}^{(m)}_R \gamma_\mu d^{(m)}_R A^0_\mu \,, \\ \mathcal{L}^{\text{SM}}_{qqZ} &= g_Z \bar{q}^{(m)}_L \gamma_\mu q^{(m)}_L Z^0_\mu + g_Z \bar{u}^{(m)}_R \gamma_\mu u^{(m)}_R Z^0_\mu + g_Z \bar{d}^{(m)}_R \gamma_\mu d^{(m)}_R Z^0_\mu \,, \\ \mathcal{L}^{\text{SM}}_{qqg} &= g_s T^a \bar{q}^{(m)}_L \gamma_\mu q^{(m)}_L g^a_\mu + g_s T^a \bar{u}^{(m)}_R \gamma_\mu u^{(m)}_R g^a_\mu + g_s T^a \bar{d}^{(m)}_R \gamma_\mu d^{(m)}_R g^a_\mu \,.\end{aligned} \tag{1.12}$$

In contrast, after rotation of the charged-current interaction into the mass eigenbasis, the product of the two involved rotation matrices does not vanish in the Lagrangian,

$$\mathcal{L}^{\text{SM}}_{qqW} \;=\; g_W \bar{u}^{(m)}_L V^\dagger_{uL} V_{dL} \gamma^\mu d^{(m)}_L W^+_\mu \;\equiv\; g_W \bar{u}^{(m)}_L V_{\text{CKM}} \gamma^\mu d^{(m)}_L W^+_\mu \,, \tag{1.13}$$

and defines the *Cabbibo-Kobayashi-Maskawa* (CKM) matrix [31, 32],

$$\boxed{V_{\text{CKM}} \;=\; V^\dagger_{uL} V_{dL} \,.} \tag{1.14}$$

The CKM-matrix expresses the misalignment between the rotations of the left-handed up- and down-type sectors and allows thus for flavour-changing charged current interactions between up- and down-type quarks. More precisely, the transition of an up-type quark u_i ($i = 1,2,3$) to a down-type quark d_j ($j = 1,2,3$) is governed by the corresponding element $(V_{\text{CKM}})_{ij}$ of the CKM-matrix.

The CKM-matrix possesses four degrees of freedom and can be parametrized in various ways. One way is writing it in terms of three Euler angles θ_{12}, θ_{13}, and θ_{23}, plus one additional phase δ_{13},

$$V_{\text{CKM}} \;=\; \begin{pmatrix} 1 & 0 & 0 \\ 0 & c_{23} & s_{23} \\ 0 & -s_{23} & c_{23} \end{pmatrix} \begin{pmatrix} c_{13} & 0 & s_{13} e^{-i\delta_{13}} \\ 0 & 1 & 0 \\ -s_{13} e^{i\delta_{13}} & 0 & c_{13} \end{pmatrix} \begin{pmatrix} c_{12} & s_{12} & 0 \\ -s_{12} & c_{12} & 0 \\ 0 & 0 & 1 \end{pmatrix} . \tag{1.15}$$

Here, $s_{ij} = \sin\theta_{ij}$ and $c_{ij} = \cos\theta_{ij}$ for $i,j = 1,2,3$, and the angles can be chosen such that $0 \leq \theta_{ij} \leq \pi/2$. While the three angles correspond to the couplings between the respective generations, the phase δ_{13} is responsible for CP-violation. A second, approximate but rather illustrative, way of parametrizing the CKM-matrix is the Wolfenstein parametrization [33],

$$V_{\text{CKM}} \;=\; \begin{pmatrix} 1 - \frac{1}{2}\lambda^2 & \lambda & A\lambda^3(\rho - i\eta) \\ -\lambda & 1 - \frac{1}{2}\lambda^2 & A\lambda^2 \\ A\lambda^3(1 - \rho - i\eta) & \mathcal{O}(\lambda^2) & 1 \end{pmatrix} \approx \begin{pmatrix} 1 - \mathcal{O}(\lambda^2) & \mathcal{O}(\lambda) & \mathcal{O}(\lambda^3) \\ \mathcal{O}(\lambda) & 1 - \mathcal{O}(\lambda^2) & \mathcal{O}(\lambda^2) \\ \mathcal{O}(\lambda^3) & \mathcal{O}(\lambda^2) & 1 \end{pmatrix} , \tag{1.16}$$

where terms of order λ^4 and higher have been omitted.

Experimentally, the absolute values of the elements of the CKM-matrix are determined to the values given in Table 1.2. This leads to the value of $\lambda \approx 0.22$ in the Wolfenstein parametrization. The approximate expression in Eq. (1.16) exhibites the hierarchical structure of the CKM-matrix, flavour-violating transitions being most important between the first and second generations, and least relevant between the first and third generations. The same can be seen when translating the values of Table 1.2 into the Euler angles, which leads to

$$\sin\theta_{12} \approx 13.0^\circ \,, \quad \sin\theta_{23} \approx 2.4^\circ \,, \quad \sin\theta_{13} \approx 0.2^\circ \,, \tag{1.17}$$

while the CP-violating phase is approximated to $\delta_{13} \approx 1.2^\circ$. As the present manuscript focuses on in flavour violation, but not CP-violation, a more detailed discussion of the latter is not

$\left\|\left(V_{\mathrm{CKM}}\right)_{11}\right\| = \left\|\left(V_{\mathrm{CKM}}\right)_{ud}\right\|$	0.97420 ± 0.00021	[34]
$\left\|\left(V_{\mathrm{CKM}}\right)_{12}\right\| = \left\|\left(V_{\mathrm{CKM}}\right)_{us}\right\|$	0.2243 ± 0.0005	[35]
$\left\|\left(V_{\mathrm{CKM}}\right)_{13}\right\| = \left\|\left(V_{\mathrm{CKM}}\right)_{ub}\right\|$	$(3.94 \pm 0.36) \cdot 10^{-3}$	[35]
$\left\|\left(V_{\mathrm{CKM}}\right)_{21}\right\| = \left\|\left(V_{\mathrm{CKM}}\right)_{cd}\right\|$	0.218 ± 0.004	[35]
$\left\|\left(V_{\mathrm{CKM}}\right)_{22}\right\| = \left\|\left(V_{\mathrm{CKM}}\right)_{cs}\right\|$	0.997 ± 0.017	[35]
$\left\|\left(V_{\mathrm{CKM}}\right)_{23}\right\| = \left\|\left(V_{\mathrm{CKM}}\right)_{cb}\right\|$	$(42.2 \pm 0.8) \cdot 10^{-3}$	[36]
$\left\|\left(V_{\mathrm{CKM}}\right)_{31}\right\| = \left\|\left(V_{\mathrm{CKM}}\right)_{td}\right\|$	$(8.1 \pm 0.5) \cdot 10^{-3}$	[35]
$\left\|\left(V_{\mathrm{CKM}}\right)_{32}\right\| = \left\|\left(V_{\mathrm{CKM}}\right)_{ts}\right\|$	$(39.4 \pm 2.3) \cdot 10^{-3}$	[35]
$\left\|\left(V_{\mathrm{CKM}}\right)_{33}\right\| = \left\|\left(V_{\mathrm{CKM}}\right)_{tb}\right\|$	1.019 ± 0.025	[35]

TABLE 1.2: Experimentally determined absolute values of the elements of the CKM matrix as given in Ref. [35].

pursued here.

Lepton and neutrino sector

In the same way as discussed above for the quarks, the lepton mass eigenvalues are obtained by diagonalizing the lepton mass matrix $M_e^{(i)}$, which leads to two rotations from the interaction eigenbasis, denoted (i), to the mass eigenbasis, denoted (m), for the left- and right-handed leptons,

$$e_L^{(i)} \;=\; V_{eL} e_L^{(m)}\,, \qquad e_R^{(i)} \;=\; V_{eR} e_R^{(m)}\,. \tag{1.18}$$

The corresponding transformation of the mass matrix reads

$$M_e^{(m)} \;=\; \mathrm{diag}\left(m_e, m_\mu, m_\tau\right) \;=\; V_{eL}^\dagger M_e^{(i)} V_{eR}\,, \tag{1.19}$$

where m_e, m_μ, and m_τ are the physical electron, muon, and tau masses.

In the absence of corresponding mass terms, the physical neutrino eigenstates correspond to the interaction eigenstates. Neutrino mixing in extensions of the Standard Model will be discussed in the following Section.

1.2 Extending the Standard Model

Although the Standard Model described in the previous Section succesfully describes an impressively wide range of phenomena related to matter and its interactions, there are strong reasons to believe that the Standard Model as such is incomplete, and should rather be seen as the low-energy limit of a more fundamental or more complete framework.

The most important evidences for such new physics arise from experimental evidence. The strongest hint towards extensions of the Standard Model is undoubtedly the presence of *dark matter* in our Universe. After first observational hints manifesting through gravitational effects [37, 38, 39] there is now rather precise knowledge of the energy content of the Universe. In particular, thanks to the subsequent cosmological probes *COBE* [40], *WMAP* [41, 42, 43, 44, 45], and *Planck* [46, 47, 48], it is well established that non-baryonic dark matter accounts for about 15% of the matter density, and for about 4.9% of the total energy density. More precisely, within

the ΛCDM model, the abundance of non-baryonic cold dark matter (CDM) is constrained to the rather narrow interval [48]

$$\Omega_{\text{CDM}}h^2 \;=\; 0.1200 \pm 0.0012\,, \tag{1.20}$$

h expressing the present Hubble expansion rate in units of $100\,\text{km}\,\text{s}^{-1}\,\text{Mpc}^{-1}$. As the Standard Model does not include a suitable candidate particle for cold dark matter, this clearly calls for physics beyond the Standard Model of particle physics.

The second experimental evidence for physics beyond the Standard Model stems from the neutrino sector. More precisely, there is compelling evidence for neutrino oscillations [8, 9, 11, 12, 13, 13, 14, 15, 16, 17, 18, 19, 20, 21, 22], meaning that the physical neutrino states carry different flavours. This in turn leads to the conclusion that neutrinos must be massive, in contradiction to their description in the Standard Model alone, where they cannot acquire a Dirac mass through the Higgs mechanism. The implementation of neutrino masses is discussed below. However, this mechanism cannot be achieved without introducing new physics.

In addition, several shortcomings of the Standard Model arise on the theory side. There is, e.g., the so-called "hierarchy problem" related to the mass of the Higgs boson. In the Standard Model alone, the fermionic correction to the Higgs mass contains a quadratic divergence, which either needs to be cancelled by some mechanism stemming from outside the Standard Model, or by extreme fine-tuning, which is unattractive from the natural point of view.

Moreover, the indication that the three gauge couplings, when evolved towards high energy scales through renormalizatoin group running, do not precisely meet at one energy scale, but take similar values around a scale of 10^{15} GeV, hints towards *Grand Unification* at a scale close to this value. The presence of additional fields in the beta-functions may improve the situation such that the three couplings "meet" with better precision at a high scale.

Finally, there is the so-called *flavour problem*, meaning that the Standard Model does not explain why there are three generations of matter fields, and more important, does not explain the observed hierarchy of the fermion masses. This question may be addressed by including, e.g., flavour symmetries in the theory.

The theories seeking to address the shortcomings of the Standard Model mentioned above are numerous. While rather simple extensions such as the singlet scalar [49, 50, 51] or inert doublet [52, 53] model, to name only a few, are based on additional scalar fields to include a dark matter candidate, other theories rely on more fundamental principles such as additional space-time dimensions or additional symmetries with respect to the Standard Model [54, 55]. Before discussing in more detail such a framework, namely the *Minimal Supersymmetric Standard Model* (MSSM), I shall proceed with a general discussion of the flavour structure of theories beyond the Standard Model.

The neutrino sector

Although the neutrinos are strictly massless in the Standard Model, as they do not allow for Yukawa interactions as in Eq. (1.3), it is apparent that there must be some mechanism generating masses for the left-handed neutrinos. In the simplest form, this manifests as a Majorana mass term,

$$-\mathcal{L}_\nu \;=\; \frac{1}{2}\bar{\nu}_L^{(i)} M_\nu^{(i)} \nu_L^{(i)} + \text{h.c.} \tag{1.21}$$

for the left-handed neutrinos. At this stage, the precise origin of the mass matrix is not discussed. Possible sources of neutrino mass terms can be, e.g., the Seesaw mechanism [56, 57, 58, 59, 60] or the radiative generation of neutrino masses [61, 62, 63]. The rotation of this term to

the neutrino mass eigenbasis invokes a rotation matrix according to

$$\nu_L^{(i)} = V_{\nu L}\nu_L^{(m)}\,, \tag{1.22}$$

$$M_\nu^{(m)} = \mathrm{diag}\,(m_{\nu_1}, m_{\nu_2}, m_{\nu_3}) = V_{\nu L}^\dagger M_\nu^{(i)} V_{\nu_L}\,, \tag{1.23}$$

where the mass eigenstates are denoted ν_1, ν_2, and ν_3.

Rewriting the interaction Lagrangian in the mass eigenbasis leads to the same conclusions as for the quarks, namely that neutral current interactions are unaffected by the introduced rotation matrices, but one product of rotation matrices remains in the charged current Lagrangian,

$$-\mathcal{L}_{\ell\nu W} = g_W \bar{e}_L^{(m)} V_{eL}^\dagger V_{\nu L}\gamma_\mu \nu_L^{(m)} W_\mu^+ + \text{h.c.} \equiv g_W \bar{e}_L^{(m)} V_{\text{PMNS}}\gamma_\mu \nu_L^{(m)} W_\mu^+ + \text{h.c.}\,. \tag{1.24}$$

This introduces the *Pontecorvo-Maki-Nakagawa-Sakata* (PMNS) matrix [9, 10],

$$\boxed{V_{\text{PMNS}} = V_{eL}^\dagger V_{\nu L}\,,} \tag{1.25}$$

which expresses the mismatch between the rotations of the left-handed charged leptons and the neutrinos. It is thus the equivalent to the CKM matrix in the quark sector. All charged-current interactions between left-handed leptons and neutrinos are related to the corresponding elements of the PMNS matrix.

If the lepton mass eigenstates are identified with their flavour eigenstates, as it is the case in the Standard Model, the lepton mixing matrices correspond to the identity. The PMNS matrix is thus identified directly with the neutrino mixing matrix, $V_{\text{PMNS}} = V_{\nu L}$. In the absence of neutrino masses, the PMNS matrix is also equivalent to the identity. This illustrates that the presence of lepton-flavour violating interactions is directly related to the fact that neutrinos are massive.

In the same way as the CKM matrix, the PMNS matrix can be parametrized through three mixing angles, ϑ_{12}, ϑ_{13}, and ϑ_{13}, associated to the transitions between the respective generations, plus CP-violating phases η_{12}, η_{23}, and η_{13}. Denoting $c_{ij} = \cos\vartheta_{ij}$ and $s_{ij} = \sin\vartheta_{ij}$ for $i, j = 1, 2, 3$, the PMNS matrix reads

$$V_{\text{PMNS}} = \begin{pmatrix} 1 & 0 & 0 \\ 0 & c_{23} & s_{23} \\ 0 & -s_{23} & c_{23} \end{pmatrix} \begin{pmatrix} c_{13} & 0 & s_{13}e^{-i\eta_{13}} \\ 0 & 1 & 0 \\ -s_{13}e^{i\eta_{13}} & 0 & c_{13} \end{pmatrix} \begin{pmatrix} c_{12} & s_{12} & 0 \\ -s_{12} & c_{12} & 0 \\ 0 & 0 & 1 \end{pmatrix} \begin{pmatrix} 1 & 0 & 0 \\ 0 & e^{i\eta_{12}} & 0 \\ 0 & 0 & e^{i\eta_{23}} \end{pmatrix}, \tag{1.26}$$

where $\eta_{12} = \eta_{23} = 0$ in the case of Dirac neutrinos, and η_{13} is the Dirac $CP-violating$ phase analogous to the phase δ_{13} of the CKM-matrix. As mentioned above, the physics related to CP-violation is beyond the scope of the present manuscript.

Assuming normal neutrino mass ordering, i.e. $m_{\nu 1} \leq m_{\nu_2} \leq m_{\nu 3}$, leads to the experimental determination of the angles

$$\vartheta_{12} \approx 33.6^\circ\,, \qquad \vartheta_{23} \approx 41.6^\circ\,, \qquad \vartheta_{23} \approx 8.5^\circ\,, \tag{1.27}$$

while the CP-violating phase is found to be $\eta_{13} \approx 261^\circ$ [64]. Assuming inverted mass hierarchy, $m_{\nu 1} \leq m_{\nu_3} \leq m_{\nu 2}$, leads to slightly different values. Comparing to the values given in Eq. (1.17), it becomes obvious that lepton mixing is generally more important and at the same time less hierarchical than quark mixing.

Minimal vs. Non-Minimal Flavour Violation

Coming back to the subject of flavour, considering extensions of the Standard Model, assumptions have to be made concerning the underlying flavour structure of the theory. The simplest assumption is that the flavour structure of the extended theory is the same as in the Standard without introducing additional sources of flavour violation. In other words, the Yukawa matrices remain the only source of flavour violation, and consequently all flavour-changing interactions are related to the CKM and PMNS matrices as discussed above. This is known as the *Minimal Flavour Violation* (MFV) paradigm [65].

An alternative assumption is to allow for additional sources of flavour violation when extending the Standard Model by new fields or symmetries. This means that, while the Yukawa matrices still induce flavour-changing charged currents related to the CKM and PMNS matrices, additional terms may be present in the Lagragian of the theory introducing additional contributions to flavour-changing interactions, including flavour-changing neutral currents. This defines the *Non-Minimal Flavour Violation* (NMFV) framework.

In the present manuscript, I mainly consider the framework of Non-Minimal Flavour Violation, in particular in supersymmetric theories. In the next Section, the Minimal Supersymmetric Standard Model (MSSM), including the implementation of flavour violation therein, will be discussed.

1.3 The Minimal Supersymmetric Standard Model

In the present manuscript, I will focus on Supersymmetry [54, 55], which is based on a link between bosonic and fermionic degrees of freedom. More precisely, the Poincaré algebra is extended by fermionic generators $\mathcal{Q}_\alpha$ relating bosonic and fermionic states,

$$\mathcal{Q}_\alpha \big|\text{boson}\big\rangle \;=\; \big|\text{fermion}\big\rangle\,, \qquad \mathcal{Q}_\alpha \big|\text{fermion}\big\rangle \;=\; \big|\text{boson}\big\rangle\,. \tag{1.28}$$

For phenomenological purposes, it is reasonable to assume only one fermionic generator. In this way, Supersymmetry provides a bosonic counterpart for each fermionic degree of freedom of the Standard Model, and a fermionic counterpart for each boson of the Standard Model. These counterparts, usually referred to as superpartners, constitute additional particles with respect to the Standard Model. This assumptions defines the so-called *Minimal Supersymmetric Standard Model* (MSSM), which will be at the centre of the studies presented in this manuscript. A detailed discussion of the Supersymmetry algebra can be found, among others, in Refs. [66, 67].

The particle content of the MSSM in terms of supermultiplets is summarized in Table 1.3. The scalar partners of the Standard Model quarks are referred to as "scalar quarks" or *squarks*, the scalar partners of the leptons are the "scalar leptons" or *sleptons*, and the scalar partners associated to the neutrinos are the "scalar neutrinos" or *sneutrinos*. The fermionic partners of the gauge bosons are called *bino*, *winos*, *gluino*, which refers to the B^0- and $W^{0,\pm}$-bosons before electroweak symmetry breaking as well as to the gluon. It is to be noted that in supersymmetric theories, in contrast to the Standard Model, and in order to forbid anomalies, electroweak symmetry breaking is implemented by means of two complex Higgs doublets H_u and H_d coupling respectively to up- and down-type (s)fermions. The fermionic partners of the scalar Higgs doublets are called *Higgsinos*. By convention, the superpartnes are denoted by adding a tilda to the Standard Model notation, e.g., $\tilde{e}$ for a "selectron" being the superpartner of the electon e. The supermultiplets of the MSSM are summarized in Table 1.3.

Since no superpartners have been observed at the same masses as the Standard Model particles, Supersymmetry must be broken at the TeV scale, i.e. additional mass terms must be

		spin 0	spin 1/2
(s)quarks	Q	$(\tilde{u}_L, \tilde{d}_L)$	(u_L, d_L)
	u	$\tilde{u}_R^*$	$u_R^\dagger$
	d	$\tilde{d}_R^*$	$d_R^\dagger$
(s)leptons	L	$(\tilde{e}_L, \tilde{\nu}_L)$	(e_L, ν_L)
	e	$\tilde{e}_R^*$	$e_R^\dagger$
Higgs(inos)	H_u	(H_u^+, H_u^0)	$(\tilde{H}_u^+, \tilde{H}_u^0)$
	H_d	(H_d^0, H_d^-)	$(\tilde{H}_d^0, \tilde{H}_d^-)$

	spin 1/2	spin 1
Gluino, gluon	$\tilde{g}$	g
W(inos)	$\tilde{W}^\pm, \tilde{W}^0$	$W^\pm, W^0$
B(inos)	$\tilde{B}^0$	B^0

TABLE 1.3: Chiral (left) and vector (right) supermultiplets of the Minimal Supersymmetric Standard Model. The remaining quantum numbers are the same as those of their Standard Model parts displayed in Table 1.1.

present in the Lagrangian of the theory, lifting the superpartners to higher mass scales. Although the precise origin of the breaking mechanism are unknown, it can be parametrized in terms of so-called *soft-breaking* terms, which are included in the Lagrangian of the MSSM,

$$\begin{aligned} -\mathcal{L}_{\text{soft}}^{\text{MSSM}} &= \frac{1}{2}\Big(M_1 \tilde{B}^0 \tilde{B}^0 + M_2 \tilde{W}^+ \tilde{W}^- + M_3 \tilde{g}\tilde{g} + \text{h.c.}\Big) \\ &\quad + \tilde{Q}^\dagger M_{\widetilde{Q}}^2 \tilde{Q} + \tilde{u}^* M_{\widetilde{U}}^2 \tilde{u} + \tilde{d}^* M_{\widetilde{D}}^2 \tilde{d}^\dagger + \tilde{L}^\dagger M_{\widetilde{L}}^2 \tilde{L} + \tilde{e}^* M_{\widetilde{E}}^2 \tilde{e} \\ &\quad + \Big(\tilde{u}^* A_u \tilde{Q} H_u + \tilde{d}^* A_d \tilde{Q} H_d + \tilde{e}^* A_e \tilde{L} H_d + \text{h.c.}\Big) \\ &\quad + m_{H_u}^2 H_u^* H_u + m_{H_d}^2 H_d^* H_d + \Big(b H_u^* H_d + \text{h.c.}\Big)\,. \end{aligned} \tag{1.29}$$

For the sector of squarks and sleptons, the soft-breaking Lagrangian introduces the mass matrices $M_{\widetilde{Q}}^2$ for the "left-handed" squarks, $M_{\widetilde{U}}^2$ for the "right-handed" up-type squarks, $M_{\widetilde{D}}^2$ for the "right-handed" down-type squarks, $M_{\widetilde{L}}^2$ for the "left-handed" sleptons and sneutrinos, and $M_{\widetilde{E}}^2$ for the "right-handed" sleptons. Note that the naming convention is somewhat abusive, the terms "left-handed" and "right-handed" not refering to the squarks or sleptons themselves but rather to their fermionic Standard Model partners. Finally, we have three trilinear coupling matrices A_u, A_d, A_e for the up-type squarks, down-type squarks, and sleptons, respectively.

To complete the discussion, the first line of Eq. (1.29) includes mass terms for the bino, wino, and gluino, while the last line concerns the mass of the physical Higgs bosons. In total, the soft-breaking Lagrangian contains over 120 free parameters. In constrained or simplified models, such as the "constrained MSSM" (CMSSM) [68] or the "phenomenological MSSM" (pMSSM) [69], the number of free parameters can be reduced, reaching from a few to about twenty.

In the remainder of this Section, I shall briefly review the different sectors of the MSSM particle content, giving a larger focus on the sector of squarks. In particular, I will discuss the implementation of the concepts of Minimal and Non-Minimal Flavour Violation in this sector.

Higgs sector

As mentioned above, in a supersymmetric theory two Higgs doublets are needed to convey electroweak symmetry breaking. More precisely, the two complex doublets H_u and H_d couple to up-type and down-type fields, respectively. In terms of the supermultiplets of Table 1.3, the

corresponding superpotential can be written as

$$\mathcal{W}_{\text{MSSM}} = \bar{u} Y_u Q H_u + \bar{d} Y_d Q H_d + \bar{e} Y_e L H_d + \mu H_u H_d + \text{h.c.}\,. \tag{1.30}$$

Upon electroweak symmetry breaking, both Higgs doublets acquire vacuum expectation values, $\langle H_u \rangle = v_u/\sqrt{2}$ and $\langle H_d \rangle = v_d/\sqrt{2}$, and are expanded according to

$$H_u = \begin{pmatrix} H_u^+ \\ \frac{1}{\sqrt{2}}\left(v_u + h_u^0 + i A_u^0\right) \end{pmatrix}, \qquad H_d = \begin{pmatrix} \frac{1}{\sqrt{2}}\left(v_d + h_d^0 + i A_d^0\right) \\ H_d^- \end{pmatrix}. \tag{1.31}$$

The CP-even, CP-odd, and charged components mix and give rise to two CP-even mass eigenstates, h^0 and H^0, one CP-odd pseudoscalar eigenstate, A^0, and two charged mass eigenstates $H^\pm$. By convention h^0 is identified with the "Standard-Model-like" Higgs-boson such that $m_{h^0} \approx 125$ GeV. The mixing is parametrized by the two mixing angles α and β. The latter is related to the vacuum expectation values through

$$\tan\beta = \frac{v \sin\beta}{v \cos\beta} = \frac{v_u}{v_d}, \qquad v_u^2 + v_d^2 = v^2 \approx (246\,\text{GeV})^2\,. \tag{1.32}$$

Considering the MSSM at the TeV scale, as it will be done, e.g., in Sec. 2.2, the key parameters are typically chosen to be the ratio of the two vacuum expectation values $\tan\beta$, the Higgsino mass parameter μ, and the pole mass of the pseudoscalar Higgs boson m_{A^0}. In contrast, if the MSSM parameters are defined at higher scales, such as the Grand Unification scale, it is more convenient to choose the mass parameters associated to the two doublets, $m_{H_u}^2$ and $m_{H_d}^2$ together with the ratio of the vacuum expectation values $\tan\beta$ as key parameters. Such a setup will be discussed in Sec. 4.2. For a more detailed presentation and review of the MSSM Higgs sector, the reader is referred, e.g., to Refs. [67, 70].

Gaugino sector

Coming to the fermionic partners of the gauge and Higgs bosons, after electroweak symmetry breaking the neutral fermions share the same quantum numbers and the corresponding physical states will be superpositions of the gauge eigenstates. More precisely, the neutral bino, wino, and Higgsinos mix to give rise to four *neutralinos*, denoted $\tilde{\chi}_i^0$ ($i = 1, \ldots, 4$). The lightest of the four neutralinos typically acts as the dark matter candidate.

In the same way, the charged winos and Higgsinos mix to the physical *charginos*, denoted $\tilde{\chi}_i^\pm$ ($i = 1, 2$). Being the only strongly interaction fermion of the theory, the gluino does not mix with other states. A more complete review of the gaugino sector, including the corresponding Lagrangian, mass matrix, and mixing matrices, can be found, e.g., in Refs. [66, 67].

Squark sector

It is convenient to rotate the squark fields $\tilde{u}_L$, $\tilde{u}_R$, $\tilde{d}_L$, and $\tilde{d}_R$ in the same way as presented in Chap. 1.1 for their Standard Model counterparts. This defines the so-called *super-CKM basis* [71], maintaining the Yukawa matrices diagonal. In this basis, the squared mass matrices for

up- and down-type squarks are given by

$$\begin{aligned}\mathcal{M}^2_{\tilde{u}} &= \begin{pmatrix} V_{\mathrm{CKM}} M^2_{\tilde{Q}} V^\dagger_{\mathrm{CKM}} + M^2_u + D_{uL} & \frac{v_u}{\sqrt{2}} T^\dagger_u - M_u \mu / \tan\beta \\ \frac{v_u}{\sqrt{2}} T_u - M_u \mu^* / \tan\beta & M^2_{\tilde{U}} + M^2_u + D_{uR} \end{pmatrix}, \\ \mathcal{M}^2_{\tilde{d}} &= \begin{pmatrix} M^2_{\tilde{Q}} + M^2_d + D_{dL} & \frac{v_d}{\sqrt{2}} T^\dagger_d - M_d \mu \tan\beta \\ \frac{v_d}{\sqrt{2}} T_d - M_d \mu^* \tan\beta & M^2_{\tilde{D}} + M^2_d + D_{dR} \end{pmatrix}, \end{aligned} \tag{1.33}$$

respectively. Again, flavour indices are omitted for the sake of readability. It is to be noted that the left-left sectors share the common mass parameter $M^2_{\tilde{Q}}$, as they are related through $SU(2)$ symmetry, and the misalignment discussed in Sec. 1.1 manifests as the relative rotation by the CKM-matrix. The matrices M_u and M_d are the diagonal up- and down-type quark mass matrices, respectively, giving a Supersymmetry-conserving contribution. Finally, the diagonal "D-terms" are given by

$$D_{qL} = m^2_Z \left(T_3 - Q \sin^2\theta_W\right) \cos 2\beta\,, \tag{1.34}$$

$$D_{qR} = m^2_Z Q \sin^2\theta_W \sin 2\beta\,, \tag{1.35}$$

for $q = u, d$, where T_3 and Q denote weak isospin and electric charge of the corresponding quark. In the following, we will focus on the structure of the soft-mass matrices $M^2_{\tilde{Q}}$, $M^2_{\tilde{U}}$, and $M^2_{\tilde{D}}$, as well as the trilinear coupling matrices T_u and T_d.

The diagonalization of the above matrices leads to the physical mass eigenstates of the squarks. I will discuss the diagonalization seperately depending on the chosen flavour scenario.

Minimal Flavour Violation

In the case of Minimal Flavour Violation, additional flavour violation with respect to the CKM matrix is forbidden, such that the soft matrices $M_{\tilde{Q}}$, $M_{\tilde{U}}$, and $M_{\tilde{D}}$, as well as the trilinear matrices T_u and T_d are diagonal in flavour space. In this case, the mass matrices of Eq. (1.33) break down to in total six matrices of dimension two. The trilinear terms then give rise to mixing between the "left-" and "right-handed" squark gauge eigenstates.

Since the corresponding entry in the mass matrix is proportional to the quark mass matrix, for typical phenomenological purposes only helicity mixing within the third generation is considered. As an example, the two-dimensional stop mass matrix is then diagonalized by a rotation matrix than can be parametrized by a single mixing angle $\theta_{\tilde{t}}$. The gauge eigenstates $\left(\tilde{t}_L, \tilde{t}_R\right)$ are linked to the physical mass eigenstates $\left(\tilde{t}_1, \tilde{t}_2\right)$ through

$$\begin{pmatrix} \tilde{t}_1 \\ \tilde{t}_2 \end{pmatrix} = \begin{pmatrix} \cos\theta_{\tilde{t}} & -\sin\theta_{\tilde{t}} \\ \sin\theta_{\tilde{t}} & \cos\theta_{\tilde{t}} \end{pmatrix} \begin{pmatrix} \tilde{t}_L \\ \tilde{t}_R \end{pmatrix}, \tag{1.36}$$

where by convention $m_{\tilde{t}_1} < m_{\tilde{t}_2}$. The mass splitting is mainly driven by the magnitude of the corresponding trilinear coupling parameter, e.g., $\left(T_u\right)_{33}$ in the present case of the stops. Similar expressions hold for the sbottoms and staus, while for the first and second generation squarks, in the absence of sizeable trilinear terms, the mass eigenstates essentially correspond to the flavour eigenstates. Let us note again, that in this case, all quark flavour-changing interactions relate to the CKM matrix as discussed in Sec. 1.1.

Non-Minimal Flavour Violation

Allowing for Non-Minimal Flavour Violation, the additional sources of flavour mixing manifest as non-diagonal terms in the soft and trilinear matrices. For example, a non-zero element $\left(\mathcal{M}^2_{\tilde{Q}}\right)_{23}$ induces inter-generational mixing of $\tilde{c}_L$ and $\tilde{t}_L$, a non-zero element $\left(T_u\right)_{32}$ describes a mixing of $\tilde{c}_R$ and $\tilde{t}_L$, and so on.

In this framework, the physical mass eigenstates are not necessarily single-flavoured but can rather be a superposition of up to all six flavours. Therefore, they are labeled $\tilde{u}_1, \tilde{u}_2, \ldots, \tilde{u}_6$ for the up-type squarks, and $\tilde{d}_1, \tilde{d}_2, \ldots, \tilde{d}_6$ for the down-type squarks. By convention they are mass-ordered according to $m_{\tilde{u}_1} < m_{\tilde{u}_2} < \ldots < m_{\tilde{u}_6}$ and similarly for the down-type squarks.

The diagonalization of the mass matrices in Eq. (1.33),

$$\begin{aligned} \mathrm{diag}\left(m^2_{\tilde{u}_1}, \ldots, m^2_{\tilde{u}_6},\right) &= \mathcal{R}_{\tilde{u}} \mathcal{M}^2_{\tilde{u}} \mathcal{R}^\dagger_{\tilde{u}}, \\ \mathrm{diag}\left(m^2_{\tilde{d}_1}, \ldots, m^2_{\tilde{d}_6},\right) &= \mathcal{R}_{\tilde{d}} \mathcal{M}^2_{\tilde{d}} \mathcal{R}^\dagger_{\tilde{d}}, \end{aligned} \tag{1.37}$$

introduces two rotation matrices, which link the gauge and mass eigenstates of the up- and down-type squarks, respectively, according to

$$\begin{aligned} \left(\tilde{u}_1, \tilde{u}_2, \ldots, \tilde{u}_6\right)^T &= \mathcal{R}_{\tilde{u}} \left(\tilde{u}_L, \tilde{c}_L, \tilde{t}_L, \tilde{u}_R, \tilde{c}_R, \tilde{t}_R\right)^T, \\ \left(\tilde{d}_1, \tilde{d}_2, \ldots, \tilde{d}_6\right)^T &= \mathcal{R}_{\tilde{d}} \left(\tilde{d}_L, \tilde{s}_L, \tilde{b}_L, \tilde{d}_R, \tilde{s}_R, \tilde{b}_R\right)^T. \end{aligned} \tag{1.38}$$

Compating to the situation of minimal flavour violation, the rotation matrices thus can be seen as "generalized squark mixing angles". They carry the essential information about the flavour content of each physical state, and therefore appear naturally in the couplings of squarks to other fields. Detailed listings of the couplings can be found in Refs. [72, 73, 74].

In order to study the parameter space including non-minimally flavour-violating terms, it is convenient to work within a scenario-independant parametrization allowing to compare different parameter points more easily. Such a parametrization can be achieved by normalizing the flavour-violating non-diagonal elements of the mass matrix with respect to the corresponding diagonal ones. This defines the following set of dimensionless quark-flavour violation parameters,

$$\begin{aligned} \left(\delta_{LL}\right)_{ij} &= \frac{\left(M^2_{\tilde{Q}}\right)_{ij}}{\left(M_{\tilde{Q}}\right)_{ii}\left(M_{\tilde{Q}}\right)_{jj}}, & & \\ \left(\delta^u_{RR}\right)_{ij} &= \frac{\left(M^2_{\tilde{U}}\right)_{ij}}{\left(M_{\tilde{U}}\right)_{ii}\left(M_{\tilde{U}}\right)_{jj}}, & \left(\delta^d_{RR}\right)_{ij} &= \frac{\left(M^2_{\tilde{D}}\right)_{ij}}{\left(M_{\tilde{D}}\right)_{ii}\left(M_{\tilde{D}}\right)_{jj}}, \\ \left(\delta^u_{RL}\right)_{ij} &= \frac{v_u}{\sqrt{2}} \frac{\left(T_u\right)_{ij}}{\left(M_{\tilde{Q}}\right)_{ii}\left(M_{\tilde{U}}\right)_{jj}}, & \left(\delta^d_{RL}\right)_{ij} &= \frac{v_d}{\sqrt{2}} \frac{\left(T_d\right)_{ij}}{\left(M_{\tilde{Q}}\right)_{ii}\left(M_{\tilde{D}}\right)_{jj}}, \\ \left(\delta^u_{LR}\right)_{ij} &= \frac{v_u}{\sqrt{2}} \frac{\left(T_u\right)_{ji}}{\left(M_{\tilde{U}}\right)_{ii}\left(M_{\tilde{Q}}\right)_{jj}}, & \left(\delta^d_{LR}\right)_{ij} &= \frac{v_d}{\sqrt{2}} \frac{\left(T_d\right)_{ji}}{\left(M_{\tilde{D}}\right)_{ii}\left(M_{\tilde{Q}}\right)_{jj}}, \end{aligned} \tag{1.39}$$

where we use the implicit notation $\left(M_{\tilde{Q}}\right)_{ij} = \sqrt{\left(M^2_{\tilde{Q}}\right)_{ij}}$.

Slepton and sneutrino sector

In the same way as for the squarks, the slepton and sneutrino fields undergo the same rotation as the leptons and neutrinos in the Standard Model, potentially augmented by some mechanism generating neutrino masses as discussed in Sec. 1.2. In the so-called *super-PMNS* basis, where the corresponding Yukawa couplings are diagonal, the squared mass matrix is given by

$$\mathcal{M}^2_{\tilde{\ell}} = \begin{pmatrix} M^2_{\tilde{L}} + M^2_e + D_{eL} & \frac{v_d}{\sqrt{2}} T^\dagger_e - M_e \mu \tan\beta \\ \frac{v_d}{\sqrt{2}} T_e - M_e \mu^* \tan\beta & M^2_{\tilde{E}} + M^2_e + D_{eR} \end{pmatrix} . \tag{1.40}$$

Again, the lepton mass matrix is diagonal by choice of basis, and the "D-terms" have similar expressions as given in Eq. (1.35) for the quarks. The squared mass matrix for the sneutrinos is

$$\mathcal{M}^2_{\tilde{\nu}} = V_{\text{PMNS}} M^2_{\tilde{L}} V^\dagger_{\text{PMNS}} + M^2_\nu + D_{\nu L} , \tag{1.41}$$

where only the "left-handed" block is present due to the absence of right-handed neutrinos.

As for the squarks discussed above, the structure of the involved soft-mass and trilinear terms depends on the assumption of the flavour structure. While assuming MFV, the matrices $M^2_{\tilde{L}}$, $M^2_{\tilde{E}}$, and T_ℓ are diagonal, they may include off-diagonal elements when assuming NMFV. In this case, dimensionless NMFV-parameters can be defined analogously to those given in Eq. (1.39). In the general case, the diagonalization of the two mass matrices proceeds through

$$\begin{aligned} \left(\tilde{\ell}_1, \tilde{\ell}_2, \ldots, \tilde{\ell}_6\right)^T &= \mathcal{R}_{\tilde{\ell}} \left(\tilde{e}_L, \tilde{\mu}_L, \tilde{\tau}_L, \tilde{e}_R, \tilde{\mu}_R, \tilde{\tau}_R\right)^T , \\ \left(\tilde{\nu}_1, \tilde{\nu}_2, \tilde{\nu}_3\right)^T &= \mathcal{R}_{\tilde{\nu}} \left(\tilde{\nu}_{Le}, \tilde{\nu}_{L\mu}, \tilde{\nu}_{L\tau}\right)^T . \end{aligned} \tag{1.42}$$

As the discussion within present manuscript will mainly focus on the sector of squarks, and in particular Non-Minimal Flavour Violation therein, the discussion of the slepton sector is kept rather short here. The interested reader is referred to, e.g., Refs. [66, 67] for a more detailed discussion.

Benefits of the MSSM

To conclude this Chapter, I will mention how Supersymmetry, and in particular the Minimal Supersymmetric Standard Model (MSSM), allows to cure certain shortcomings of the Standard Model mentioned in Sec. 1.2. As already mentioned above, the lightest neutralino is a very good candidate for cold dark matter reaching the observed relic abundance through the freeze-out mechanism. Detailed reviews of neutralino dark matter can be found, among others, in Refs. [75, 76].

Concerning the quadratic divergences in the Higgs mass calculation, it turns out that including the corrections due to the additional particles, namely the sfermions, cancels the divergence provided that Supersymmetry is preserved, i.e. that the sfermions have the same mass as the fermions, and that the corresponding couplings to the Higgs boson match. A detailed discussion and calculation can be found, e.g., in Refs. [66, 67].

In addition, it has been shown that the gauge couplings unify to a better precision in the MSSM as they do in the Standard Model alone [77]. Finally, Supersymmetry does not provide an intrinsic mechanism to generate neutrino masses. However, "standard" mechanisms such as the Seesaw mechanism can be implemented in the MSSM without difficulty, see Refs. [78, 79, 80, 81, 82, 83, 84, 85, 86, 87] for examples.

Chapter 2

Flavour constraints on new physics models

Additional states with respect to the Standard Model impact the theory predictions of basically all observables in particle physics. Consequently, a very large variety of experimental measurements can be used to constrain new physics models.

In addition to searches for new physics at colliders and the search for astrophysical dark matter signals, theories beyond the Standard Model are in particular heavily constrained by a large number of precision measurements, mostly related to rare decays of mesons and leptons. In such cases, the new particles appear through their virtual effects, e.g., at the one-loop level.

The present Chapter is dedicated to a discussion of such observables. In Sec. 2.1, a summary of relevant observables and constraints is presented. In Sec. 2.2, an extensive study of Non-Minimal Flavour Violation within the sector of squarks of the Minimal Supersymmetric Standard Model, in particuler in view of the mentioned flavour constraints, is discussed. This discussion is based on Ref. [88].

2.1 The experimental situation

The aim of the present Section is to give an overview of the most important constraints on new physics models stemming from observables related to flavour physics. This includes measurements within the hadronic sector, such as meson decays and oscillation parameters, as well as within the leptonic sector, such as rare lepton decays or the anomalous magnetic moments of leptons. The constraints relevant for the analyses presented in this manuscript are summarized in Table 2.1, indicating the respective uncertainties, confidence level, and bibliographic references.

It is to be noted that, while in the Standard Model the mass of the Higgs boson is a free parameter, its value is a prediction in extensions such as the Minimal Supersymmetric Standard Model discussed in Sec. 1.3. I therefore include the observed value of the Higgs boson mass into the summary of constraints. Another constraint, that is powerful but not related to flavour-changing currents, is the relic density $\Omega_{\text{CDM}}h^2$ of dark matter, interpreted in the ΛCDM model, given in the last line of Table 2.1.

In addition to the indirect constraints given in Table 2.1, direct searches at collider, in particular the *Large Hadron Collider* via the ATLAS and CMS experiments, have lead to null results in view of particles not belonging to the Standard Model. Such null results are interpreted in terms of exclusion limits on the respective particle masses and, in certain circumstances, their couplings to the Standard Model fields [35]. Aspects of flavour violation in such searches will be discussed in Chap. 3 of this manuscript.

In addition, a large number of experimental collaborations aim at the detection of dark matter. The constraints stemming from direct or indirect detection of dark matter are numerous, but not relevant for the work presented in this manuscript. I will therefore not discus this

Observable	Experimental result	References	Remarks	
m_{h^0}	(125.2 ± 2.1) GeV	[35, 89]	(1)	(2)
$\mathrm{BR}(B \to X_s\gamma)$	$(3.32 \pm 0.15) \cdot 10^{-4}$	[90]	(1)	(2)
$\mathrm{BR}(B \to X_s\mu\mu)_{q^2\in[1;6]\ \mathrm{GeV}^2}$	$(0.66 \pm 0.55) \cdot 10^{-6}$	[91]	(1)	(2)
$\mathrm{BR}(B \to X_s\mu\mu)_{q^2>14.4\ \mathrm{GeV}^2}$	$(0.60 \pm 0.26) \cdot 10^{-6}$	[91]	(1)	
$\mathrm{BR}(B_s \to \mu\mu)$	$(2.7 \pm 1.0) \cdot 10^{-9}$	[35]	(1)	
$\mathrm{BR}(B \to K^*\mu\mu)_{q^2\in[1;6]\ \mathrm{GeV}^2}$	$(1.7 \pm 0.26) \cdot 10^{-7}$	[92]	(1)	
$\mathrm{AFB}(B \to K^*\mu\mu)_{q^2\in[1.1;6]\ \mathrm{GeV}^2}$	$(-0.075 \pm 0.030) \cdot 10^{-7}$	[93]	(1)	
$\mathrm{BR}(B_u \to \tau\nu)\,/\mathrm{BR}(B_u \to \tau\nu)_{\mathrm{SM}}$	1.04 ± 0.34	[35]	(1)	
$\mathrm{BR}(K^0 \to \pi^0\nu\nu)$	$\leq 2.6 \cdot 10^{-8}$	[35]	(1)	
$\mathrm{BR}(K^+ \to \pi^+\nu\nu)$	$1.73^{+0.97}_{-0.88} \cdot 10^{-10}$	[35]	(1)	
ΔM_{B_s}	$(17.757 \pm 2.266)\ \mathrm{ps}^{-1}$	[35, 94]	(1)	(2)
ΔM_K	$(3.1 \pm 1.0) \cdot 10^{-15}$ GeV	[35, 95]		(2)
ϵ_K	2.228 ± 0.243	[35, 95]	(1)	(2)
$\mathrm{BR}(\mu \to e\gamma)$	$< 4.2 \cdot 10^{-13}$	[35]		(2)
$\mathrm{BR}(\mu \to e\gamma\gamma)$	$< 7.2 \cdot 10^{-11}$	[35]		(2)
$\mathrm{BR}(\mu \to 3e)$	$< 1.0 \cdot 10^{-12}$	[35]		(2)
$\mathrm{BR}(\tau \to e\gamma)$	$< 3.3 \cdot 10^{-8}$	[35]		(2)
$\mathrm{BR}(\tau \to 3e)$	$< 2.7 \cdot 10^{-8}$	[35]		(2)
$\mathrm{BR}(\tau \to \mu\gamma)$	$< 4.4 \cdot 10^{-8}$	[35]		(2)
$\mathrm{BR}(\tau \to 3\mu)$	$< 2.1 \cdot 10^{-8}$	[35]		(2)
$\mathrm{BR}(\tau \to e^-\mu\mu)$	$< 2.7 \cdot 10^{-8}$	[35]		(2)
$\mathrm{BR}(\tau \to e^+\mu\mu)$	$< 1.7 \cdot 10^{-8}$	[35]		(2)
$\mathrm{BR}(\tau \to \mu^-ee)$	$< 1.8 \cdot 10^{-8}$	[35]		(2)
$\mathrm{BR}(\tau \to \mu^+ee)$	$< 1.5 \cdot 10^{-8}$	[35]		(2)
$\Delta a_\mu = a_\mu^{\mathrm{exp}} - a_\mu^{\mathrm{SM}}$	$(26.1 \pm 10.74) \cdot 10^{-10}$	[35]	(1)	(2)†
$\Omega_{\mathrm{CDM}}h^2$	(0.1200 ± 0.0020)	[48]		(2)

TABLE 2.1: Experimental constraints at the 90% confidence level on the new physics parameter space imposed from Higgs boson mass, quark-flavour changing processes, lepton-flavour violating processes, the anomalous magnetic moments of leptons, and dark matter requirements. The numbers (1) and (2) in the last column indicate that the respective constraint has been taken into account in the Markov-Chain Monte-Carlo study of the pMSSM presented in Sec. 2.2 or in the study of the $SU(5) \times A_4$ supersymmetric Grand Unification model discussed in Sec. 4.2. For the anomalous magnetic moment of the muon, the † indicates that this constraint has been taken into account in the original motivation of the study, but has not explictely been evaluated in the analysis of Non-Minimal Flavour Violation.

topic in detail here. Concerning the neutralino relic density in the MSSM, it can be noted that the impact of Non-Minimal Flavour Violation is rather small, unless the scenario under consideration features important contributions from neutralino-sfermion co-annihilations or the flavour-violating terms in the sfermion mass matrix are very large [96, 97]. For this reason, dark matter constraints is not included in the study presented in the following Section.

2.2 An MCMC study of squark generation mixing

In recent years, the phenomenological consequences of non-minimal flavour violation in the squark sector have been studied in various areas. More precisely, effects on low-energy observables such as rare decays [98] or oblique parameters [99] have been considered, and the potential signatures at the Large Hadron Collider have been largely investigated [72, 73, 100, 101, 74, 102, 103, 104, 105, 106, 107, 108, 109, 110, 111]. More recently, the existing constraints on possible non-vanishing flavour-mixing parameters have been updated [112, 113]. All these results have been derived under the assumption that only few off-diagonal elements of the squark mass matrices are non-zero, and that at most two among them are varied at the same time. One would, however, generally expect that several or all of the flavour-violating entries are non-vanishing, especially if the flavour structure is generated by some mechanism at a higher scale. Consequently, a comprehensive study of the most general NMFV configuration of the MSSM, where all flavour-violating terms of the Lagrangian are taken in account and confronted to current data and theoretical constraints, is in order.

The results summarized in this Section present a first step in this direction. They stem from a detailed study of squark-generation mixing initiated during the 2013 *PhysTeV Les Houches* workshop [114] and published in Ref. [88]. While the present Section gives an overview over the main results, all details can be found directly in Ref. [88].

In order to keep a reasonable number of supersymmetric parameters for our study, we assume that the first two generations of squarks are degenerate. The flavour-conserving soft masses are then determined by six free parameters,

$$\begin{aligned} M_{\tilde{Q}_{1,2}} &\equiv (M_{\tilde{Q}})_{11} = (M_{\tilde{Q}})_{22}\,, & M_{\tilde{Q}_3} &\equiv (M_{\tilde{Q}})_{33}\,, \\ M_{\tilde{U}_{1,2}} &\equiv (M_{\tilde{U}})_{11} = (M_{\tilde{U}})_{22}\,, & M_{\tilde{U}_3} &\equiv (M_{\tilde{U}})_{33}\,, \\ M_{\tilde{D}_{1,2}} &\equiv (M_{\tilde{D}})_{11} = (M_{\tilde{D}})_{22}\,, & M_{\tilde{D}_3} &\equiv (M_{\tilde{D}})_{33}\,, \end{aligned} \tag{2.1}$$

For simplicity, we take the trilinear coupling parameters of the third generation to be equal,

$$A_f \equiv (A_u)_{33} = (A_d)_{33} = (A_e)_{33}\,, \tag{2.2}$$

while those of the first and second generation are set to zero since we neglect the corresponding Yukawa couplings. Coming to the flavour off-diagonal elements of the soft mass and trilinear coupling matrices, we ignore any mixing involving the first generation squarks in order to be compliant with kaon data [115]. We therefore consider mixing between the second and third generation squarks, which is parametrized (see Eqs. (1.39)) by

$$\delta_{LL},\quad \delta^u_{RR},\quad \delta^d_{RR},\quad \delta^u_{LR},\quad \delta^u_{RL},\quad \delta^d_{LR},\quad \text{and}\quad \delta^d_{RL}\,. \tag{2.3}$$

The gaugino sector is chosen to be determined by the bino mass M_1 alone. The wino and gluino tree-level masses M_2 and M_3 are then obtained by making use of the relation $M_1 = \frac{1}{2}M_2 = \frac{1}{6}M_3$, which is inspired by Grand Unified theories. Finally, we parametrize the Higgs sector in the usual way, i.e. the free parameters are μ, m_{A^0}, and $\tan\beta$.

Parameter	Scanned range
$\alpha_s(m_Z)$	$\mathcal{N}(0.1184, 0.0007)$
m_t^{pole}	$\mathcal{N}(173.3, 1.3928)$
$m_b(m_b)$	$\mathcal{N}(4.19, 0.12)$
$M_{\tilde{Q}_{1,2}}$	[300, 3500]
$M_{\tilde{Q}_3}$	[100, 3500]
$M_{\tilde{U}_{1,2}}$	[300, 3500]
$M_{\tilde{U}_3}$	[100, 3500]
$M_{\tilde{D}_{1,2}}$	[300, 3500]
$M_{\tilde{D}_3}$	[100, 3500]
A_f	[-10000, 10000] or $\lvert A_f\rvert < 4\max\{M_{\tilde{q}}, M_{\tilde{\ell}}\}$

Parameter	Scanned range
$\tan\beta$	[10, 50]
μ	[100, 850]
m_A	[100, 1600]
M_1	[100, 1600]
$M_{\tilde{\ell}}$	[100, 3500]
δ_{LL}	[-0.8, 0.8]
δ^u_{RR}	[-0.8, 0.8]
δ^d_{RR}	[-0.8, 0.8]
δ^u_{LR}	[-0.5, 0.5]
δ^u_{RL}	[-0.5, 0.5]
δ^d_{LR}	[-0.05, 0.05]
δ^d_{RL}	[-0.05, 0.05]

TABLE 2.2: Supersymmetric and Higgs sectors of our NMFV MSSM parameter space, as well as varying Standard Model parameters. All dimensionful quantities are given in GeV. $\mathcal{N}(\mu, \sigma)$ denotes a Gaussian profile of mean μ and width σ. The variable $M_{\tilde{q}}$ corresponds to the maximum of the diagonal entries of the matrices $M_{\tilde{Q}}$, $M_{\tilde{U}}$, and $M_{\tilde{D}}$.

For an efficient exploration of this 22-dimensional parameter space, we rely on a Markov Chain Monte Carlo (MCMC) scanning technique [116] based on the Metropolis-Hastings algorithm [117, 118]. A given point is accepted or rejected based on the comparison of the products of likelihoods of this point with that of the previous point. Each of the likelihoods is associated with a specific constraint accounting for measurements and theoretical predictions in the framework of the MSSM with Non-Minimal Flavour Violation. The experimental constraints taken into account in this analysis are marked as "(1)" in Table 2.1. The associated predictions are calculated using the `SuperIso` package [119, 120] when available, otherwise using `SPheno 3.3.3` [121, 122]. The data transfer between the two codes is achieved through the *Flavour Les Houches Accord* [123].

The above parameters are varied randomly within intervals which are chosen to yield a good coverage of the phenomenologically relevant parameter space. In addition, we have varied $\alpha_s(m_Z)$, m_t^{pole}, and $m_b(m_b)$ using a Gaussian profile taking into account their experimental uncertainties, while all other Standard Model parameters are fixed to the values given in Chap. 1.1. The applied ranges for all parameters are given in Table 2.2. Note that the limits on the trilinear coupling parameter A_f and the flavour-violating parameters are chosen to prevent all off-diagonal elements of the squark mass matrices from being too large, such that tachyonic mass eigenstates are avoided. For each parameter combination, the resulting mass spectrum is computed using the publicly available spectrum calculator `SPheno 3.3.3` [121, 122].

Concerning dark matter, only the requirement that the lightest supersymmetric particle is a neutralino has been imposed, while in particular the relic density has not been computed for the present study. For a study of neutralino annihilation in the presence of non-minimally flavour violating elements in the Lagrangian see Ref. [96].

The analysis of the results of the Markov Chain Monte Carlo analysis discussed above gives us information about the regions of parameter space that are favoured by the experimental data indicated in Table 2.1. The influence of a specific experimental result on a given parameter can be studied by comparing its theoretical prior distribution to the posterior distribution that is obtained after imposing the related constraint alone. The prior distributions of all parameters are obtained from a uniform random scan in which we discard parameter points that lead to

tachyons, where the electroweak symmetry is not successfully broken, or where the lightest neutralino is not the lightest supersymmetric particle. We hence include about $1.5 \cdot 10^6$ theoretically accepted setups. The posterior distributions are then computed on the basis of the MCMC scan, in which the experimental constraints indicated in Table 2.1 are imposed. The final posterior distributions include about 100000 points. To estimate the importance of each observable separately, we have run a separate MCMC scans for each observable. Note that the convergence test of Gelman and Rubin [124] has been verified.

In the following, the main results of the MCMC analysis are discussed.

Distributions of the flavour-conserving parameters

Although we are mainly interested in the flavour-violating parameters given in Eq. (1.39), we start the discussion by the obtained distributions for the flavour-conserving parameters of our model. The corresponding probability density distributions over the respective parameter ranges are shown in Fig. 2.1. Each panel shows the theoretical prior (yellow area) together with the posterior distribution (solid line), which includes the impact of the included constraints.

As can be seen, the prior distribution of the gaugino mass parameter M_1 is centred at relatively low values $M_1 \sim 400$ GeV and may reach values of up to about $M_1 \sim 1000$ GeV. When imposing all considered experimental constraints, the distribution is shifted by about 100 GeV to higher values. This behaviour can be traced to the chargino contributions to the branching ratio of the decay $B_s \to \mu^+\mu^-$ and to the B-meson mass difference ΔM_{B_s}. Let us recall that the chargino mass is governed by the parameter M_1.

For the trilinear coupling parameter A_f, the prior distribution is centred around zero. Large values are indeed often rejected since they may induce a large left-right mixing implying tachyonic states. Imposing the experimental constraints drastically changes the shape of the distribution, which now featues two peaks at $|A_f| \sim 3000$ GeV. This feature is induced by the condition on the Higgs boson mass, which requires a relatively large splitting of the squark masses exhibiting the largest stop components. The peaks correspond to the situation of $|X_t| \sim \sqrt{6} M_{\text{SUSY}}$, which is well-known for the MSSM with Minimal Flavour Violation [125].

The slepton mass parameter exhibits a peak around $M_{\tilde{\ell}} \sim 600$ GeV after imposing all experimental constraints. This is mainly inferred by the condition on the anomalous magnetic moment of the muon that strongly depends on the slepton sector properties. Remember that squarks enter the calculation only at the two-loop level, such that this constraint does not have a remarkable influence on the squark sector.

Turning to the Higgs sector (second line of Fig. 2.1), the prior distribution of the higgsino mass parameter μ shows a preference for low values, while its posterior distribution slightly peaks around $\mu \sim 200$ GeV due to the $B_s \to \mu^+\mu^-$, Δa_μ, and ΔM_{B_s} constraints, which all depend on the gaugino sector. Next, $\tan\beta$ tends towards lower values in both its prior and posterior distributions, the favourite values being pushed to the rough interval $12 \lesssim \tan\beta \lesssim 18$. Finally, the posterior distribution of the pseudoscalar mass m_A is shifted towards higher values with respect to its prior distribution. This results from the interplay of the most considered observables for which low values of m_A would induce too large contributions.

The last two lines of Fig. 2.1 concern the soft squark mass parameters. As can be seen, low values are preferred for the first and second generation squarks masses $M_{\tilde{Q}_{1,2}}$, $M_{\tilde{U}_{1,2}}$, and $M_{\tilde{D}_{1,2}}$. This feature is mostly caused by imposing the Higgs boson mass. It can be understood in the limiting case of $M_{\tilde{Q}_{1,2}} \simeq M_{\tilde{U}_{1,2}} \simeq M_{\tilde{D}_{1,2}} \equiv \tilde{M}^2$. The one-loop contributions to m_{h^0} that are proportional to δ^u_{LR} are then approximately given by [113]

$$\Delta m^2_{h^0} = \frac{3 v_u^4}{8\pi^2 (v_u^2 + v_d^2)} \left[\frac{(T_u)^2_{23}}{\tilde{M}^2} \left(\frac{(Y_u)^2_{33}}{2} - \frac{(T_u)^2_{23}}{12 \tilde{M}^2} \right) \right], \tag{2.4}$$

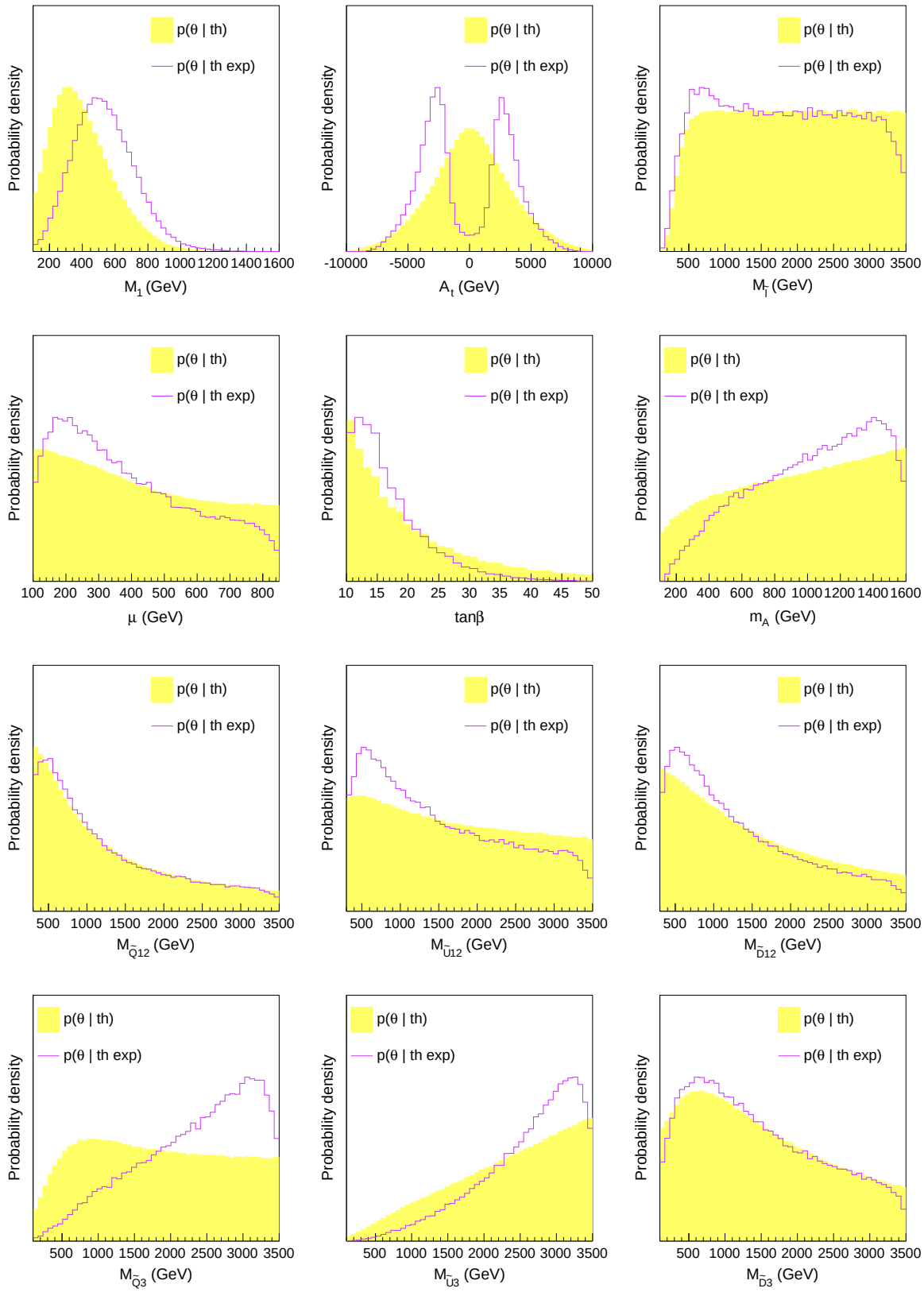

FIGURE 2.1: The one-dimensional prior (yellow filled area) and posterior (violet solid curve) distributions of the parameters of our NMFV MSSM description. The prior only incorporates theoretical inputs while the posterior distribution shows the impact of the experimental observations.

while the corresponding contributions of down-type squarks are obtained by replacing $T_u \to T_d$ and $Y_t \to Y_d$, and by exchanging $v_u \leftrightarrow v_d$. In our parametrization, we have

$$\left(T_u\right)_{23} = \frac{v_u}{\sqrt{2}} \delta^u_{LR} M_{\tilde{Q}_{1,2}} M_{\tilde{U}_3}\,, \tag{2.5}$$

such that for non-zero δ^u_{LR} the Higgs boson becomes tachyonic if the scale $\tilde{M}^2$ is too large. Similarly, the requirement of a physical solution for the electroweak vacuum also favours lower values for $M_{\tilde{Q}_{1,2}}$. The distributions of the third-generation mass parameters $M_{\tilde{Q}_3}$ and $M_{\tilde{U}_3}$ prefer in contrast larger values, which can be traced to the constraints from ΔM_{B_s} and the Higgs boson mass. Finally, both the prior and posterior distributions of the right-handed down-type squark mass $M_{\tilde{D}_3}$ prefer lower values and are in this case very similar.

Distributions of the flavour-violating parameters

We now turn to the analysis of the distributions of the seven non-minimally flavour-violating parameters, which are at the centre of interest of the present study. Their prior and posterior distributions are shown in Fig. 2.2.

The theoretical constraints on additional stop-scharm mixing in the left-left sector, corresponding to the parameter δ_{LL}, are relatively mild such that an almost flat prior distribution is observed. The parameter δ_{LL} is then mainly constrained by the B-meson oscillation parameter ΔM_{B_s}, which favours smaller absolute values of δ_{LL}, and the branching ratio of the decay $B_s \to \mu^+\mu^-$, which causes a slight preference for positive values. Values ranging up to $|\delta_{LL}| \lesssim 0.8$ can nevertheless be reached, but this requires simultanously large values for other NMFV-parameters such that cancellations between the different contributions to the considered observables occur.

In a similar way, the prior distributions of the parameters δ^u_{RR} and δ^d_{RR}, inducing mixing in the right-right sectors, show a mild preference for low absolute values. The posterior distribution of δ^u_{RR} does not differ significantly from its prior distribution meaning that δ^u_{RR} is insensitive to the experimental constraints under consideration. In contrast, the B-meson oscillation parameter ΔM_{B_s} restricts the posterior distribution of δ^d_{RR} to be narrower, while the branching ratio of $B_s \to \mu^+\mu^-$ implies a preference for negative values. However, the full explored range of $-0.8 \lesssim \delta^{u,d}_{RR} \lesssim 0.8$ remains accessible for both right-right mixing parameters.

The flavour-violating left-right and right-left elements of the up-type squark mass matrix, translating into the parameters δ^u_{RL} and δ^u_{LR}, turn out to be mainly constrained by the necessity to incorporate a Higgs boson mass of about 125 GeV. The posterior distribution of δ^u_{LR} exhibits two peaks at $|\delta^u_{LR}| \sim 0.5$ and is restricted to $-0.15 \lesssim \delta^u_{LR} \lesssim 0.15$. Theoretically, this behaviour is expected from Eq. (2.4). The parameter δ^u_{RL}, however, receives extra constraints stemming from the branching ratio of $B_s \to \mu^+\mu^-$, such that the posterior distribution peaks around zero and has a maximal value of $|\delta^u_{RL}| \sim 0.2$. We recall that the two parameters δ^u_{RL} and δ^u_{LR} are independent and induce different mixing patterns. More precisely, δ^u_{LR} describes a $\tilde{c}_L$–$\tilde{t}_R$ mixing, while δ^u_{RL} corresponds to mixing between the $\tilde{c}_R$ and $\tilde{t}_L$ eigenstates. The impact of the constraints and the resulting distributions are therefore different and directly related to the structure of the chargino-squark-quark and neutralino-squark-quark interactions.

In the down-type sector, the prior distributions of the parameters δ^d_{LR} and δ^d_{RL} show a clear peak for values close to zero. Large values are mostly discarded as they imply large off-diagonal terms in the mass matrix $\mathcal{M}^2_{\tilde{d}}$ and the resulting spectrum likely contains tachyons. Both parameters are hardly constrained by any of the observables under consideration and we only observe minor effects. The posterior distribution of δ^d_{LR} slightly prefers negative values, and the posterior distribution of δ^d_{RL} is slightly narrower, when both distributions are compared to their respective prior. This mostly results from an interplay of all observables, although for

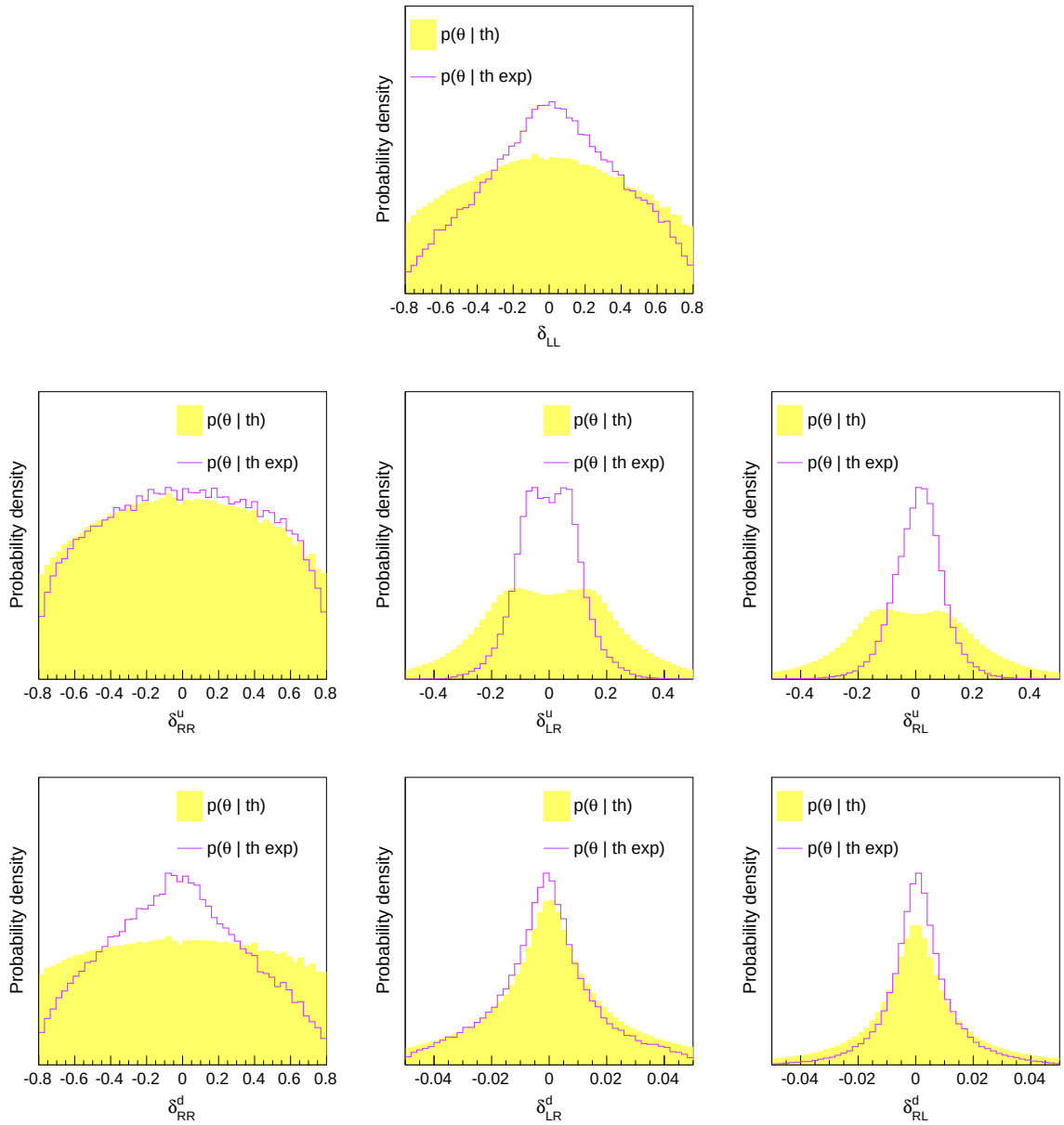

FIGURE 2.2: Same as Fig. 2.1 for the flavour-violating parameters of the NMFV MSSM setup under consideration.

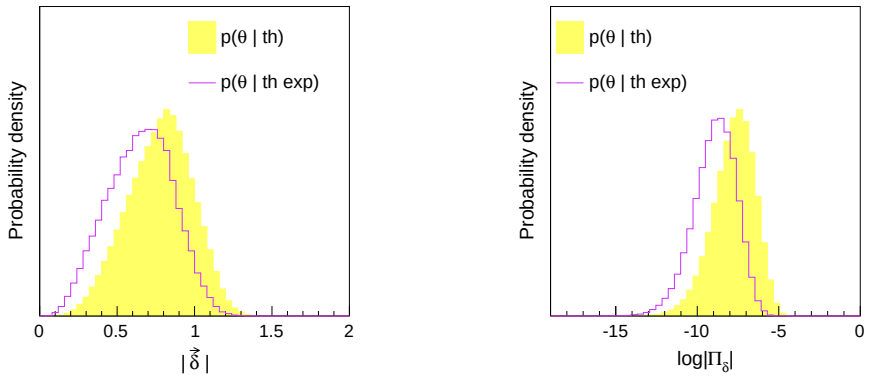

FIGURE 2.3: The one-dimensional prior (yellow histogram) and posterior (violet curve) distributions of the quantities $|\vec{\delta}|$ and $\log|\Pi_\delta|$ defined in Eqs. (2.6).

the δ^d_{RL} case, the B-meson oscillation observable ΔM_{B_s} and the Higgs boson mass requirement play a non-negligible role.

We finally illustrate the global distribution of all NMFV parameters under consideration. To this end, we introduce the quantities

$$\begin{aligned} |\vec{\delta}| &= \sqrt{(\delta_{LL})^2 + (\delta^u_{RR})^2 + (\delta^d_{RR})^2 + (\delta^u_{LR})^2 + (\delta^u_{RL})^2 + (\delta^d_{LR})^2 + (\delta^d_{RL})^2}\,, \\ \log|\Pi_\delta| &= \log\left|\delta_{LL}\,\delta^u_{RR}\,\delta^d_{RR}\,\delta^u_{LR}\,\delta^u_{RL}\,\delta^d_{LR}\,\delta^d_{RL}\right|. \end{aligned} \tag{2.6}$$

The former, $|\vec{\delta}|$, gives a measure of how far a given benchmark is situated from the minimally flavour-violating paradigm where $|\vec{\delta}| = 0$. The maximum value that can be reached in our setup is $|\vec{\delta}| \approx 1.56$. The second quantity, $\log|\Pi_\delta|$, gives an indication about how many NMFV parameters are sizeable at the same time. One of the NMFV parameters being close to zero pulls this quantity towards large negative values, while the case where all NMFV parameters are maximum corresponds to $\log|\Pi_\delta| \approx 0$.

In Fig. 2.3, we show the prior and posterior distributions of these two quantities. All scanned points feature $|\vec{\delta}| > 0$, such that at least one of the NMFV parameters is sizeable and non-vanishing. The second quantity is in general large and negative so that at least one of the NMFV parameters has to be small. However, since the distribution shows a peak around $\log|\Pi_\delta| \approx -7$, it is clear that a large fraction of the scanned points exhibit seven non-vanishing (with some sizeable) NMFV parameters.

As a final remark, no significant correlations between different NMFV-parameters have been found in the present analysis, see Ref. [88] for details.

Distributions of squark masses and flavour contents

After the discussion of the flavour-violating parameters of the theory, we now turn to the distributions of the physical squark masses, their flavour decompositions, and the mass differences between states relevant for phenomenology at the *Large Hadron Collider (LHC)*. Figure 2.4 shows the prior and posterior distributions of the up-type squark masses. The shapes of the distributions for the two lightest states, $\tilde{u}_1$ and $\tilde{u}_2$, are very similar and they both peak at about 800 - 1000 GeV. These two states are mostly of the first and second generation, are in general relatively close in mass, which is due to the choice of common mass parameters $M_{\tilde{Q}_{1,2}}$, $M_{\tilde{U}_{1,2}}$, and $M_{\tilde{D}_{1,2}}$.

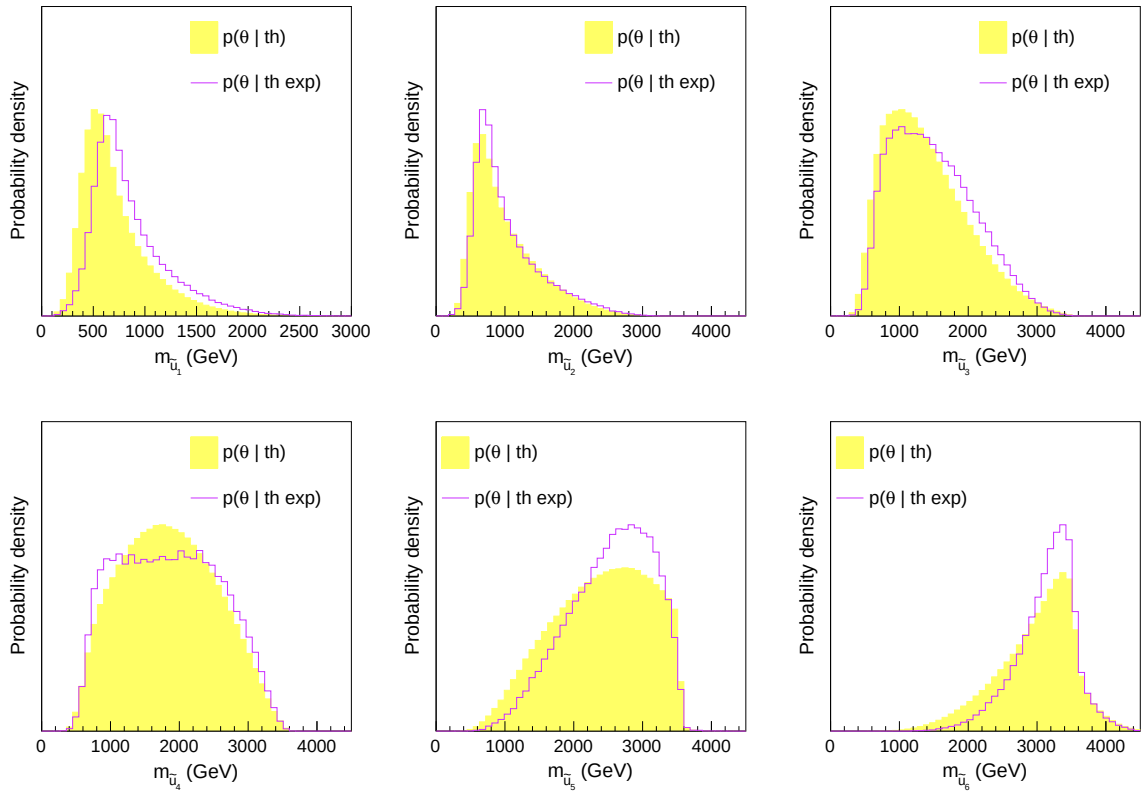

FIGURE 2.4: The one-dimensional prior (yellow histogram) and posterior (violet curve) distributions of the masses of the six up-type squarks.

The heavier states $\tilde{u}_3$, $\tilde{u}_4$, and $\tilde{u}_5$ exhibit more spread distributions, their masses ranging from 1 to 3.5 TeV. Finally, the heaviest state $\tilde{u}_6$ is barely reachable at the LHC with a mass in general above 2 TeV. Although the considered experimental constraints affect all NMFV parameters, the associated effects on the mass eigenvalues is at the end only mild, the mass distributions being only slightly shifted towards higher values.

From a phenomenological point of view, it is interesting to examine the flavour content – in particular the stop content – of the six up-type squark mass eigenstates. It appears that the lighter states $\tilde{u}_1$, $\tilde{u}_2$, and $\tilde{u}_3$ are mainly not stop-like, i.e. they have significant up- or charm-components. Most scenarios appearing in our scan indeed exhibit a charm-dominated lightest squark $\tilde{u}_1$, while $\tilde{u}_2$ is mostly dominated by its up component. This clearly contrasts with the "usual" flavour-conserving MSSM, where the lightest squark state is typically a stop. This difference can be traced to the first and second generation soft masses that are driven to lower values as explained in Sec. 2.2, while the third generation soft masses are pushed towards higher values by the flavour constraints. Furthermore, even in the presence of trilinear terms, the lightest states are still found to be mainly up- or charm-like. This feature will become important in the discussion presented in Sec. 3.3.

Similar conclusions hold for the sector of the down-type squarks. The three lighter states $\tilde{d}_1$, $\tilde{d}_2$, and $\tilde{d}_3$ exhibit comparable distributions, peaking as for the up-type squarks at about 800 - 1000 GeV. The masses of $\tilde{d}_4$ and $\tilde{d}_5$ feature distributions with a larger spread, and the one of the heaviest squark $\tilde{d}_6$ is peaking at about 3 TeV, although masses of about 1 TeV are predicted for a small subset of scenarios. Flavour mixing in the down-type squark sector is generally less pronounced than for the up-type squarks. A majority of scenarios include light down- and stange-like states, and there is only a small number of parameter points where $\tilde{d}_1$ and $\tilde{d}_2$ feature a sizeable sbottom content.

Since the analyses discussed in the following will focus on the sector of up-type squarks, the phenomenology of the down-type sector is not developed further here. The interested reader can find more details on the down-type squark masses and flavour composition in Ref. [88].

Chapter 3

Exploring squark generation mixing at the LHC

Having shown that Non-Minimally Flavour Violating (NMFV) terms may be present in the Lagrangian without infringing the divers constraints on the parameter space, especially those coming from flavour data, it is interesting to turn towards the related signatures at colliders, in particular the Large Hadron Collider (LHC). In the present Chapter, I will discuss specific signatures stemming from NMFV-terms together with their implications on present and future searches for squarks.

For the sake of simplicity, but without loss of generality, I will discuss these topics within a simplified model of two squark mass eigenstates, $\tilde{u}_1$ and $\tilde{u}_2$, which are admixtures of "right-handed" top- and charm-flavour. The general up-squark mass matrix of Eq. (1.33) then reduces to

$$\mathcal{M}^2_{\tilde{u}} = \begin{pmatrix} M^2_{\tilde{c}_R} & M^2_{tc} \\ M^2_{tc} & M^2_{\tilde{t}_R} \end{pmatrix} \qquad \text{with} \qquad \delta_{tc} = \frac{M^2_{tc}}{\sqrt{M^2_{\tilde{c}_R} M^2_{\tilde{t}_R}}}, \tag{3.1}$$

where the parameter δ_{tc} parametrized the flavour mixing in the same way as introduced in Eqs. (1.39). The rotation between the flavour and the mass eigenbasis can be expressed as

$$\begin{pmatrix} \tilde{u}_1 \\ \tilde{u}_2 \end{pmatrix} = \begin{pmatrix} \cos\theta_{tc} & \sin\theta_{tc} \\ -\sin\theta_{tc} & \cos\theta_{tc} \end{pmatrix} \begin{pmatrix} \tilde{c}_R \\ \tilde{t}_R \end{pmatrix} \qquad \text{with} \qquad m_{\tilde{u}_1} < m_{\tilde{u}_2}\,. \tag{3.2}$$

i.e. through introducing the mixing angle θ_{tc}. Note that the mixing angle is related to the NMFV-parameter δ_{tc} in a non-linear way. The simplified setup considered here is completed by a bino-like neutralino $\tilde{\chi}^0$, which in view of the dark matter requirement is lighter than the two squarks, and thus will appear in their respective decays.

In this setup, the physical masses as well as the flavour decomposition of the two squark eigenstates depends on the mixing angle θ_{tc}. The dependence of the two key characteristics on θ_{tc} is depicted in Figure 3.1, where for illustration purposes the diagonal parameters of the mass matrix have been fixed to $M_{\tilde{c}_R} = 500$ GeV and $M_{\tilde{t}_R} = 1000$ GeV, respectively. As can be seen, the mass splitting increases for increasing flavour-mixing angle. At the same time, the lightest squark state receives an increasing admixture of top-flavour, the case $\theta_{tc} = 0$ corresponding to a pure charm-flavoured state. In this simplified model, the second squark eigenstate $\tilde{u}_2$ features the opposite flavour content (not depicted in Figure 3.1). As we will see in the following, the mixing angle has an important impact on the production cross-section as well as the subsequent decay channels of the lightest squark, which will be the particle of interest.

The dominant production mode of the lightest up-type squark $\tilde{u}_1$ at the LHC is squark-antisquark production, depicted in terms of Feynman diagrams in Fig. 3.2. The production can

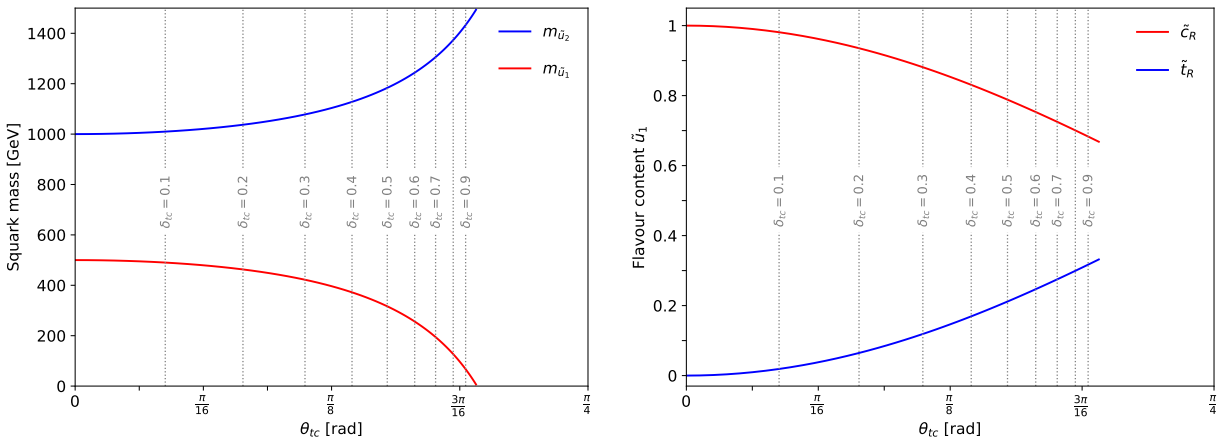

FIGURE 3.1: Physical masses of the two squarks $\tilde{u}_1$ and $\tilde{u}_2$ (left) together with the flavour content of the lighter mass eigenstate $\tilde{u}_1$ (right) as a function of the mixing angle θ_{tc} for fixed soft mass parameters $M_{\tilde{c}_R} = 500$ GeV and $M_{\tilde{t}_R} = 1000$ GeV. The heavier state $\tilde{u}_2$ features the inverse flavour content. The vertical lines indicate the corresponding values of δ_{tc} defined in Eq. (3.1).

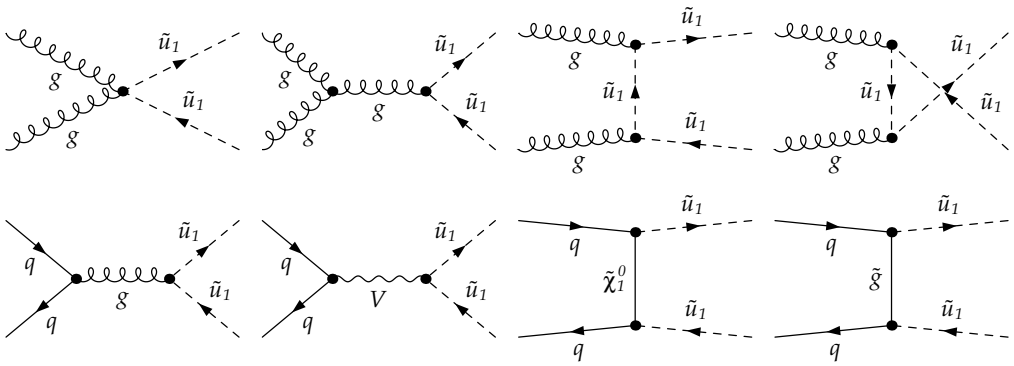

FIGURE 3.2: Feynman diagrams associated to squark-antisquark pair production at the Large Hadron Collider. The diagrams involving gluons are "flavour-blind", while the remaining ones are sensitive to flavour-violating terms.

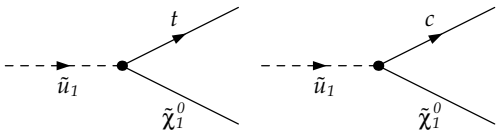

FIGURE 3.3: Feynman diagram associated to the decay of the lighter squark into a quark and a neutralino.

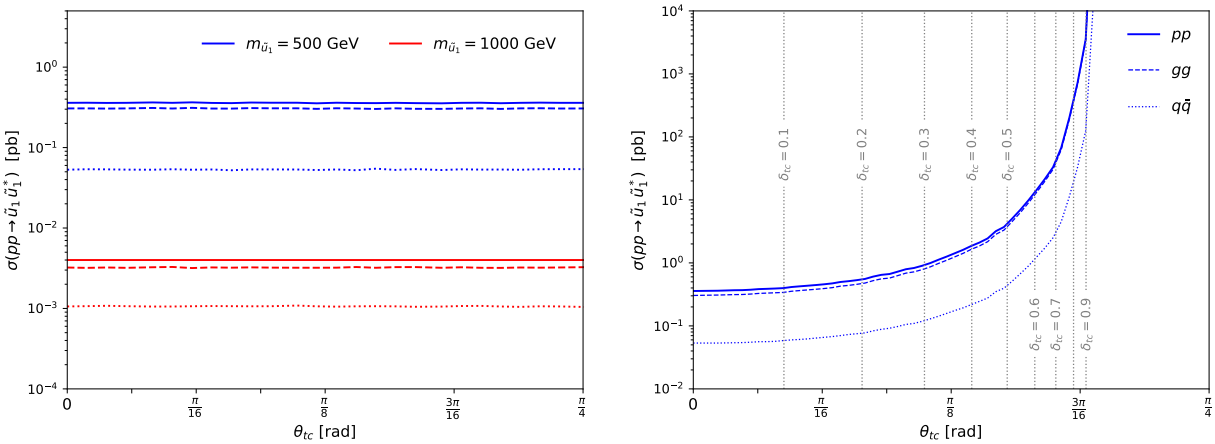

FIGURE 3.4: Production cross-section obtained using `MadGraph5_aMC@NLO` for a centre-of-momentum energy $\sqrt{s} = 13$ TeV as function of the flavour mixing angle θ_{tc} for fixed physical squark masses $m_{\tilde{u}_1} = 500$ GeV and $m_{\tilde{u}_2} = 1000$ GeV (left) and for fixed soft mass parameters $M_{\tilde{c}_R} = 500$ GeV and $M_{\tilde{t}_R} = 1000$ GeV (right). In each panel, the solid line corresponds to the total cross-section, while the dashed and dotted indicate the gluon- and quark-initiated contributions, respectively.

be initiated from gluon fusion or from quark-antiquark pairs. At the LHC, the former are dominant because of the important parton densities of the gluon within the colliding protons. Moreover, the gluon-initiated and gluon-mediated diagrams are "flavour-blind", i.e. insensitive to flavour violating elements of the mass matrix. In contrast, the remaining diagrams involving Higgs bosons, electroweak vector bosons, gauginos, or gluinos may be affected by the presence of flavour violation. For fixed squark masses, we can therefore expect a mild dependence on the NMFV-parameter δ_{tc} or the mixing angle θ_{tc}. This behaviour is confirmed by the first panel of Fig. 3.4, where the production cross-section is shown as computed at leading-order accuracy using `MadGraph5_aMC@NLO` [126].

The situation is different if the production cross-section is computed from the soft mass parameters instead directly from the physical masses. In this case, the cross-section calculation is preceded by the diagonalization of the mass matrix. As shown above (see Fig. 3.1), this step strongly depends on the imposed flavour mixing. The cross-section then indirectly depends on the mixing angle through the squark mass eigenvalues. The resulting cross-section is depicted, again as a function of the mixing angle, in the second panel of Fig. 3.4, where the soft mass parameters have again been fixed to $M_{\tilde{c}_R} = 500$ GeV and $M_{\tilde{t}_R} = 1000$ GeV. As can be seen, with increasing mixing angle, i.e. with decreasing squark mass $m_{\tilde{u}_1}$, the cross-section may increase by several orders of magnitude in the case of large flavour-violating elements $\delta_{tc} \gtrsim 0.5$.

Let us now turn to the subsequent decay of the produced squark. Each squark can decay either into a top- or a charm-quark plus a neutralino $\tilde{\chi}_1^0$,

$$\tilde{u}_i \;\to\; t\,\tilde{\chi}_1^0\,, \qquad \tilde{u}_i \;\to\; c\,\tilde{\chi}_1^0\,, \tag{3.3}$$

for $i = 1, 2$ in the simplified model under consideration. The corresponding Feynman diagrams are shown in Fig. 3.3. It is to be noted that both decay channels are simultaneously open, which is in contrast to the often assumed Minimal Flavour Violation (MFV) paradigm featuring single-flavoured squark states. The associated decay widths and branching fractions are rather sensitive to flavour-violating elements, as the flavour content of the squark governs the interaction responsible for the decay. The dependence of the branching ratios on the flavour mixing angle θ_{tc} is shown in Fig. 3.5 for different mass configurations. This shows that indeed the impact of the mixing angle is dominant, while the involved squark and neutralino masses

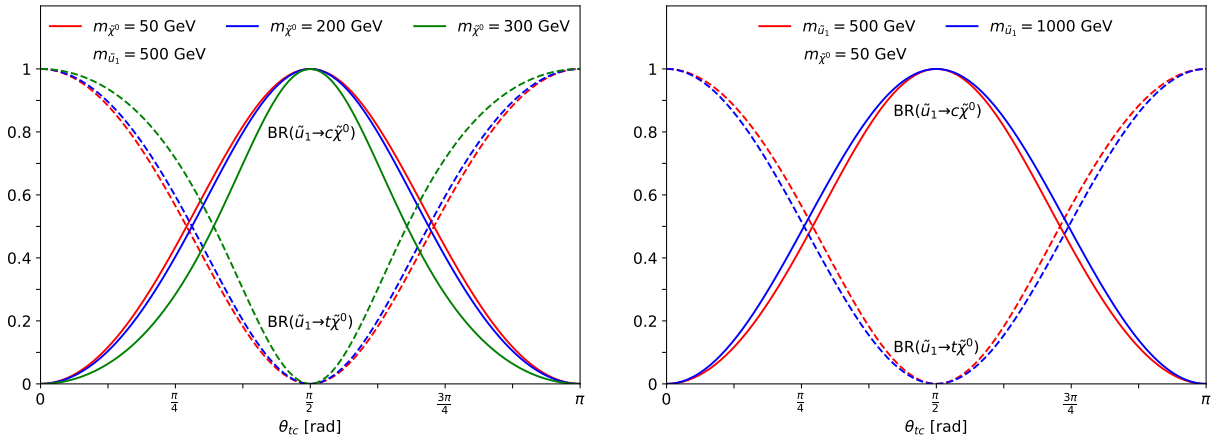

FIGURE 3.5: Branching ratios associated to the squark decays into quarks and a neutralino in the simplified model under consideration. The squark and neutralino masses are fixed as shown in the legend.

play a less important role, unless the mass difference becomes too close to the kinematical threshold of the decay into the top quark. Again, I would like to emphasize that for maximal mixing, both decay modes are equally important, which will lead to characteristical collider signatures.

Assuming MFV, i.e. single-flavoured squark states, the resulting signatures at the Large Hadron Collider correspond to the production of a squark-antisquark pair, each of which will decay into the same quark flavour plus a neutralino,

$$\begin{aligned} pp &\to \tilde{u}_i \tilde{u}_i^* \to t\bar{t}\,\tilde{\chi}_1^0\tilde{\chi}_1^0, \\ pp &\to \tilde{u}_i \tilde{u}_i^* \to c\bar{c}\,\tilde{\chi}_1^0\tilde{\chi}_1^0, \end{aligned} \tag{3.4}$$

where the neutralinos in the final state manifest as missing transverse energy ($\not{E}_T$). Going beyond the MFV paradigm, i.e. taking into account the possibility that the squarks may contain two flavours such that both decay channels given in Eq. (3.3) are open, gives rise to the additional signature [102]

$$pp \to \tilde{u}_i \tilde{u}_i^* \to t\bar{c}\,\tilde{\chi}_1^0\tilde{\chi}_1^0 + c\bar{t}\,\tilde{\chi}_1^0\tilde{\chi}_1^0, \tag{3.5}$$

which is characteristic for Non-Minimal Flavour Violation.

In the Sections 3.1 and 3.2, I am going to discuss the above signatures in the context of non-zero flavour mixing parameters δ_{tc} and θ_{tc}, respectively. The following two Sections are the fruit of a collaboration initiated by myself during the 2017 *PhysTeV Les Houches* workshop [127]. The corresponding results have been published in Ref. [128]. More details on the NMFV signature of Eq. (3.5) and other related collider signatures can be found in Refs. [72, 73, 74, 102, 104, 103, 105].

Going a step further and assuming the actual observation of a squark-like state at the LHC, the subsequent Sections 3.3 to 3.4 are dedicated to the question how to identify the squark's flavour content. I will present two methods aiming at the determination of, e.g., the top-flavour content, and the underlying flavour paradigm. This discussion is based on Ref. [111].

3.1 Recasting of LHC limits on squark and neutralino masses

The ATLAS and CMS collaborations have performed several direct searches for top- and charm-flavoured squarks, mostly in setups where the squarks are produced by pairs and subsequently

decay into quarks plus neutralinos, where the latter manifest as missing transverse energy. This situation corresponds to the possibilities assuming Minimal Flavour Violation (MFV) given in Eqs. (3.4). In the absence of any direct hint for new physics, especially in the channels under consideration in this Chapter, the most stringent constraints arise from the analyses of data obtained during Run 2 of the Large Hadron Collider at a centre-of-momentum energy of 13 TeV [129, 130, 131, 132, 133, 134, 135, 136, 137, 138, 139, 140]. For top-flavoured squarks, the searches have lead to exclusion limits of the order of 1 TeV for the stop mass. Bounds on first and second generation squarks are of similar order if single squarks are considered, but increase to about 1.5 TeV if four mass-degenerate squarks are assumed [141, 142].

The most sensitive searches for top-flavoured squarks, yielding a similar expected sensitivity for low neutralino masses, are the ones addresses final states with either zero or one lepton. In order to obtain conversative constraints on the model presented above, we therefore choose the recent ATLAS search of top squarks in final states with one lepton of Ref. [140] as a benchmark. Coming to final states containing charm quarks, the ATLAS collaboration has carried out an analysis corresponding to this situation and targeting either top- or charm-flavoured squarks [143]. As this signature is expected to play a significant role for getting handles on the inter-generational mixing in our model, we use the analysis of Ref. [143] as a second benchmark to evaluate the existing constraints on simplified setup under consideration here. The ATLAS limits corresponding to the two benchmark analyses are shown in Fig. 3.6 and 3.7 in the respective squark-mass neutralino mass planes. The same Figures show the corresponding limits obtained from the CMS collaboration. As can be seen, the limits are comparable between the two experiments, and in the following only those obtained from the ATLAS collaboration will be used.

In order to recast these limits obtained by the ATLAS collaboration into our simplified model for non-minimal top-charm mixing in the squark sector, we perform a three-dimensional scan over the relevant parameter space. More precisely, we vary independantly the two squark masses $m_{\tilde{u}_1}$ and $m_{\tilde{u}_2}$ as well as the top-charm mixing angle θ_{tc}. Following the results depicted in Fig. 3.5, we fix the neutralino mass to $m_{\tilde{\chi}_1^0} = 50$ GeV. Our results are therefore valid if the squarks are much heavier than the neutralino. For each parameter point of the scan, the sensitivity of the two benchmark analyses of Refs. [140, 143] has been evaluated. Concerning the stop analysis, we rely on the acceptences and efficiencies that have been officially provided by the ATLAS collaboration for each of the "discovery tN_med" and "discovery tN_high" regions, targeting moderate and high squark masses, respectively. The two corresponding signal yields (N_{sig}) have been estimated considering next-to-leading-order (NLO) stop pair-production cross-sections corrected by the resummation of the threshold logarithms at the next-to-leading logarithmic (NLL) accuracy [145] and the appropriate branching ratios (see Fig. 3.5). These signal yields are then compared to the ATLAS model-independent upper limit ($N^{\text{obs}}_{\text{non-SM}}$) for each of the two regions. If the ratio of the two yields exceeds one, the signal point is considered excluded. While providing acceptance and efficiency values only for the inclusive "signal" regions, the ATLAS analysis employs a multi-bin fit in the most sensitivie distribution for the final exclusion limit estimation. For this reason, the presented recast represents a conservative estimate of the effective reach of the ATLAS search. The same procedure has lead to the extraction of the constraints from the charm-tagging search of Ref. [143].

The obtained exclusion limits for the simplified NMFV-model are presented in Fig. 3.8 for the situation where the top-charm mixing is maximal, i.e. $\theta_{tc} = \pi/4$. The obtained exclusion limit is presented in the plane of the two squark masses. Let us recall that $m_{\tilde{u}_1} < m_{\tilde{u}_1}$ per definition of the simplified model. The total new-physics production rate is solely driven by the lightest of the two squark states $\tilde{u}_1$, except for the region $m_{\tilde{1}} \approx m_{\tilde{u}_2}$, where the mass difference is small and both production modes contribute. For sufficiently large mass differences, the exclusion limit is thus independent of $m_{\tilde{u}_2}$, and squarks are found to be constrained to be heavier than about 550 GeV. Compared with the standard MFV case, where the bounds are of about 1

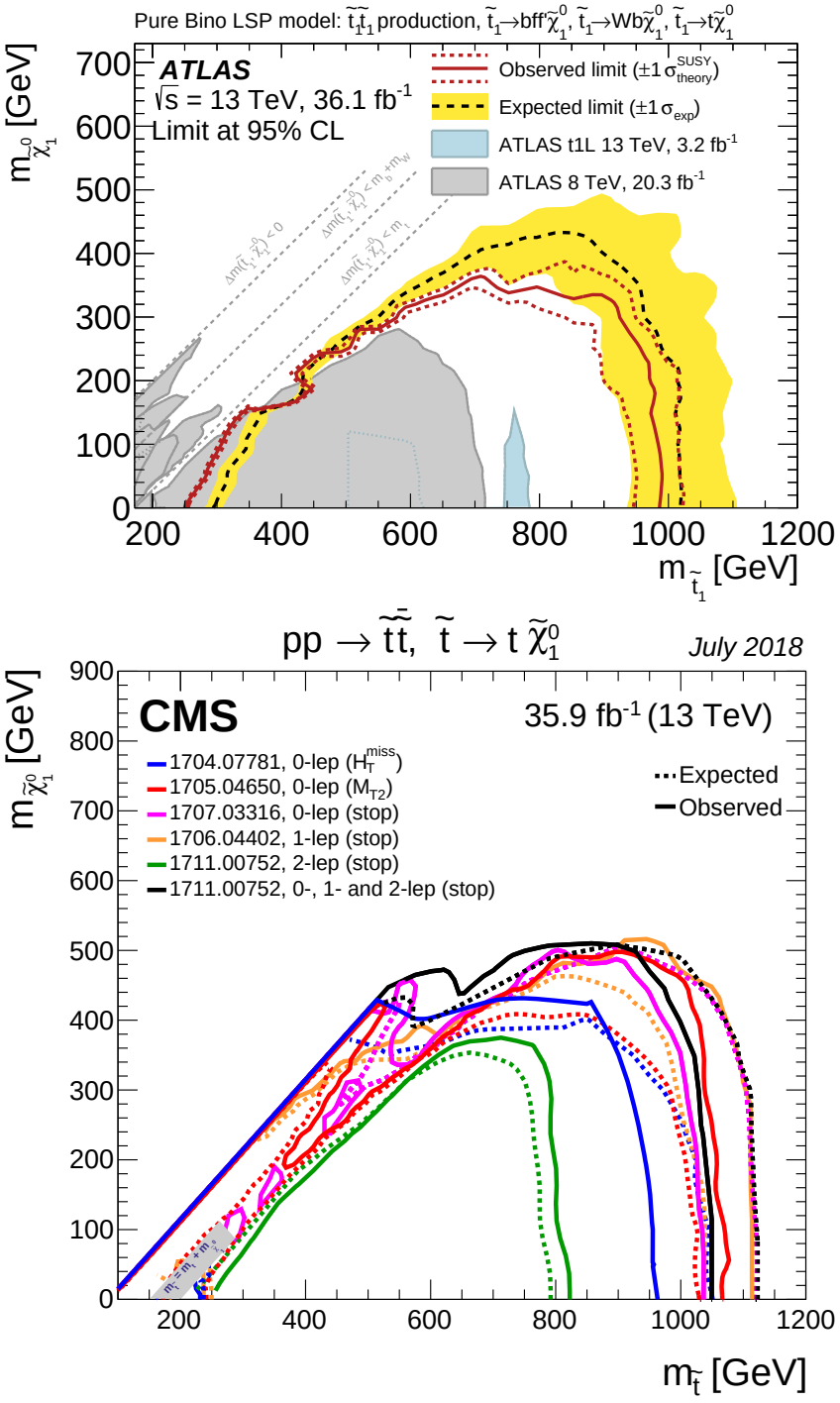

FIGURE 3.6: ATLAS limits on top-flavoured (left) and charm-flavoured (right) squark and neutralino masses assuming Minimal Flavour Violation. The shown plots are extracted from Refs. [140] and [144].

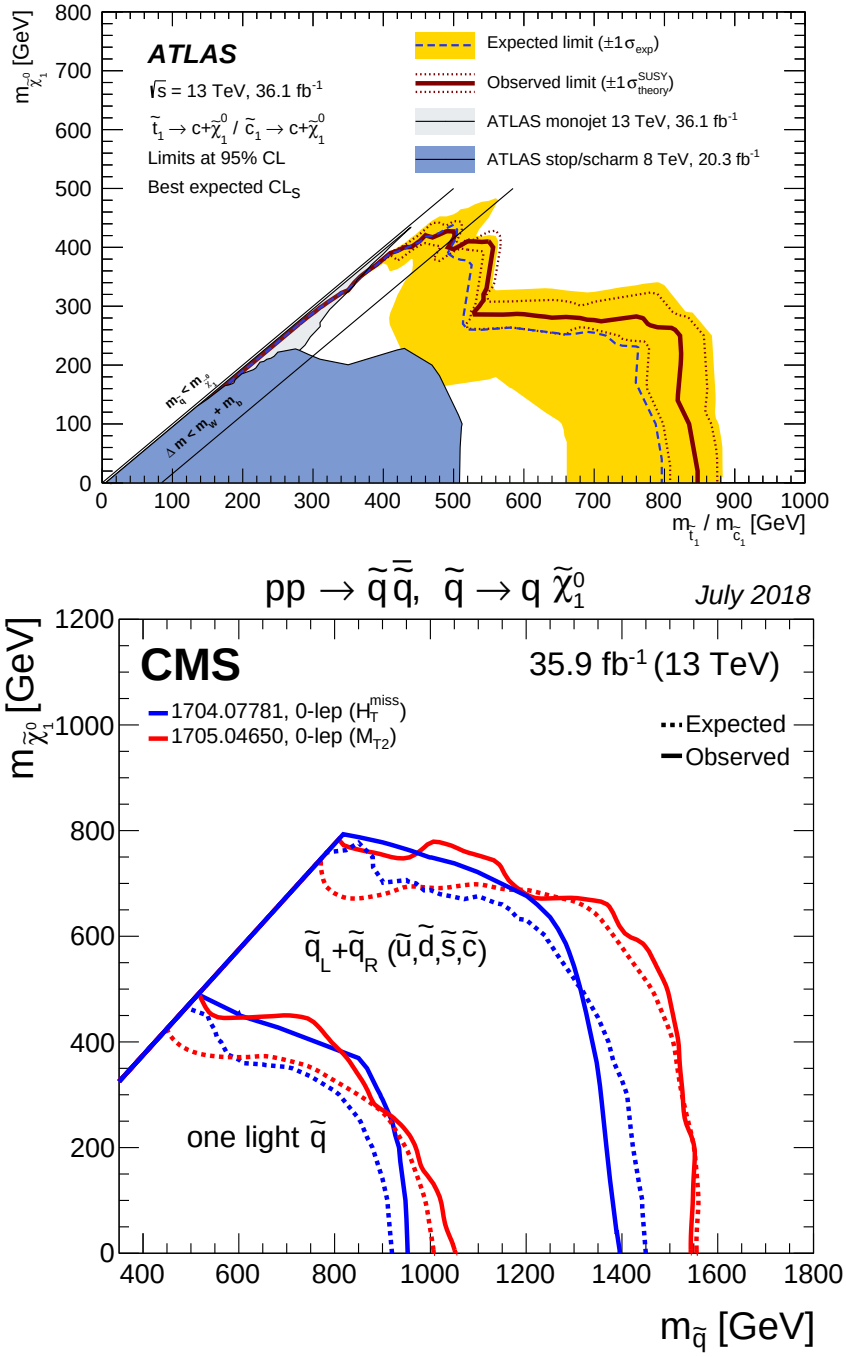

FIGURE 3.7: ATLAS limits on top-flavoured (left) and charm-flavoured (right) squark and neutralino masses assuming Minimal Flavour. The shown plots are extracted from Refs. [143] and [144].

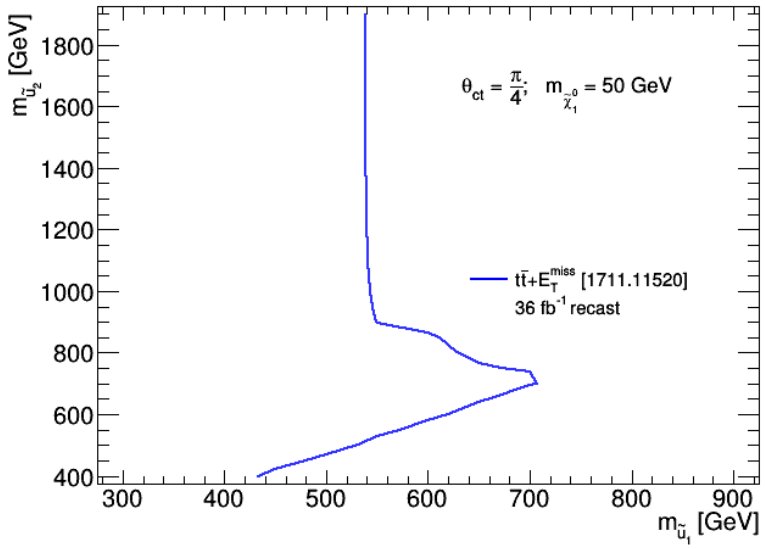

FIGURE 3.8: Recast of ATLAS limits on the squark masses assuming Non-Minimal Flavour Violation, fixing the squark mixing angle and the neutralino mass to the indicated values.

TeV, the limits are hence weakened by almost 500 GeV in this maximal-mixing scenario. The important mixing indeed implies that the two signal regions of the stop analysis of Ref. [140], specifically targeting final states with two top quarks, are less populated by virtue of the large decay fraction of the mixed squarks into charm quarks $\mathrm{BR}(\tilde{u}_1 \to c\tilde{\chi}_1^0)$.

In the complementary parameter region where

$$m_{\tilde{u}_1}\,,\; m_{\tilde{u}_2} \lesssim 750\,\mathrm{GeV}\,, \tag{3.6}$$

the situation is somewhat different, since both squark mass eigenstates $\tilde{u}_1$ and $\tilde{u}_2$ contribute to a potentially observable new physics signal. This partly compensates the loss due to the smaller branching ratio into top quarks, so that the obtained limites are stronger than in the previous case where the second state was heavier.

The charm-tagging analysis of Ref. [143] always implies weaker bounds for this specific class of scenarios, as the number of events populating the signal regions is very small. The corresponding results are therefore omitted in Fig. 3.8.

Assuming now the heavier mass eigenstate to be decoupled, Fig. 3.9 shows the reinterpretation of the ATLAS limits in the $m_{\tilde{u}_1}$-θ_{tc} plane. The obtained results exhibit the complementary effect of the top-charm mixing angle θ_{tc} on the mass bounds. For θ_{tc}, the lightest squark $\tilde{u}_1$ is a pure charm squark, so that the ATLAS stop search is insensitive to the signal and the limit of $m_{\tilde{u}_1} \lesssim 800$ GeV solely arises from the ATLAS charm-tagging analysis. With increasing mixing angle, the corresponding $c\bar{c}+\not{E}_T$ production rate decreases so that the bounds are progressively weakened.

On the other hand, the increase in the mixing angle implies that, while the signal regions of the charm-tagging analysis are more and more depleted due to the lower and lower branching ratio of the decay $\tilde{u}_1 \to c\tilde{\chi}_1^0$, the signal regions of the stop analysis are more and more populated due to the increasing branching ratio of the decay $\tilde{u}_1 \to t\tilde{\chi}_1^0$. Consequently, the bounds stemming from the latter progressively increase. In the limit of a pure top-flavoured squark, i.e. for $\theta_{tc} = \pi/2$, its mass is constrained to be at least 825 GeV.

For the maximimal-mixing scenario, $\theta_{tc} = \pi/4$, the mass constraints for both analyses are below 600 GeV, which is the minimum mass value for which experimental acceptances are available for both the considered benchmark analyses. Finally, Fig. 3.9 shows also the official ATLAS limits for both analyses in the MFV case. The usage of the multi-bin signal regions

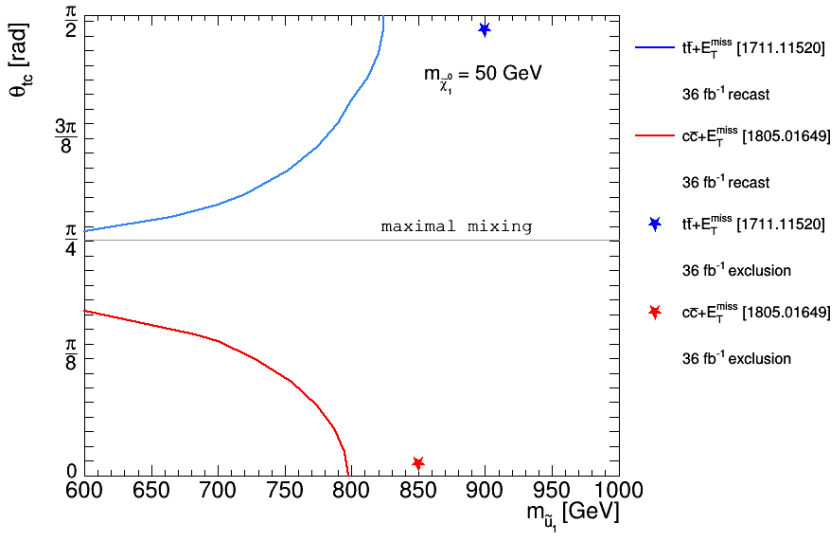

FIGURE 3.9: Recast of ATLAS limits on the squark masses assuming Non-Minimal Flavour Violation, decoupling the heavier squark state, and fixing the neutralino mass to the indicated values.

mentioned above increases the limits by about 50-100 GeV. Although such an extreme mixing configuration seems rather unlikely, due to the flavour constraints discussed in the previous Chapter, the limit is significantly lowered when moving away from the situation of MFV.

3.2 Prospects for a dedicated search at LHC

Having shown that the current experimental searches focusing on pair production of squarks that carry a well-defined flavour have a significantly reduced sensitivity to models with sizeable flavour-mixing, we now develop a dedicated analysis addressing this issue. More precisely, we propose to target the $tc+\not{E}_T$ final state, which has its maximum rate in the case of maximal mixing and is therefore complementary to the $t\bar{t}+\not{E}_T$ and $c\bar{c}+\not{E}_T$ final states targeted by previous studies. The present Section contains a description of a possible implementation of such an analysis. In particular, we focus on the case in which the top quark decays semi-leptonically, resulting in the final state

$$pp \;\to\; \ell\, b\, c\, \not{E}_T\,, \tag{3.7}$$

where the final state comprises an isolated lepton, a b-jet, a c-jet, and missing tranvserse energy stemming from two neutralinos and the neutrino from the top decay. The following study assumes proton-proton collisions a centre-of-momentum energy of 14 TeV and integrated luminosities of 300 fb^{-1} and 3000 fb^{-1}, corresponding to the expected configurations for the coming runs of the Large Hadron Collider.

Before discussing the analysis proposal in more detail, Fig. 3.10 shows the production cross-section (as shown in Fig. 3.4) multiplied with the appropriate branching ratios (as shown in Fig. 3.5) for centre-of-momentum energies of 7 and 14 TeV at the Large Hadron Collider. While the cross-section is zero in the case of Minimal Flavour Violation ($\theta_{tc} = 0$ and $\theta_{tc} = \pi/2$), it reaches sizeable values already for relatively small mixing angles (here expressed in terms of the NMFV parameter $(\delta^u_{RR})_{23}$). This illustrates that a non-negligible number of events can be expected, e.g., around 10^4 events for a squark mass of about $m_{\tilde{u}_1} \approx 500$ GeV and an integrated luminosity of about $\mathcal{L}_{\int} \approx 100$ fb^{-1} [102].

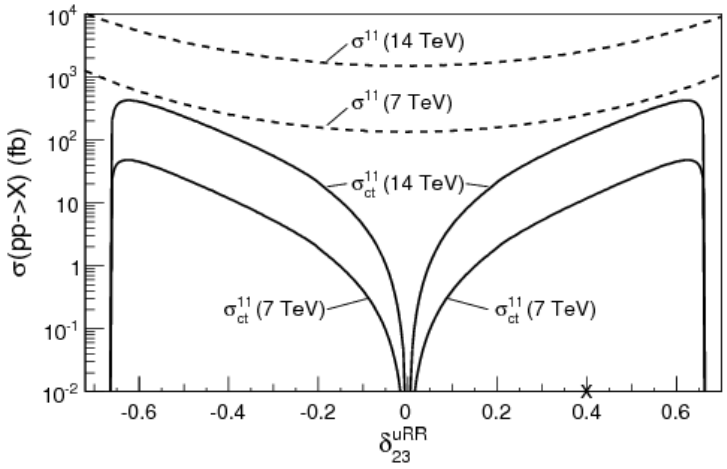

FIGURE 3.10: Squark-pair production cross-section with (solid lines) and without (dashed lines) the branching fraction into quarks and a neutralino for centre-of-momentum energies of $\sqrt{s} = 7$ TeV and $\sqrt{s} = 14$ TeV as a function of the flavour-violating parameter $\left(\delta^u_{RR}\right)_{23}$ in the notation of Eq. (1.39). The shown plot is taken from Ref. [102].

In order to simulate the corresponding signal, the simplified model presented above has been implemented into `FeynRules 2.0` [146, 147] to obtain a `UFO` model [148] to be used with the `MadGraph5_aMC@NLO` framework [126]. Leading-order (LO) hard-scattering matrix elements have been generated for squark pair-production and subsequent decay, and have been convoluted with the leading-order set of `NNPDF 3.0` parton distribution functions [149]. Parton showering and hadronisation have been handled with `PYTHIA 8.2` [150, 151]. Each event has been reweighted so that the corresponding total rate matches the production cross-section estimated at the NLO+NLL accuracy [145].

The relevant parameter space of the model is covered by means of a grid, the lightest squark nass being varied in the $m_{\tilde{u}_1} \in \left[600\text{ GeV}, 1.5\text{ TeV}\right]$ window by steps of 100 GeV, and the neutralino mass in the $m_{\tilde{\chi}^0_1} \in \left[50\text{ GeV}, 900\text{ GeV}\right]$ window by steps of 50 GeV for $m_{\tilde{\chi}^0_1} < 400$ GeV and of 100 GeV above. The squark mixing angle is fixed to $\theta_{tc} = \pi/4$, corresponding to the maximal mixing scenario. The heavier squark is again assumed to be decoupled.

The Standard Model processes which can mimic the targeted signature of Eq. (3.7) involve one or two leptons originating either from the decay of a W- or Z-boson, or from tau leptons decaying leptonically. In consequence, we generate events for Standard Model $t\bar{t}$, Wt, t-channel single top, $t\bar{t}W$, $t\bar{t}Z$, tWZ, tZ, $W+$jets, $Z+$jets, WW, WZ, and ZZ production. For $t\bar{t}$, single top and diboson processes, events are simulated at NLO accuracy in QCD within the `POWHEG BOX` framework [152]. Samples for the remaining processes are then generated at leading order, using `MadGraph5_aMC@NLO`. All those events are reweighted so that the total rates match the next-to-next-to-leading-order (NNLO) cross-sections if available, or the NLO ones otherwise.

Furthermore, appropriate jet reconstruction algorithms [153, 154, 155] and b- and c-jet identification criteria are employed, and detector effects are incorporated such that they reproduce the performance of the ATLAS detector [156, 157, 158], especially concerning the b- and c-tagging efficiencies [159, 160]. Moreover, an appropriate event preselection for the envisaged signal structure has been defined. For a detailed description of the technical details of the proposed analysis, including the kinematic cuts, the reader is referred to Ref. [128].

Most of the backgrounds to the process under consideration exhibit two b-jets in the final state, while the targeted signal features one b-jet and one c-jet. Two strategies can be envisaged to seperate the signal from the backgrounds. The first possibility is to veto the presence of any additional b-jet, which will here be labelled strategy A. The second possibility is to enfore the

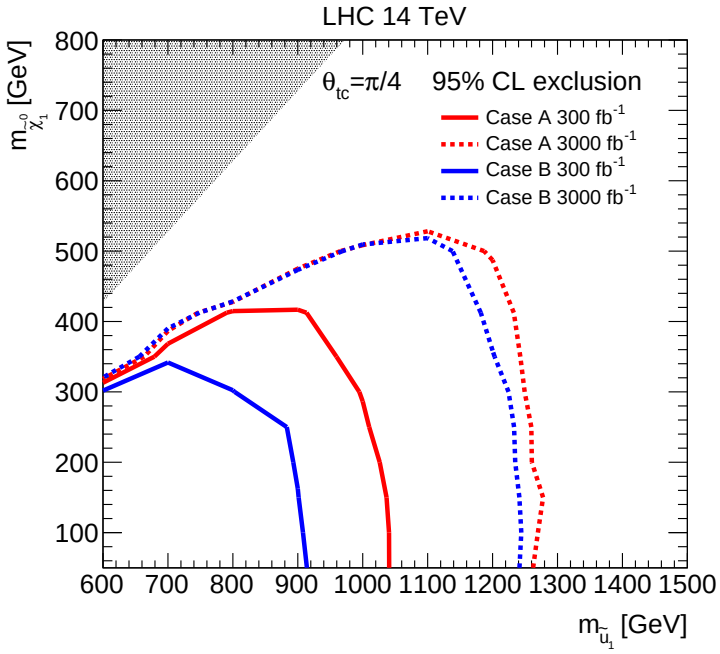

FIGURE 3.11: Prospected reach of dedicated NMFV search in the plane of the squark and neutralino masses for the two strategies A (no c-tagging, red) and B (with c-tagging, blue), for 300 fb^{-1} and 3000 fb^{-1} of integrated luminosity, assuming maximal top-charm mixing.

presence of an extra c-jet, which will here be labelled strategy B. Simple calculations based on efficencies show that the signal over background ratio will be improved by a factor of about 1.5 more for the strategy B, but the price to pay will be an overall reduction of statistics by a factor of approximately 3. In the following, results for both strategies will be presented. For additional information such as the associated cuts the reader is again referred to Ref. [128].

On the basis of the analysis strategy outlined above, we estimate the sensitivity of the Large Hadron Collider to supersymmetric scenarios featuring mixed top-charm squarks with 300 fb^{-1} and 3000 fb^{-1} of integrated luminosity. For the latter configuration, we assume no modification in the detector performances for the high-luminisity LHC. The sensitivity can be extracted by means of a test statistics based on a profiled likelihood ratio. In the present analysis, this has been realized based on the CLs method [161] to obtain 95% confidence level exclusion limits. The statistical analysis is performed with the `ROOSTAT` toolkit [162] assuming systematic uncertainties of 20% and 5% on the Standard Model background and the signal, respectively. The results are presented in terms of upper limits, at the 95% confidence level, on the ratio of the signal yields to the corresponding benchmark predictions, denoted as $\sigma^{\text{excl}}/\sigma^{\text{SUSY}}$.

The obtained analysis reach is shown in Fig. 3.11 for the case of maximal mixing, $\theta_{tc} = \pi/4$, in the same squark-neutralino mass plane as the ATLAS limits presented in Figs. 3.6 and 3.7 of the previous Section. As complementary information, and in order to better understand the relative performance of the two analysis strategies, the dependence of the signal over background ratio on the squark mass is shown in Fig. 3.12 for the case of maximal mixing and assuming that the relevant kinematic cuts have been applied. As expected, the signal over background ratio is higher when charm-tagging is incorporated. However, the expected reach is lower for the case including charm-tagging, especially for the case of lower integrated luminosity, 300 fb^{-1}, as can be seen in Fig. 3.11. For a neutralino mass of 50 GeV, The expected upper limit on the squark mass is 1050 GeV for strategy A (without c-tagging) against 920 GeV for strategy B (with c-tagging). This difference can be traced to the fact that the analysis is dominated by statistics, which is lower for the charm-tagging strategy. Consequently, the difference in the

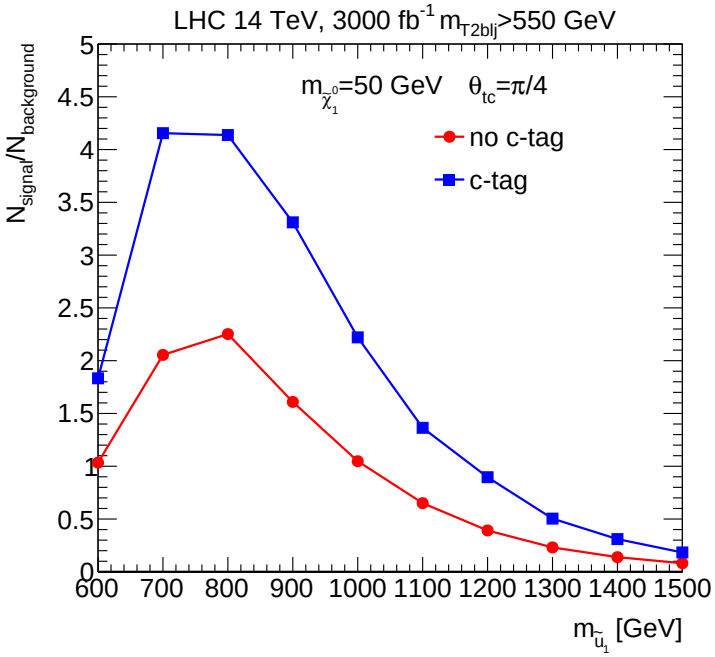

FIGURE 3.12: Signal over background ratio as function of the squark mass $m_{\tilde{u}_1}$ for the two strategies A (no c-tagging, red) and B (with c-tagging, blue), for 3000 fb^{-1} of integrated luminosity, assuming maximal top-charm mixing.

reach of the two strategies is less pronounced for a higher integrated luminosity of 3000 fb^{-1}. In this case the reach is about 1280 GeV for the strategy A (without c-tagging) and about 1240 GeV for strategy B (with c-tagging).

The results of the recasting presented in the previous Section and expected reach of the dedicated analysis presented here are summarized in Fig. 3.13. More precisely, the recasts of the 13 TeV exclusion limits obtained by the ATLAS experiment with 36 fb^{-1} (see Fig. 3.9) are overlaid with the expected exclusion limits of the dedicated analysis of the $tc+\not{E}_T$ signal. This figure clearly illustrates the strength of the proposed analysis, since it covers a region of the parameter space which is not accessible with current searches relying on the MFV paradigm.

More generally, the study presented in this Chapter, although relying on a simplified model, nicely illustrates the limits of current experimental searches. In a non-"vanilla" case, i.e. if the new physics model does not correspond to the assumptions which the experimental search is based on, new states quite likely escape detection even if they are relatively light and can thus be produced at the Large Hadron Collider. It will therefore be of great importance to widen the search horizon in order to cover a larger, and in my opinion more realistic, part of the new physics parameter space.

3.3 Identifying the squark flavour structure in a simplified model

In the previous Section, a dedicated search strategy for the caractestical NMFV signature has been discussed. In particular, strategies with and without explicit charm-tagging have been compared. This study has shown that including dedicated searches for non-minimally flavour violating configurations would improve the coverage of the supersymmetric parameter space.

Going a step further, and assuming that a squark-like state will be observed at the Large Hadron Collider, a crucial question will be to identify its flavour content. This will not only provide valuable information on the particle spectrum at the TeV scale, but is an equally important question in the context of Grand Unified Theories, where the flavour structure may be

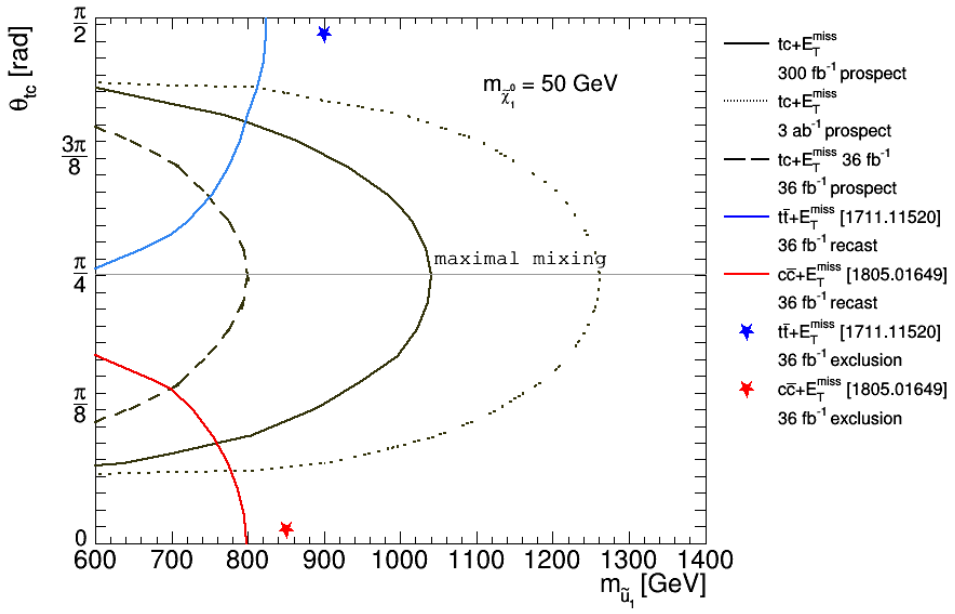

FIGURE 3.13: Present and expected exclusion limits in the $m_{\tilde{u}_1}$-θ_{tc} plane of the simplified NMFV model under consideration.

generated at the high scale. On the basis of the study of NMFV signatures presented in the previous Chapter, the comparison of results stemming from analyses with and without charm-tagging, or relying on different charm-tagging working points could be used to get information on the flavour content of the observed squark [128].

While such a study is definititely worth to be pursued, the present Section is dedicated to the discussion of two alternative methods: the first based on likelihood inference, the second relying on a multivariate analysis. These two analyses will again rely on the pair-production of squarks, which are potential mixtures of top and charm flavour, and their subsequent decays into either a top- or a charm-quark plus missing energy. An additional decay channel to be taken into account is the decay into a bottom quark and a chargino, mediated through the CKM matrix. A direct reconstruction of, e.g., the associated mass matrix and thus the flavour structure would in principle be possible, provided that there is experimental access to the corresponding branching ratios, potentially with the help of top-polarization measurements, plus complete information on the sector of neutralinos and charginos. In practice, however, having precise enough information on the latter, is not a realistic option. We therefore seek to develop methods to infer on the top-flavour content of the observed squark, defined as

$$x_{\tilde{t}} \;=\; \left(\mathcal{R}_{\tilde{u}}\right)^2_{13} + \left(\mathcal{R}_{\tilde{u}}\right)^2_{16}, \tag{3.8}$$

keeping in mind that $\left(\mathcal{R}_{\tilde{u}}\right)^2_{13}$ and $\left(\mathcal{R}_{\tilde{u}}\right)^2_{16}$ correspond to the percentage of "left-handed" and "right-handed" top-flavour within the lightest squark eigenstate $\tilde{u}_1$. The goal of the present study is to obtain valuable information on the flavour structure based on as few information as possible.

Let us note that for the sake of simplicity, only additional top-charm mixing is considered here. This can be motivated by the fact that charm-top mixing is least constrained (see Sec. 2.2). Moreover, squarks containing top flavour are easier to handle from the experimental point of view, since they may decay into top quarks which are easy to identify. However, the methods presented in this Chapter can be generalised to the more general mixing pattern involving the first generation, or be directly translated to the sectors of down-type squarks or sleptons.

In the case where a squark should be observed at the Large Hadron Collider or any future

hadron collider, as discussed in the beginning of the present Chapter, it will most likely be produced from (flavour-conserving) gluon-initiated processes and manifest through its decays into quarks and gauginos. As indicated above, in the present context, the decay modes of interest are

$$\tilde{u}_1 \;\to\; t\,\tilde{\chi}_1^0\,, \qquad \tilde{u}_1 \;\to\; c\,\tilde{\chi}_1^0\,, \qquad \tilde{u}_1 \;\to\; b\,\tilde{\chi}_1^+\,, \tag{3.9}$$

which are simultaneously open if the squark is a mixture of top and charm flavour, i.e. if $0 < x_{\tilde{t}} < 1$. The neutralinos manifest as missing transverse energy, while the chargino decays further into W-bosons and neutralinos.

The following studies are based on the assumption that these decays are observed, and that the following observables can be experimentally accessed:

$$m_{\tilde{u}_1}\,, \quad m_{\tilde{\chi}_1^0}\,, \quad m_{\tilde{\chi}_0^\pm}\,, \quad R_{c/t} = \frac{\mathrm{BR}\big(\tilde{u}_1 \to t\tilde{\chi}_1^0\big)}{\mathrm{BR}\big(\tilde{u}_1 \to c\tilde{\chi}_1^0\big)}\,, \quad R_{b/t} = \frac{\mathrm{BR}\big(\tilde{u}_1 \to b\tilde{\chi}_1^+\big)}{\mathrm{BR}\big(\tilde{u}_1 \to c\tilde{\chi}_1^0\big)}\,. \tag{3.10}$$

Note that the production cross-section of the squarks, as well as their branching ratios alone, are difficult to access experimentally. It is therefore convenient to work with the ratios $R_{c/t}$ and $R_{b/t}$ rather than with the pure associated event rates. Analytical expressions for the corresponding decay widths in the framework of Non-Minimal Flavour Violation can be found in Ref. [72]. Finally, note that in the definition given in Eq. (3.10) it is assumed, without the loss of generality, that the decay into top quarks is always open.

In view of the analysis presented here, it is interesting to examine the expressions given in Eq. (3.10) in order to exhibit their dependence on the stop-flavour content $x_{\tilde{t}}$, which is the target of the present study, assuming certain limits concerning the nature of the involved neutralino and chargino. For example, assuming a pure higgsino-like neutralino and neglecting the neutralino mass with respect to the squark mass, we obtain

$$R_{c/t}\Big|_{\tilde{\chi}_1^0=\tilde{H}^0,\; m_{\tilde{u}_1}\gg m_{\tilde{\chi}_1^0}} \;=\; \frac{m_c^2}{m_t^2}\frac{1-x_{\tilde{t}}}{x_{\tilde{t}}}\,. \tag{3.11}$$

As a second example, we assume a pure bino-like neutralino and obtain

$$R_{c/t}\Big|_{\tilde{\chi}_1^0=\tilde{B}^0,\; m_{\tilde{u}_1}\gg m_{\tilde{\chi}_1^0}} \;=\; \frac{1-x_{\tilde{t}}+\kappa_c\big(\mathcal{R}_{\tilde{u}}\big)^2_{15}}{x_{\tilde{t}}+\kappa_c\big(\mathcal{R}_{\tilde{u}}\big)^2_{16}} \;\longrightarrow\; \frac{1-x_{\tilde{t}}}{x_{\tilde{t}}}\,, \tag{3.12}$$

where $\kappa_q = e_q/\big(e_q - T_q^3\big)^2 - 1 = 15$ for $q = c, t$, and the last expression holds for a pure "left-handed" or a pure "right-handed" squark. Finally, for a pure wino-like neutralino, the ratio becomes

$$R_{c/t}\Big|_{\tilde{\chi}_1^0=\tilde{H}^0} \;=\; \frac{B_c}{B_t}\frac{\lambda_c^{1/2}}{\lambda_t^{1/2}}\frac{\big(\mathcal{R}_{\tilde{u}}\big)^2_{12}}{\big(\mathcal{R}_{\tilde{u}}\big)^2_{13}} \;\longrightarrow\; \frac{B_c}{B_t}\frac{\lambda_c^{1/2}}{\lambda_t^{1/2}}\frac{1-x_{\tilde{t}}}{x_{\tilde{t}}}\,, \tag{3.13}$$

where $\lambda_q = \lambda\big(m_{\tilde{u}_1}^2, m_{\tilde{\chi}_1^0}^2, m_q^2\big)$ denotes the usual Källén function associated to the squark decay, and $B_q = m_{\tilde{u}_1}^2 - m_{\tilde{\chi}_1^0}^2 - m_q^2$ for $q = c, t$. Here, the last expression holds for a pure "left-handed" squark. As can be seen, these simplifying limits contain the same factor $\big(1-x_{\tilde{t}}\big)/x_{\tilde{t}}$.

In order to visualize these results, we randomly scan over the parameters governing the lightest squark as well as the neutralino/chargino sector. More precisely, we vary the physical squark mass $m_{\tilde{u}_1}$ and the parameters $x_{\tilde{t}}$, $\theta_{\tilde{t}}$, and $\theta_{\tilde{c}}$ defining its flavour decomposition. In the gaugino sector, we scan over bino, wino, and Higgsino mass parameters M_1, M_2, and μ. For

Variable	Range
$m_{\tilde{u}_1}$	$[700, 2000]$
$x_{\tilde{t}}$	$[0, 1]$
$\cos\theta_{\tilde{t}}$	$[0, 1]$
$\cos\theta_{\tilde{c}}$	$[0, 1]$

Variable	Range
M_1	$[600, 2000]$
M_2	$[600, 2000]$
μ	$[600, 2000]$

TABLE 3.1: Scanned ranges of the parameters associated to the squark (left) and gaugino sector (right). All masses are given in GeV.

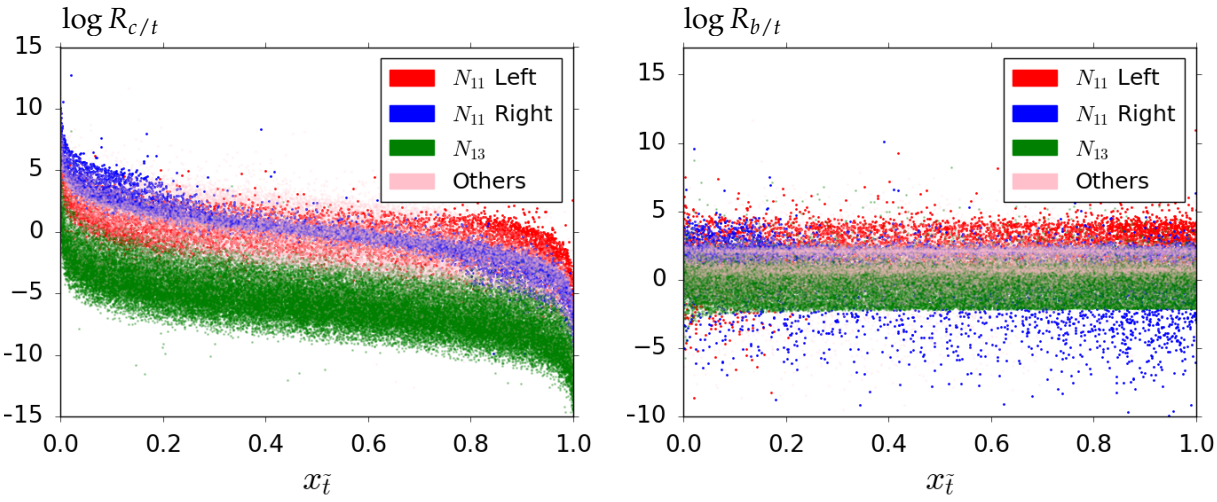

FIGURE 3.14: Distributions of the ratios $R_{c/t}$ (left) and $R_{b/t}$ (right) of the decay modes defined in Eq. (3.10) in dependence of the stop composition $x_{\tilde{t}}$ of the decaying squark. The colour code refers to different combinations of neutralino compositions and squark "chiralities".

this simple study, the physical masses are obtained by diagonalizing the mass matrices at the tree-level. All parameters are scanned over according to the ranges given in Table 3.1. As the expressions in Eqs. (3.11) – (3.13) do not exhibit a dependence on $\tan\beta$, we conclude that this parameter only has a mild impact on the observables of our interest and set $\tan\beta = 10$ throughout the following analyses.

For each parameter point, the ratios $R_{c/t}$ and $R_{b/t}$ are computed using the full analytical expressions for the involved decay widths given in Ref. [72]. The results are shown in Fig. 3.14, where we indicate as a colour code the dominant component of the involved neutralino as well as the nature of the decaying squark, relating thus the regions of the plot to the expressions found in Eqs. (3.11) – (3.13). As expected from these expressions, distinct regions are observed in the distribution of $R_{c/t}$. The same behaviour is observed for $R_{b/t}$. The two rations depend strongly on the neutralino decomposition and the "chirality" of the decaying squark. The width of each band is due to the fact that the majority of the randomly chosen parameter points feature mixed gauginos and squarks rather than falling into the limit cases discussed above. Nevertheless, the presence of the observed rather distinct regions is an important feature which will turn out to be crucial in the identification of the squark flavour decomposition from the observables given in Eq. (3.10).

Before discussing the actual methods aiming at reconstructing the value of the top-content $x_{\tilde{t}}$, let us mention that the studies presented here are a first step in this direction. It is to be noted that there is certainly room for improvement, especially on the treatment of the involved uncertainties, and a certain amount of follow-up work will be required to achieve the actual goal.

A likelihood fit in a simplified model

As indicated in the introduction of this Chapter, the first method attempting to reconstruct the flavour content of an observed squark is based on a likelihood fit. The goal is to infer the stop content $x_{\tilde{t}}$ of the squark. The starting point of the present method is the construction of a likelihood estimator. For a given set of data

$$D \;=\; \left\{ m_{\tilde{u}_1}\,, m_{\tilde{\chi}_1^0}\,, m_{\tilde{\chi}_1^\pm}\,, R_{c/t}\,, R_{b/t} \right\} \tag{3.14}$$

supposed to be obtained at the Large Hadron Collider, a likelihood value is associated to each point of an ensemble of randomly generated parameter points. Assuming a Gaussian distribution, this likelihood takes the form

$$\ln \mathcal{L}(\theta) \;=\; -\sum_i \left(\frac{\theta_i - D_i}{\sigma_i} \right)^2 , \tag{3.15}$$

where θ is the set of parameters associated to the random parameter point under consideration. Moreover, σ_i denotes the error associated to the observable D_i. For the present example, the sum runs over the five observed quantities given in Eq. (3.14).

The next step consists of dividing the interval $x_{\tilde{t}} \in [0;1]$ into N bins of equal size. For each bin $j = 1, \ldots, N$, we compute an average likelihood $\hat{\mathcal{L}}(x_{\tilde{t}})$ of all random parameter points having their value $x_{\tilde{t}}$ inside the given bin. From the obtained values of $\hat{\mathcal{L}}(x_{\tilde{t}})$, a Gaussian distribution can be fitted in order to find the maximum of likelihood corresponding to the inferred value of the stop content $x_{\tilde{t}}$. The associated uncertainty $\sigma(x_{\tilde{t}})$ is then based on the standard deviation value associated to the Gaussian fit.

Several subtleties appear and have to be addressed when performing this analysis. The first one is of technical nature: in order to fill the full interval $x_{\tilde{t}} \in [0;1]$ in a consistent way, a large number of random points is required. The exact number depends on the chosen bin size. The second, and more tricky, part resides in the uncertainty σ_i entering the likelihood calculation in Eq. (3.15). Usually this standard deviation corresponds to the uncertainty associated to the measurement of the quantity D_i. In the present case, however, since different parameter configurations θ_i can lead to the same observation, there is an additional feature, which shall be discussed later on.

In order to illustrate the proposed method using a simple example, let us first consider the case where the parameters related to the neutralino and chargino mixing are fixed as

$$N_{1i} \;=\; 0.5 \qquad U_{11} \;=\; V_{12} \;=\; 1 \qquad U_{12} \;=\; V_{11} \;=\; 0\,, \tag{3.16}$$

i.e. we consider the case of a maximally mixed neutralino. For this example, a random scan over the five parameters of Eq. (3.14) has been performed leading to an ensemble of $5 \cdot 10^8$ parameter points. Moreover, we assign a common value of $\sigma_i = 0.25 D_i$ to the uncertainties entering the likelihood calculation.

In order to illustrate the results of this method, we start by discussing the first four test parameter points P_i ($i = 1, \ldots, 4$) listed in the first part of Table 3.2. As can be seen in the Table, the test parameter sets are chosen to represent different configurations concerning the involved masses and the squark flavour content. The Gaussian fits based on the average likelihood $\hat{\mathcal{L}}_j(x_{\tilde{t}})$ for the four points are shown in Figure 3.15, and the resulting inferred stop components $x_{\tilde{t}}$ are indicated in Table 3.2. As can be seen, the method basically manages to recover the actual stop component of the lightest squark within the resulting uncertainties from the Gaussian fit.

If almost all points in a given bin lead to a rather low value of the likelihood $\mathcal{L}(\theta)$ and if the uncertainties σ_i are rather low, a single point featuring a larger likelihood may become of

Data set	$m_{\tilde{u}_1}$	$m_{\tilde{\chi}_1^\pm}$	$m_{\tilde{\chi}_1^0}$	$x_{\tilde{t}}$	σ_i / D_i	inferred $x_{\tilde{t}} \pm \sigma(x_{\tilde{t}})$
P_1	1015.73	699.60	604.39	0.66	0.25	0.57 ± 0.16
P_2	1798.29	303.02	267.66	0.04	0.25	0.04 ± 0.03
P_3	1488.78	321.53	244.21	0.08	0.25	0.15 ± 0.08
P_4	1422.50	1001.11	637.85	0.83	0.25	0.76 ± 0.12
S	1531.97	643.99	289.09	0.54	0.35	0.49 ± 0.18
					0.25	0.47 ± 0.15
					0.15	0.45 ± 0.14
					0.05	–
P_5	1369.07	281.13	276.32	0.04	0.35	0.03 ± 0.03
P_6	1770.52	717.95	511.39	0.65	0.35	0.00 ± 0.90

TABLE 3.2: Parameters of the test data sets together with the assumed relative error σ_i / D_i and the stop component obtained from the likelihood fits illustrated in Figs. 3.15 – 3.17. All masses are given in GeV. Details on the results are given in the text.

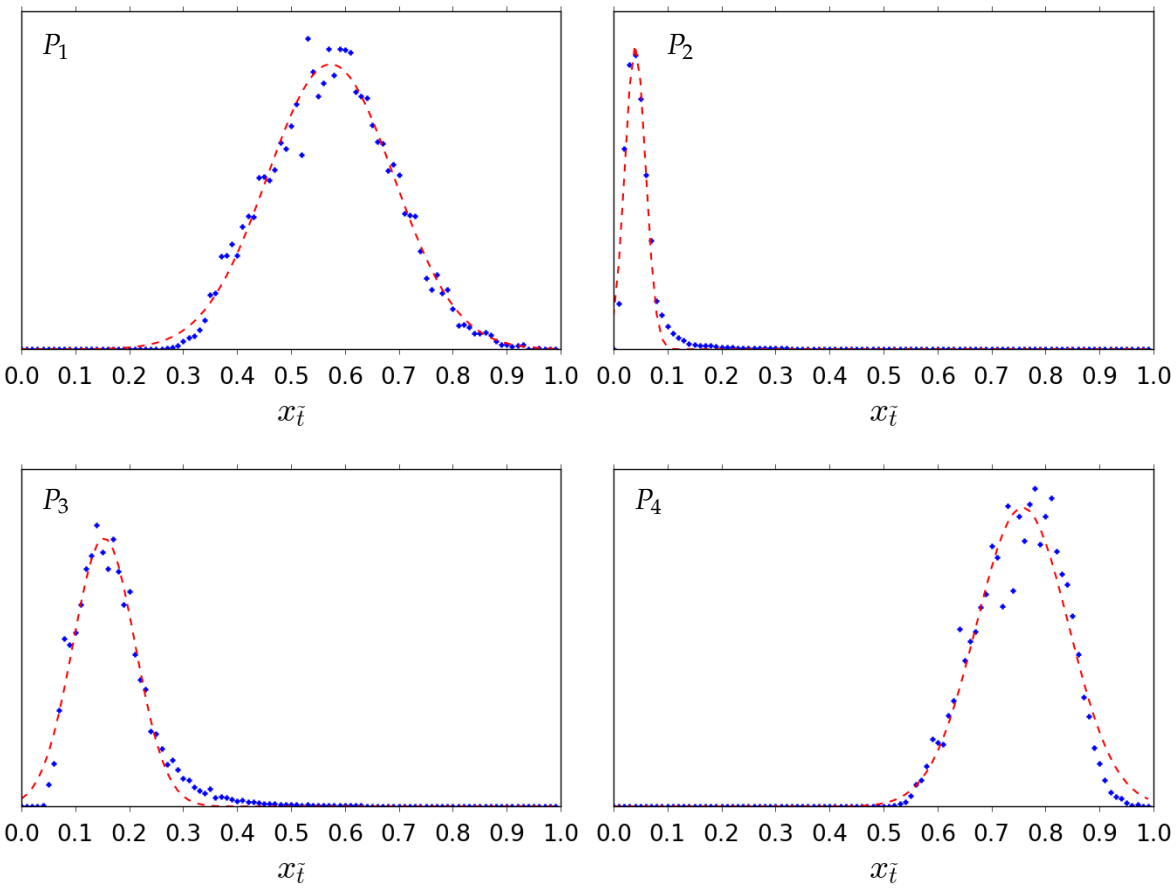

FIGURE 3.15: Likelihood fit four test data sets featuring a fixed gaugino composition as in Eq. (3.16). The resulting inferred values of the stop component are listed in Table 3.2. The distributions are shown on a linear scale.

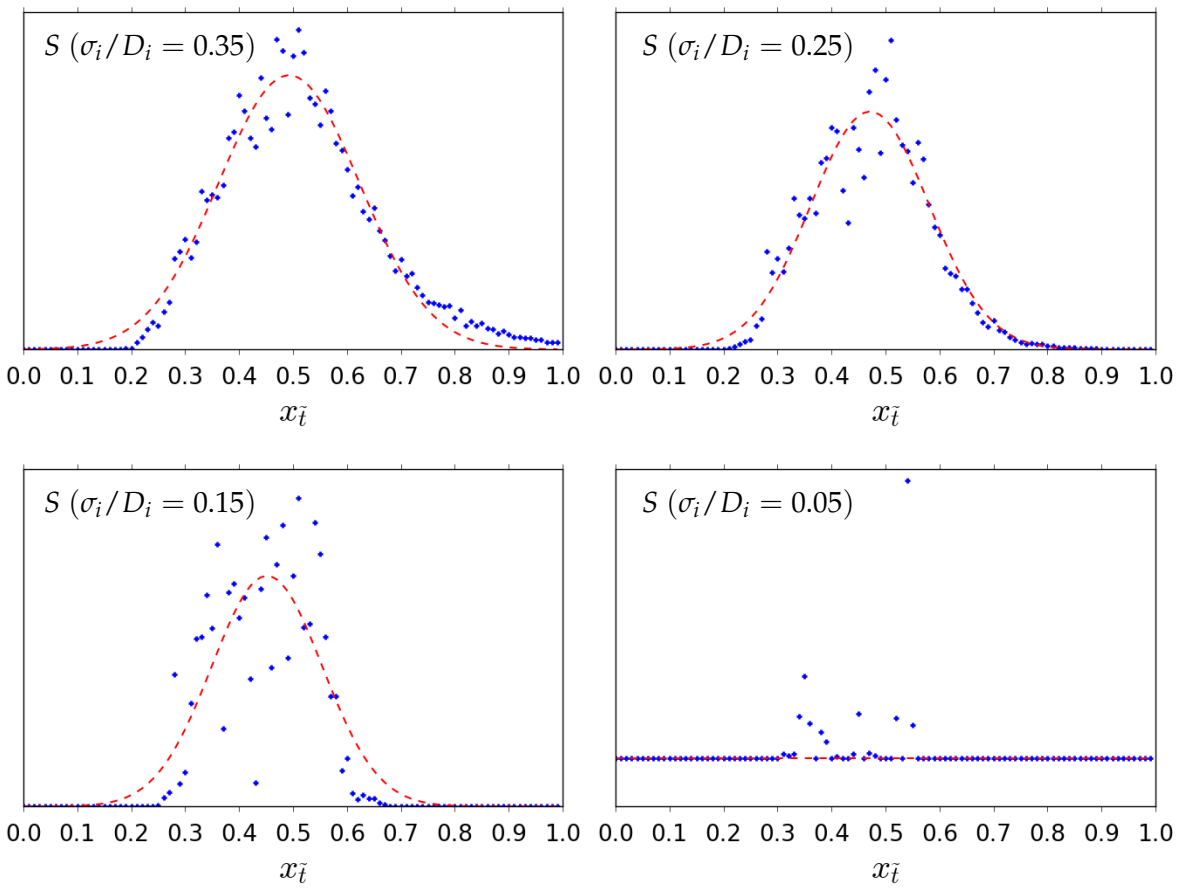

FIGURE 3.16: Same as Fig. 3.15 for a single test parameter point but varying uncertainty σ_i/D_i.

great importance. This in turn can lead to a bad estimation of the stop component $x_{\tilde{t}}$. The conclusion of this is that the uncertainties σ_i entering the likelihood calculation in Eq. (3.15) have in fact two components: the uncertainty of the observable itself, and in addition an uncertainty coming from the potential degeneracy of the observables with respect to the stop component $x_{\tilde{t}}$. Such a gegeneracy may lead to a variation of the density of points between different regions of parameter space.

For completeness, we illustrate the impact of the uncertainty σ_i associated to the observables D_i. The four graphes in Figure 3.16 show the likelihood fits for a single test parameter point for four different values of σ_i/D_i as indicated in the middle part of Table 3.2. For large values of $\sigma_i/D_i = 0.35$, the fit converges well and the resulting value of $x_{\tilde{t}}$ is close to the assumed one. However, the Gaussian width is rather large leading to a sizeable uncertainty $\sigma(x_{\tilde{t}})$. Going to smaller values of σ_i/D_i leads to a less accurate fit and drives the inferred stop composition away from the assumed one. The associated Gaussian width is smaller, and thus the inferred uncertainty is less important. The explanation of this feature is that the actual uncertainty on the inferred stop composition has in reality two components, the first coming from the width of the fitted Gaussian function, the second coming from the overall quality of the fit. Finally, pushing σ_i/D_i to even lower values makes the fit break down, as can be seen in the last panel of Fig. 3.16. This is the actual tricky point of the present analysis. The choice of σ_i/D_i must therefore be made with precaution because it has more impact than the Gaussian width and it also depends on the density of points in a certain area of the scan. Using this method to infer the actual stop composition will need specific care and deeper understanding of the uncertainties, which is beyond the first step presented in this work.

As a final step, we relax the assumption on the gaugino decompositions given in Eq. (3.16),

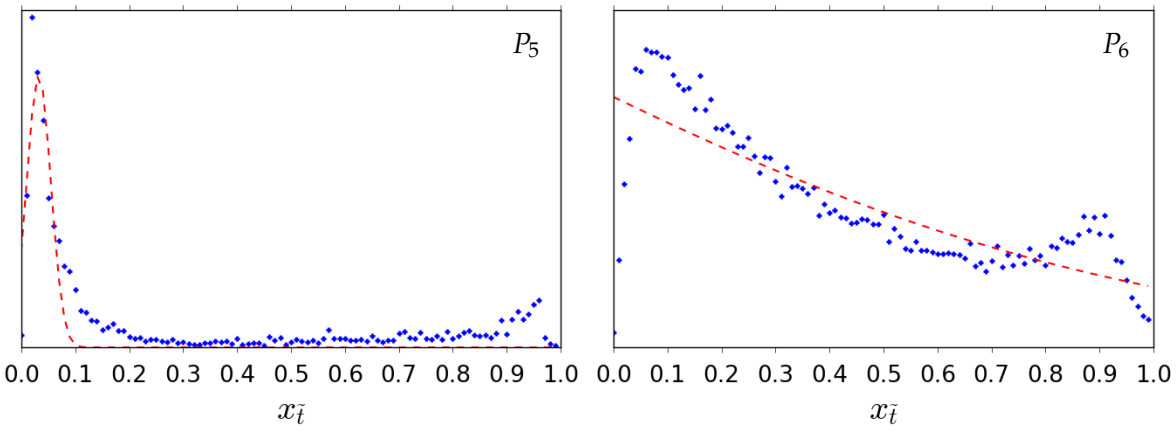

FIGURE 3.17: Same as Fig. 3.15 for two test parameter points obtained by scanning in addition over the parameters related to the gaugino sector.

and include the gaugino mixing parameters in the random scan. Again, we generate an ensemble of $5 \cdot 10^8$ parameter points with $\sigma_i = 0.35 D_i$, and apply our reconstruction method to two data sets P_5 and P_6. The results are shown in Fig. 3.17 and summarized in the lower part of Table 3.2. Even if the true stop components lie within the infered intervals, the uncertainties are much larger in this case, such that the results become rather meaningless in certain cases. In addition, from Fig. 3.17 we can see that the likelihood is no longer Gaussian. This is due to the fact that here different regions of the parameters present a concentration of points able to explain the data.

A multivariate analysis in a simplified model

In order to go beyond the likelihood inference presented in the previous Section, especially in more realistic setup as discussed, e.g., in Ref. [88], we now employ a multivariate analysis classifier. In the present Section, we will present results obtained within the simplified setup already used in the previous Section from a multi-layer perceptron provided through the `TMVA` package [163, 164] of the `ROOT` framework [165]. The discussion of the Minimal Supersymmetric Standard Model with general squark mixing of Ref. [88] will follow in the next Section.

In the context of a multivariate analysis, the goal of the analysis is slightly different with respect to the previous Section. While the likelihood inference aims at estimating the actual stop component of the observed squark, a multivariate analysis is designed to effiently classify different configurations. In order to provide a simple illustration, we define two categories based on the stop composition $x_{\tilde{t}}$, which remains the key quantity of our interest. We will divide the parameter space into "top-flavoured" squarks and "charm-flavoured" squarks according to

$$x_{\tilde{t}} < 0.5 \quad \Longleftrightarrow \quad \text{“charm} - \text{flavoured”}\,, \tag{3.17}$$

$$x_{\tilde{t}} > 0.5 \quad \Longleftrightarrow \quad \text{“top} - \text{flavoured”}\,. \tag{3.18}$$

Let us note that these categories are for the moment rather arbitrary and aim at the illustration of the method rather than representing specific physical regions. In particular, additional categories can be defined in order to refine the analysis. Based on the two categories, the MLP can be trained on the parameter points obtained from the random scan, and subsequently tested on a subset of points, the test sample, in order to compute the efficiency and the misidentification rate of the classifier. The analysis presented here is based on a training sample of 10^6 points, which have been obtained by uniformly scanning as indicated in Table 3.1.

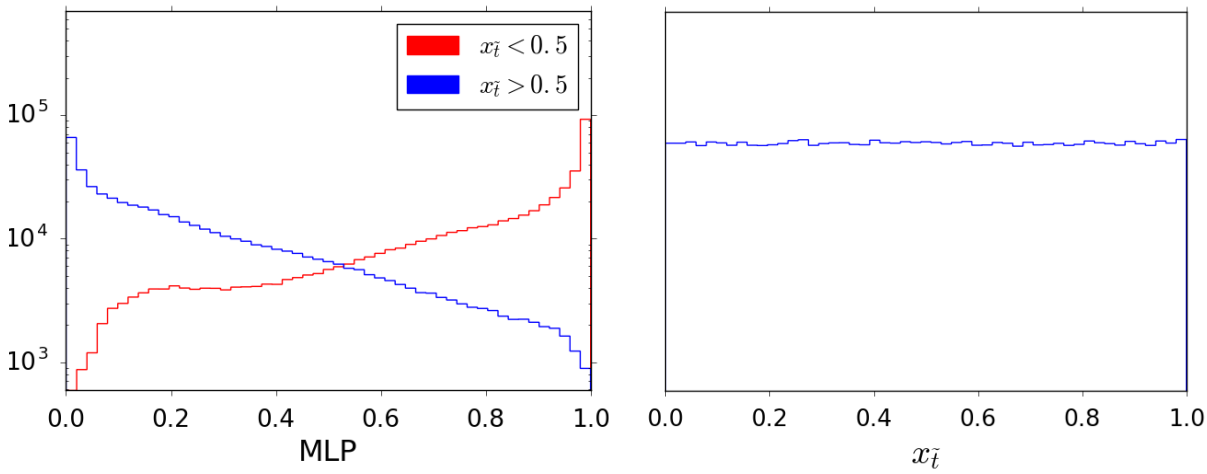

FIGURE 3.18: MLP response (left panel) on the simplified scan based on a uniform prior (right panel, linear scale) of the stop component $x_{\tilde{t}}$. The colour code corresponds to the seperation of "top-like" (blue) and "charm-like" (red) squarks.

The classifier basically combines the set of obervables given in Eq. (3.14), i.e. $R_{c/t}$, $R_{b/t}$, $m_{\tilde{u}_1}$, $m_{\tilde{\chi}_1^0}$, and $m_{\tilde{\chi}_1^+}$, into one single variable called the MLP response. The algorithm will associate an MLP value to each parameter point of the scan, depending on the set of observables that maximize the separation between the two categories. Several points need to be kept in mind when performing this type of analysis. A key point is the so-called "overtraining", meaning that training the algorithm on a too small dataset may enforce the identification of unphysical regions, i.e. statistical fluctuations, as physical ones. We have performed an overtraining check by comparing the classification performance on the training sample and on the test sample. The behavior of the algorithm being the same on the two samples, we conclude that there are no statistical fluctuations having an impact on the classification.

The rather simple situation of having only two categories will also serve to study the influence of the underlying prior distribution, in particular of the stop component $x_{\tilde{t}}$. We start from the same setup as previously, where the random parameter scan has been performed such that the stop component $x_{\tilde{t}}$ exhibits a flat distribution. For this case, we show the obtained MLP response for the two categories in Fig. 3.18, together with the prior distribution of the stop component.

As can be seen, the classifier manages to seperate the two categories with a rather good efficiency. For a given misidentification rate, the associated efficiency, i.e. the number of points of a chosen class surviving the misidentification cut, of the classifier can be computed. In the present case, for a misidentification rate of 10%, we obtain an efficiency of 54% for the "top-like" squark region and of 64% for the "charm-like" case. In other words, we can tag respectively approximately 54% and 64% of the points at 90% confidence level.

As a second example, we employ the classifier to the case of a non-uniform prior distribution of the stop-content $x_{\tilde{t}}$. Inspired by the results of Ref. [88], we choose a prior distribution peaking at its "MFV-like" extremities $x_{\tilde{t}} \approx 0$ and $x_{\tilde{t}} \approx 1$. Apart from the prior distribution (and thus the squark rotation matrix elements), the sample has the same characteristics as the previous one. The prior distribution and the resulting MLP response are shown in Fig. 3.19. While it is approximately symmetric in the case of a flat prior, the MLP response associated to the two categories is clearly non-symmetric in the present case. This can be traced to the fact that the observables used to classify are non-symmetric with respect to "top-flavoured" and "charm-flavoured" squarks.

In this example, for the misidentification rate of 10%, we obtain an efficiency of 64% (60%)

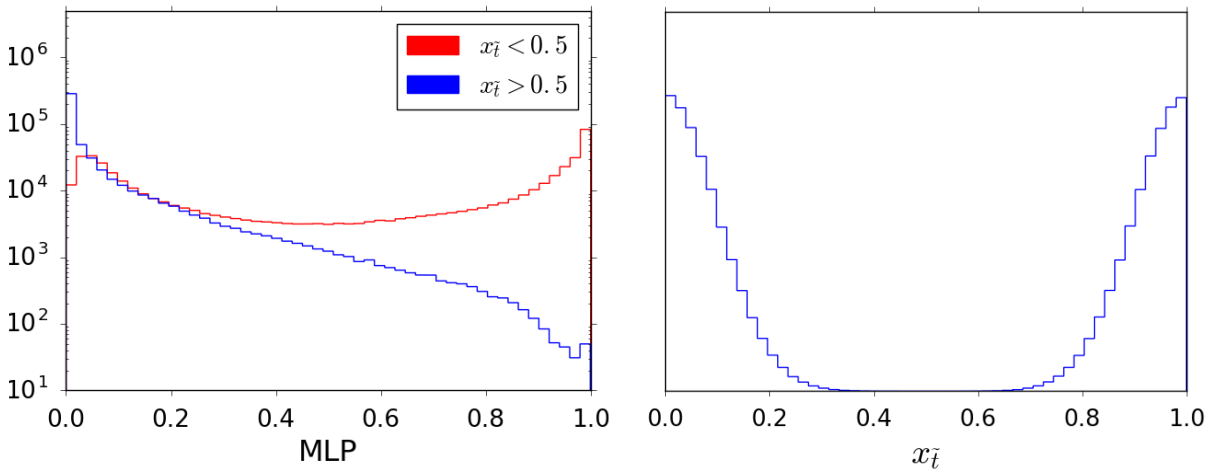

FIGURE 3.19: Same as Fig. 3.18 for an example of a non-uniform prior of the stop component $x_{\tilde{t}}$.

for the "top-flavoured" ("charm-flavoured") category. It appears that the efficiency depends on the prior distribution. More precisely, the classifier becomes more efficient in identifying the "top-flavoured" category, but slighly less performant concerning the "charm-flavoured" category.

The increasing classification power coming from the prior distribution can intuitively be understood as the two categories are now more different. The border between the two cases, i.e. $x_{\tilde{t}} \sim 0.5$, where it is phenomenologically difficult to assign a given point to a single category, are less populated in the second case with non-uniform prior. It is therefore easier to maximize the separation. After this first analysis within a simplified setup, we now aim at applying the MLP method to a more complete model.

3.4 Applications to the general MSSM

As announced in the previous Section, we finally apply the multivariate analysis (MVA) classifier to the Minimal Supersymmetric Standard Model (MSSM) with non-minimal flavour mixing between charm- and top-flavoured squarks. In order to work with a rather "realistic" setup, we choose to use the parameter points obtained in Ref. [88] as basis of our study. These parameter points defined at the TeV scale have been shown to fulfill all relevant constraints coming from flavour and precision measurements, in particular the Higgs-boson mass, the decays $B \to X_s\gamma$ and $B \to X_s\mu\mu$, and the meson oscillation parameter ΔM_{B_s}, to name the most important ones. For all details on the applied constraints and the related Markov Chain Monte Carlo study of the MSSM with non-minimal flavour violation in the squark sector, the reader is referred to Ref. [88].

Following the preliminary study of the simplified setup in Sec. 3.3, it is interesting to examine the prior distribution of the quantity that we want to address, i.e. the stop component $x_{\tilde{t}}$ of the lightest up-type squark. As can be seen from its representation in Fig. 3.20, the distribution strongly peaks at the "MFV-like" ends. Moreover, flavour and precision data tend to favour a high charm content with respect to top content in the lightest squark. Note that this situation is similar to the non-uniform prior tested in Sec. 3.3, which turned out to yield a higher efficiency than the simpler uniform prior. We now perform the same MLP classification using a training sample containing about $6 \cdot 10^5$ points obtained from the MCMC analysis of Ref. [88] [1].

[1] For the present study, we have extended the sample resulting from the analysis presented in Ref. [88] using exactly the same computational setup.

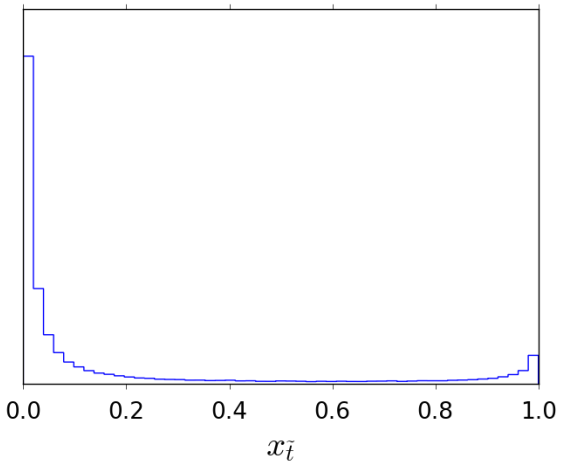

FIGURE 3.20: Prior distribution (linear scale) of the stop composition $x_{\tilde{t}}$ from the MCMC analysis of Ref. [88].

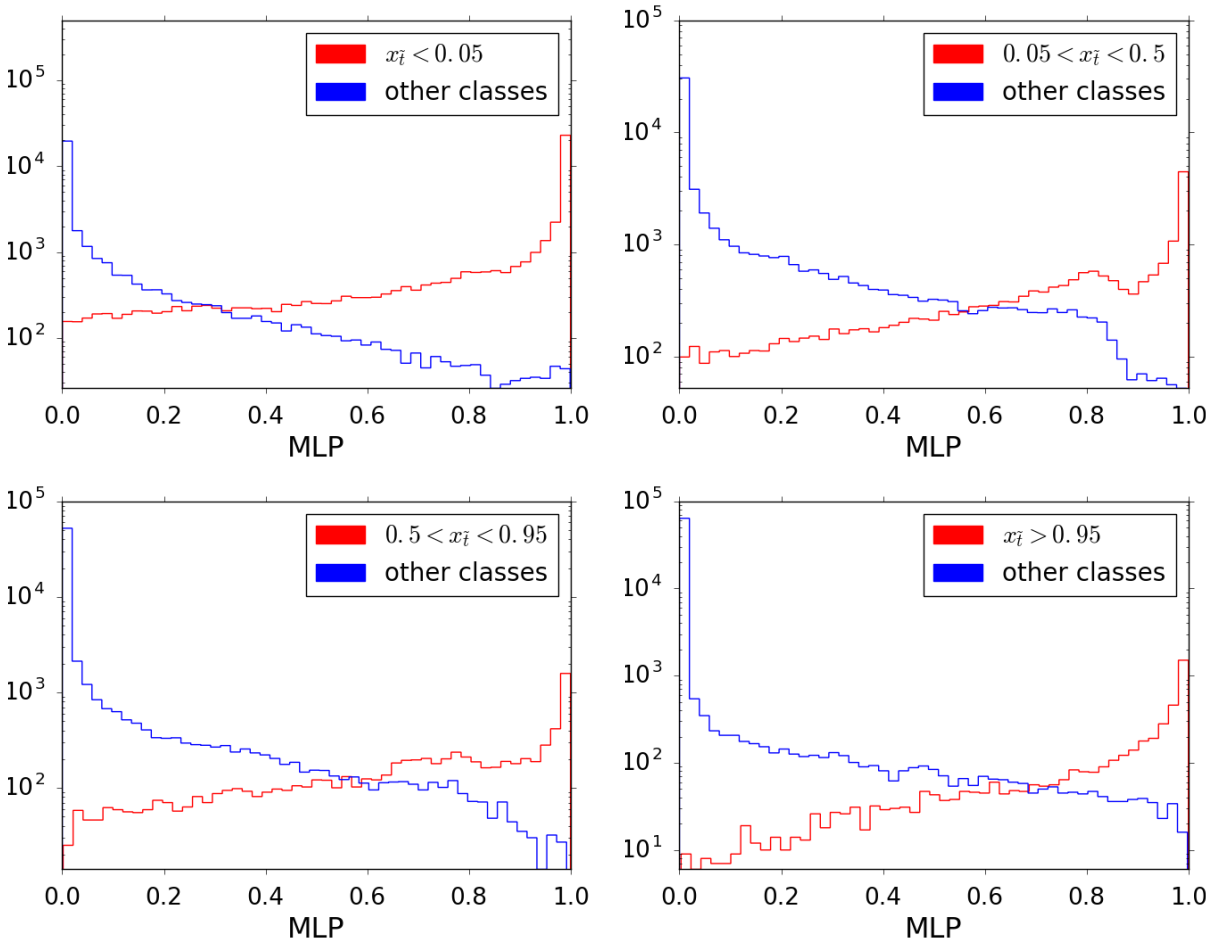

FIGURE 3.21: MLP response on the NMFV-MSSM of Ref. [88] for the seperation the "charm MFV" (upper left), "charm NMFV" (upper right), "top NMFV" (lower left), and "top MFV" (lower right) categories (red) from the remaining parameter points (blue).

Categories		Efficiency
"charm" MFV	$0.00 \leq x_{\tilde{t}} < 0.05$	95%
"charm" NMFV	$0.05 < x_{\tilde{t}} < 0.50$	51%
"top" NMFV	$0.50 < x_{\tilde{t}} < 0.95$	41%
"top" MFV	$0.95 < x_{\tilde{t}} \leq 1.00$	69%

TABLE 3.3: Efficiencies of the classification method for the four categories of our interest assuming a misidentification rate of 10%.

Starting from the prior distribution shown in Fig. 3.20, we divide the ensemble of points into four categories defined as follows:

$$\begin{aligned} 0.00 \leq x_{\tilde{t}} < 0.05 &\iff \text{"charm MFV"} \\ 0.05 < x_{\tilde{t}} < 0.50 &\iff \text{"charm NMFV"} \\ 0.50 < x_{\tilde{t}} > 0.95 &\iff \text{"top NMFV"} \\ 0.95 < x_{\tilde{t}} \leq 1.00 &\iff \text{"top MFV"} \end{aligned} \tag{3.19}$$

Note that, although the given definition of the above categories is again somewhat arbitrary, the exact value of the cuts between MFV and NMFV does not have a major impact on the methods presented in the following. It might, however, affect the efficiency of the proposed analysis, and the exact definition of the categories may in practice depend on the problem under consideration.

The MVA classifier is used to seperate each of the four categories from its complement, i.e. the ensemble comprising the three other classes. In Fig. 3.21, we show the MLP responses obtained for the four cases. As expected from the overpopulated prior region, the "charm MFV" category is rather well identified. However, the identification is less efficient for the two NMFV categories, which are underpopulated in the prior distribution. For the sake of a numerical comparison between the categories, and also to the cases presented in Sec. 3.3, we summarize the obtained efficiencies of the classifier in Table 3.3.

Overall, the performance of the classifier is better than for the simplified situations presented in Sec. 3.3. This can be traced to the underlying prior distribution of the stop content $x_{\tilde{t}}$ (see Fig. 3.20). The categories which are most difficult to identify, i.e. the two NMFV categories, are less populated in this particular model. The algorithm is therefore less performant in distinguishing these categories. The small bump observed around MLP $\sim 0.7 \ldots 0.8$ in both NMFV categories is an artefact of the employed multi-class MLP due to the presence of phenomenologically different regions.

We have also tested the likelihood inference method discussed in Sec. 3.3 on the present case of the NMFV-MSSM of Ref. [88]. However, for this method it turns out that inferring in a region of rather low density is quite difficult (contrary to the case of a uniform prior applied in Sec. 3.3). In addition, the strongly peaked prior distribution of the stop component $x_{\tilde{t}}$ leads to a certain bias, such that the obtained results are not reliable any more. We therefore do not discuss this method further for the given model.

As a final comment, I would like to emphasize that the two presented methods are not addressing exactly the same question. While the multi-variate analysis does not return an actual value for the top- flavour content of the squark, the likelihood inference can provide a reasonable estimation. However, the likelihood inference needs additional information, especially on the gaugino sector, and cannot handle very extreme prior distributions. These inconvenients can in turn be avoided by the use of the multivariate analysis, which already allows to gain valuable information on the flavour structure.

As this is a first attempt of the reconstruction of the squark flavour structure, the presented analysis relies on rather simple observables. Designing improved analyses inspired from this work should lead to a considerable improvement of the performances. One might consider additional observables related to the same parameters, such as, e.g., such as the top polarization from the squark decay or event rates stemming from gluino production and decay. From the machine-learning point of view, many algorithms exist for parameter-fitting problems and with a specific analysis it may be possible to access the actual value of the top-flavour content in a generic gaugino sector. Finally, it is to be noted that for both methods, the uncertainties will have to be analyzed in greater detail in order to maximally benefit from such a study.

Chapter 4

A window towards Grand Unification

A rather fascinating feature of the Standard Model is that its matter fields fit into a complete representation of the gauge group $SU(5)$ [166]. This feature can be interpreted as a hint that the Standard Model arises as the low-energy limit of a Grand Unified Theory (GUT) containing $SU(5)$ as a subgroup at some higher scale [167, 168, 169, 170]. Moreover, Supersymmetry is a natural companion of $SU(5)$-like unification as already the simplest supersymmetric models lead to gauge-coupling unification with a good precision.

In the present Chapter, I will discuss two aspects of the Minimal Supersymmetric Standard Model (MSSM) with general flavour mixing and $SU(5)$ unification conditions at the GUT scale. After discussing general features of this setup in Sec. 4.1, in Section 4.2, I will present a concrete implementation of such a model, where Non-Minimally Flavour Violating terms are generated thanks to the presence of a flavour symmetry. This part is based on Ref. [171].

4.1 Fermion and sfermion sectors with $SU(5)$-like unification

Within the $SU(5)$-unification framework, the fields $\{Q_i, U_i, E_i\}$ and $\{L_i, D_i\}$ can respectively be embedded intro three copies of the **10** and $\bar{\mathbf{5}}$ representations of $SU(5)$ according to

$$F = \bar{\mathbf{5}} = \begin{pmatrix} d_r^c \\ d_b^c \\ d_g^c \\ e^- \\ -\nu_e \end{pmatrix}_L , \qquad T = \mathbf{10} = \begin{pmatrix} 0 & u_g^c & -u_b^c & u_r & d_r \\ . & 0 & u_r^c & u_b & d_b \\ . & . & 0 & u_g & d_g \\ . & . & . & 0 & e^c \\ . & . & . & . & 0 \end{pmatrix}_L , \tag{4.1}$$

where r, g, b denote the quark colours, and c denotes CP-conjugated fermions. The Higgs doublets H_u and H_d, which break the electroweak symmetry, may arise from $SU(5)$ multiplets $H_{\mathbf{5}}$ and $H_{\bar{\mathbf{5}}}$, provided the colour triplet components are heavy. The $SU(5)$ gauge group may be broken by an additional Higgs multiplet in the **24** representation developping a vacuum expectation value according to

$$SU(5) \longrightarrow SU(3)_C \times SU(2)_L \times U(1)_Y , \tag{4.2}$$

corresponding to the Standard Model gauge group.

Besides gauge-coupling unification at the GUT scale, the above matter field unification implies relations within the Yukawa sector,

$$Y_d = Y_e^t \qquad Y_u = Y_u^t . \tag{4.3}$$

This means that the leptonic Yukawa matrix is given in terms of the down-quark Yukawa matrix, while the up-quark Yukawa matrix is symmetric at the unification scale.

In addition, the $SU(5)$ symmetry provides relationships between the soft terms belonging to the supermultiplets within a given representation. For the MSSM under consideration here, in terms of $SU(5)$ fields, the soft-breaking Lagrangian associated to the sector of sfermions reads

$$-\mathcal{L}_{\text{soft}}^{\text{SU(5)MSSM}} = M_F^2 \widetilde{F}^\dagger \widetilde{F} + M_T^2 \widetilde{T}^\dagger \widetilde{T} + \left(A_{TT} \widetilde{T}^* H_u \widetilde{T} + A_{FT} \widetilde{F}^* H_d \widetilde{T} + \text{h.c.} \right) \tag{4.4}$$

where $\tilde{F}$ and $\tilde{T}$ denote the superpartner fields of F and T given in Eq. (4.1). Comparing this with the general MSSM Lagrangian given in Eq. (1.29) leads to the relations

$$\begin{aligned} M_{\tilde{Q}}^2 &= M_{\tilde{U}}^2 = M_{\tilde{E}}^2 \equiv M_T^2 , & M_{\tilde{D}}^2 &= M_{\tilde{L}}^2 \equiv M_F^2 , \\ A_d &= (A_e)^T \equiv A_{FT} , & A_u &\equiv A_{TT} , \end{aligned} \tag{4.5}$$

that hold at the GUT scale. Note that renormalization group evolution towards lower scales will spoil these relations. However, although the numerical values of the elements of the soft mass and trilinear matrices may be very different at, e.g., the TeV scale, the above relations provide an interesting link between different sectors, in particular between the squark and slepton sectors. Such "footprints" of the $SU(5)$-like unification are interesting since the same soft parameters may be constrained by experimental data from the two sectors. The examples discussed in the following Section are based on such relations.

Introducing Non-Minimal Flavour Violating (NMFV) off-diagonal elements can then be parametrized relative to the diagonal ones in the same way as presented in Eqs. (1.39). Taking into account the above $SU(5)$ boundary conditions leads to the relationships

$$\begin{aligned} \delta_{LL}^q &= \delta_{RR}^u = \delta_{RR}^e \equiv \delta^T , & \delta_{RR}^d &= \delta_{LL}^e \equiv \delta^F , \\ \delta_{RL}^d &= (\delta_{RL}^e)^T \equiv \delta^{FT} , & \delta_{RL}^u &\equiv \delta^{TT} , \end{aligned} \tag{4.6}$$

where the superscripts T, F, TT, and TF refer to the respective sectors at the high scale according to Eq. (4.5). Note that δ^T, δ^F and δ^{TT} are necessarily symmetric whereas δ^{FT} is not, leading to a total of 15 independent NMFV parameters at the GUT scale. The relations given in Eqs. (4.5) and (4.6) are exact at the unification scale, but will be spoiled by the renormalization group running when evolving them towards lower scales.

4.2 Flavour Violation in $A_4 \times SU(5)$ Supersymmetry

In addition to the $SU(5)$ GUT conditions, an A_4 (alternating group of order 4) flavour symmetry is imposed on the Minimal Supersymmetric Standard Model (MSSM) under consideration. To this end, the three families of $F = \bar{\mathbf{5}} = \left(d^c, L\right)$ are unified into the triplet of A_4 leading to a unified soft-mass parameter M_F for the three generations. The three families of $T_i = \mathbf{10}_i = \left(Q, u^c, e^c\right)_i$ are singlets of A_4, meaning that the three generations have independent soft mass parameters $(M_T)_{11}$, $(M_T)_{22}$, and $(M_T)_{33}$ [172, 173, 174, 175, 176].

Flavour violation is introduced in the soft parameters by breaking of the discrete symmetry. This primordial flavour violation manifests as off-diagonal elements within the matrices M_T^2, M_F^2, A_{FT}, and A_{TT} in the A_4 flavour basis, i.e. before rotation to the Super-CKM basis. Therefore, the relations given in Eqs. (4.6) hold before rotation to the Super-CKM basis. Note that the breaking of A_4 around the GUT scale enforces off-diagonal elements of these matrices to be smaller than diagonal entries, providing a theoretical motivation for small-but-non-zero flavour violation in such a class of models. Finally, the flavour mixing parameters which are present in the Lagrangian at the TeV scale stem from those introduced through the A_4 breaking

combined with renormalization group effects when evolving the parameters towards lower scales.

The aim of the present study [171] is to assess the impact of flavour-violating parameters introduced at the GUT scale on low-energy physics within the $A_4 \times SU(5)$ framework introduced above. More precisely, this model is tested against the dark matter relic density along with leptonic and hadronic flavour-changing observables and the mass of the CP-even Higgs boson. For a summary of observables and constraints see Table 2.1.

Setup and method

In order to focus on the impact of NMFV terms in the Lagrangian of our model, we start by choosing suitable reference scenarios respecting the MFV paradigm. From the previous work presented in Ref. [177] it is apparent that successfully imposing the dark matter relic density as well as the anomalous magnetic moment of the muon on the $A_4 \times SU(5)$ framework requires rather specific parameter configurations. More precisely, the corresponding parameter points feature a physical spectrum where the "right-handed" smuon is light and almost mass-degenerate with the lightest neutralino, which is bino-like. This allows to simultaneously satisfy the $(g-2)_\mu$ and relic density constraints [35, 48]. For our study, we choose two MFV reference scenarios, which are summarized in Table 4.1.

The first reference point of our choice corresponds to the scenario labelled "BP4" in Ref. [177]. For practical reasons, mainly due to including NMFV terms at the GUT scale, we do not make use of the same version of the spectrum generator `SPheno`. In consequence, effects from renormalization group running differ slightly, and we have adapted the input parameters of the original BP4 reference scenario to the ones given in Table 4.1. However, note that, although there is a small deviation for the TeV scale parameters as compared to scenario "BP4" of Ref. [177], the phenomenological aspects of our reference scenario at the TeV scale are unaffected. Let us recall that the rather low smuon mass parameter, $(M_T)_{22} = 200$ GeV, which leads to the physical mass $m_{\tilde{\mu}_R} = 102.1$ GeV, is required in order to satisfy simultaneously the $(g-2)_\mu$ and relic density constraints as discussed in Ref. [177].

While current limits on "right-handed" smuons still allow masses as low as about 100 GeV [178], this first scenario is going to be severely challenged by ongoing LHC searches. For this reason, we choose a second reference point which is inspired by the first one but features larger smuon and neutralino masses. This still allows satisfaction of the relic density constraint due to efficient co-annihilation and avoids LHC limits to be published in the near future. Note that, however, the higher smuon mass $m_{\tilde{\mu}_R} \sim 250$ GeV does not resolve the tension between the Standard Model and the experimental value of $(g-2)_\mu$. Let us emphasize that both reference scenarios capture the essential results of Ref. [177], namely almost mass-degenerate "right-handed" smuon and bino-like neutralino, while all other MSSM states are essentially decoupled.

We study the impact of flavour-violating terms by perturbing around the two chosen MFV reference points. Keeping the MFV parameters fixed at the values given in Table 4.1, we perform a uniform random scan over the flavour violating parameters according to the ranges indicated in Table 4.2.

For numerical evaluation, we make use of the spectrum generator `SPheno 4.0.3` [121, 122], where we have included the MSSM with general flavour mixing using the `Mathematica` package `SARAH 4.12.3` [179, 180, 181, 182, 183]. From the resulting code `SPhenoMSSM` we obtain through two-loop renormalization group equations for the soft-breaking parameters and the physical mass spectrum at the TeV scale, as well as numerical predictions for flavour observables listed in Table 2.1. The neutralino relic density $\Omega_{\tilde{\chi}_1^0} h^2$ is computed using the public package `micrOMEGAs 4.3.5` [184, 185, 186, 187, 188]. Again, we have used `SARAH` to obtain the `CalcHEP` model files necessary to accomodate NFMV effects in the calculation. The mass

	Parameter/Observable	Scenario 1	Scenario 2
MFV Parameters at GUT scale	M_F	5000	5000
	$(M_T)_{11}$	5000	5000
	$(M_T)_{22}$	200	233.2
	$(M_T)_{33}$	2995	2995
	$(A_{TT})_{33}$	-940	-940
	$(A_{FT})_{33}$	-1966	-1966
	M_1	250.0	600.0
	M_2	415.2	415.2
	M_3	2551.6	2551.6
	m_{H_u}	4242.6	4242.6
	m_{H_d}	4242.6	4242.6
	$\tan\beta$	30	30
	μ	-2163.1	-2246.8
Physical masses	m_h	126.7	127.3
	$m_{\widetilde{g}}$	5570.5	5625.7
	$m_{\widetilde{\mu}_L}$	4996.7	4997.5
	$m_{\widetilde{\mu}_R}$	102.1	254.4
	$m_{\widetilde{\chi}_1^0}$	94.6	250.4
	$m_{\widetilde{\chi}_2^0}$	323.6	322.0
	$m_{\widetilde{\chi}_3^0}$	2248.8	2331.1
	$m_{\widetilde{\chi}_4^0}$	2248.8	2331.2
	$m_{\widetilde{\chi}_1^\pm}$	323.8	322.2
	$m_{\widetilde{\chi}_2^\pm}$	2249.8	2332.2
	$\Omega_{\widetilde{\chi}_1^0}h^2$	0.116	0.120
	$\sigma_{\rm SI}^{\rm proton}/10^{-14}\,{\rm pb}$	2.987	1.055
	$\sigma_{\rm SI}^{\rm neutron}/10^{-14}\,{\rm pb}$	3.249	0.986

TABLE 4.1: GUT scale inputs together with selected physical masses and relevant TeV scale parameters for the two MFV reference scenarios. First and second generation trilinear couplings are set to zero. Further squark and slepton masses which are beyond the reach of current experiments are not shown. Unless otherwise illustrated, dimensionful quantities are given in GeV. DM direct detection cross-sections are given for both protons and neutrons.

Parameters	Scenario 1	Scenario 2
$(\delta^T)_{12}$	$[-2.00, 2.00] \times 10^{-2}$	$[-5.57, 5.15] \times 10^{-2}$
$(\delta^T)_{13}$	$[-8.01, 8.01] \times 10^{-2}$	$[-0.267, 0.301]$
$(\delta^T)_{23}$	0.0	$[-5.73, 5.73] \times 10^{-2}$
$(\delta^F)_{12}$	$[-8.00, 8.00] \times 10^{-3}$	$[-8.00, 8.00] \times 10^{-3}$
$(\delta^F)_{13}$	$[-1.00, 1.00] \times 10^{-2}$	$[-8.00, 8.00] \times 10^{-2}$
$(\delta^F)_{23}$	$[-1.60, 1.60] \times 10^{-2}$	$[-8.00, 8.00] \times 10^{-2}$
$(\delta^{TT})_{12}$	$[-8.69, 10.43] \times 10^{-4}$	$[-7.46, 8.95] \times 10^{-4}$
$(\delta^{TT})_{13}$	$[-1.74, 1.74] \times 10^{-3}$	$[-3.48, 1.74] \times 10^{-3}$
$(\delta^{TT})_{23}$	$[-0.0174, 0.145]$	$[-0.0871, 0.124]$
$(\delta^{FT})_{12}$	$[-4.64, 4.64] \times 10^{-5}$	$[-5.47, 5.47] \times 10^{-5}$
$(\delta^{FT})_{13}$	$[-7.74, 7.74] \times 10^{-5}$	$[-3.87, 3.87] \times 10^{-4}$
$(\delta^{FT})_{21}$	0.0	$[-1.04, 1.04] \times 10^{-4}$
$(\delta^{FT})_{23}$	$[-1.16, 1.16] \times 10^{-4}$	$[-2.32, 2.32] \times 10^{-4}$
$(\delta^{FT})_{31}$	$[-1.39, 1.39] \times 10^{-5}$	$[-8.81, 8.81] \times 10^{-5}$
$(\delta^{FT})_{32}$	0.0	$[-1.49, 1.49] \times 10^{-4}$

TABLE 4.2: Ranges of the NMFV parameters defined at the GUT scale (see Eq. (4.6)) for our multi-dimensional scans around the reference scenarios. The parameters given as 0.0 have been not been varied, since even small variations lead to tachyonic mass spectra and/or a charged LSP.

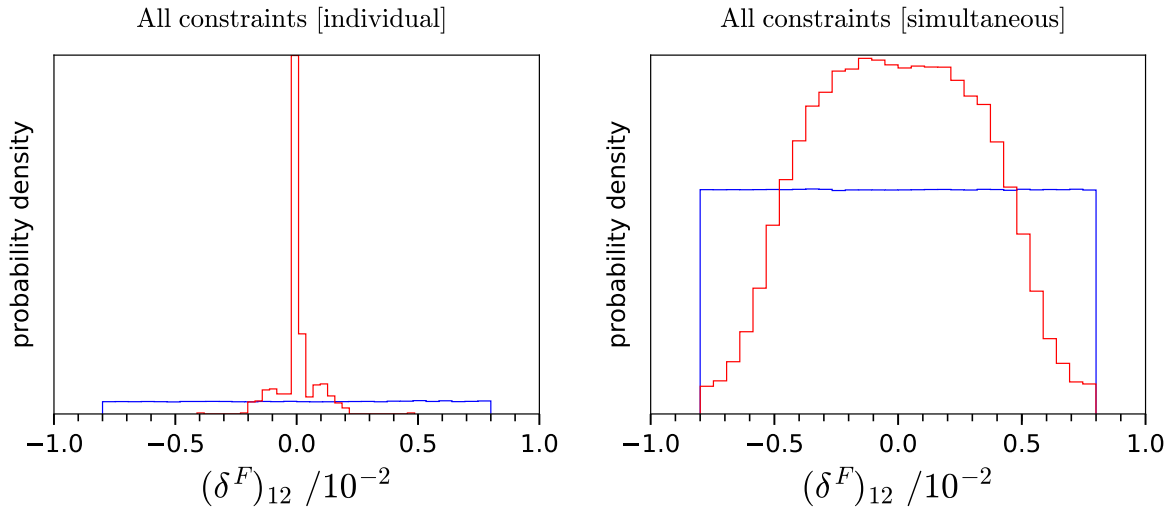

FIGURE 4.1: Comparison of individual vs. simultaneous scan of the NMFV parameter $(\delta^F)_{12}$ around Scenario 1 of Table 4.1. Each panel shows the prior (blue) together with the posterior (red) distributions obtained after imposing all relevant constraints.

spectrum obtained from `SPhenoMSSM` is handed to `micrOMEGAs` by making use of the *SUSY Les Houches Accord 2* [189]. Note that, since the spin-independent scattering cross-sections related to direct dark matter detection are relatively low as compared to the corresponding experimental limits, we do not explicitly evaluate these cross-section in our NMFV scan.

Starting from parameters at the GUT scale, we test each point against the observables marked in Table 2.1. Points which do not satisfy all the imposed constraints within the associated uncertainties are collected in the prior distribution only, while those which comply with all constraints are in addition recorded as part of the posterior distribution. In examining the latter, we obtained the allowed ranges for each of the NMFV parameters. In addition, by comparing the prior and posterior distributions, and taking into account posterior distributions based on a single constraint, we identify the most important constraints for each NMFV parameter.

Finally, note that although the reference scenarios defined in Table 4.1 have in part been obtained considering the anomalous magnetic moment of the muon as a key observable [177], we do not expect sizeable effects from NMFV terms on this observable within the ranges that are allowed from the other constraints. For this reason, and in addition given the fact that the numerical computation of the anomalous magnetic moment is difficult to perform within a model featuring NMFV terms, we do not take into account this constraint here.

Selected results: GUT-scale parameters

We have performed two different kinds of scan on the parameter space mentioned above: "individual" scans, where only one single NMFV parameter has been varied, while the others have been kept to zero, and "simultaneous" scans, where all NMFV parameters have been varied at the same time according to the ranges given in Table 4.2. From the comparison of the two scanning methods, we learn that the viable regions for each NMFV parameter are much larger for the case of simultaneous variation as compared to varying one parameter only. Indeed, it is possible that more than one of the NMFV parameters influences of one ore more given observables. In such a case, interferences and/or cancellations between the contributions induced by different NMFV-parameters may occur. As a consequence, they give rise to viable regions of parameter space that would not be fully explored when varying each parameter in isolation.

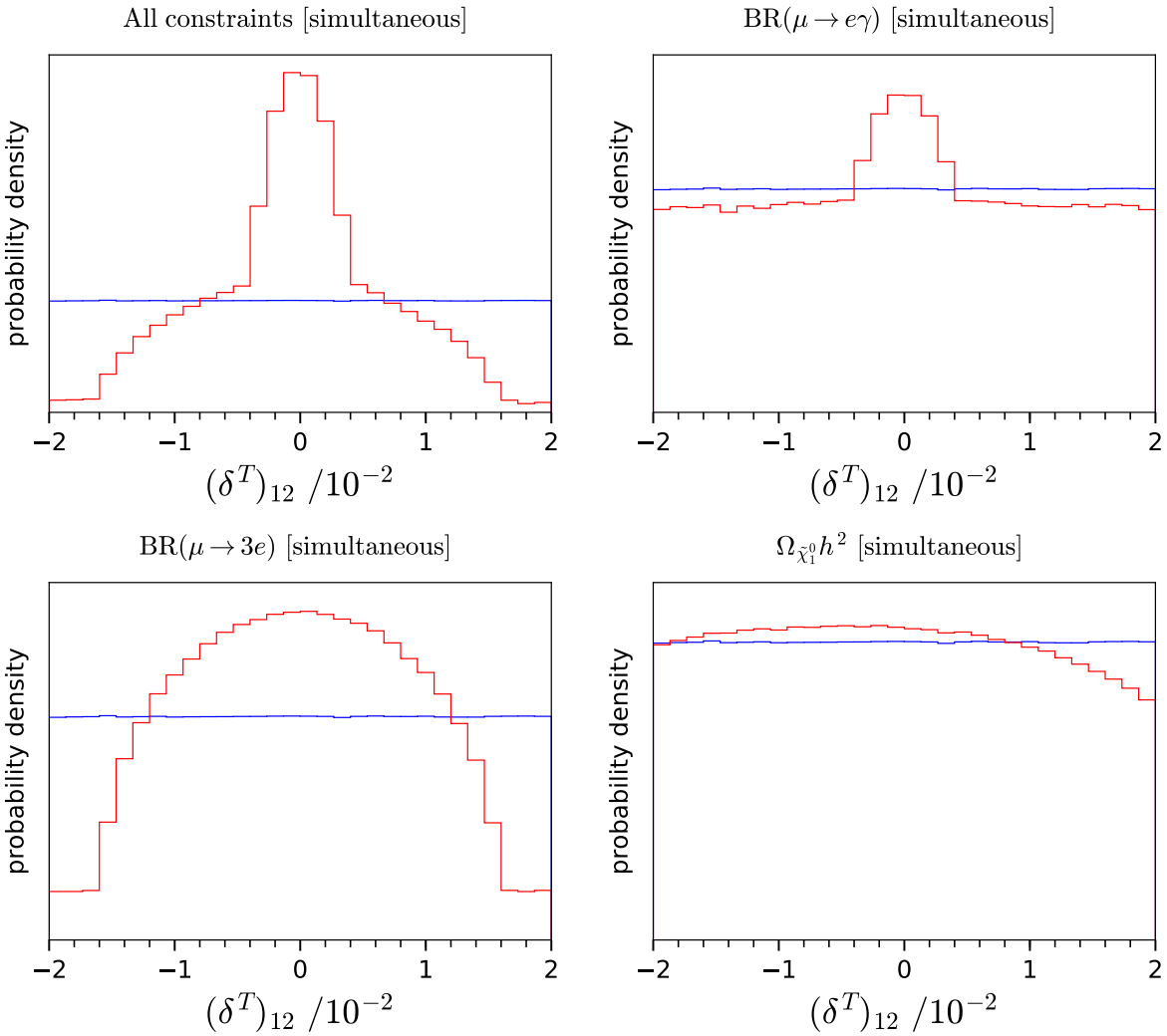

FIGURE 4.2: Dominant constraints on the parameter $(\delta^T)_{12}$ from simultaneous scan around Scenario 1. Prior distributions are given in blue and posterior distribution are given in red.

One such example is shown in Fig. 4.1. As can be seen, the posterior distribution resulting from the simulateous scan leads to a viable interval for the parameter $(\delta^F)_{12}$ that is by almost a factor of five larger than the one obtained from the individual scan. For this reason, I do not discuss further the results obtained from individual scanning, but focus on those obtained from the simultaneous scans.

From the multi-dimensional scan, we conclude that for the majority of the considered NMFV parameters, the most sensitive observables are the branching ratios of $\mu \to e\gamma$ and $\mu \to 3e$, as well as the neutralino relic density $\Omega_{\tilde{\chi}_1^0} h^2$. The impact of the relic density can be attributed to the small mass difference between the neutralino and the smuon, which depends strongly on the off-diagonal elements in the slepton mass matrix. Since both our reference scenario exhibit a relatively small value of $(M_T)_{22}$, already rather tiny flavour violating elements can be excluded by current data.

In many cases, the obtained posterior distribution is a superposition of the posteriors stemming from the individual constraints. This is illustrated in Fig. 4.2 for the parameter $(\delta^T)_{12}$, where the three constraints mentioned above have a significant impact. In other cases, one constraint is dominant with respect to the others. Such an example is shown in Fig. 4.3 for the parameter $(\delta^F)_{12}$, where the posterior obtained with the contraint of $\mu \to 3e$ alone basically

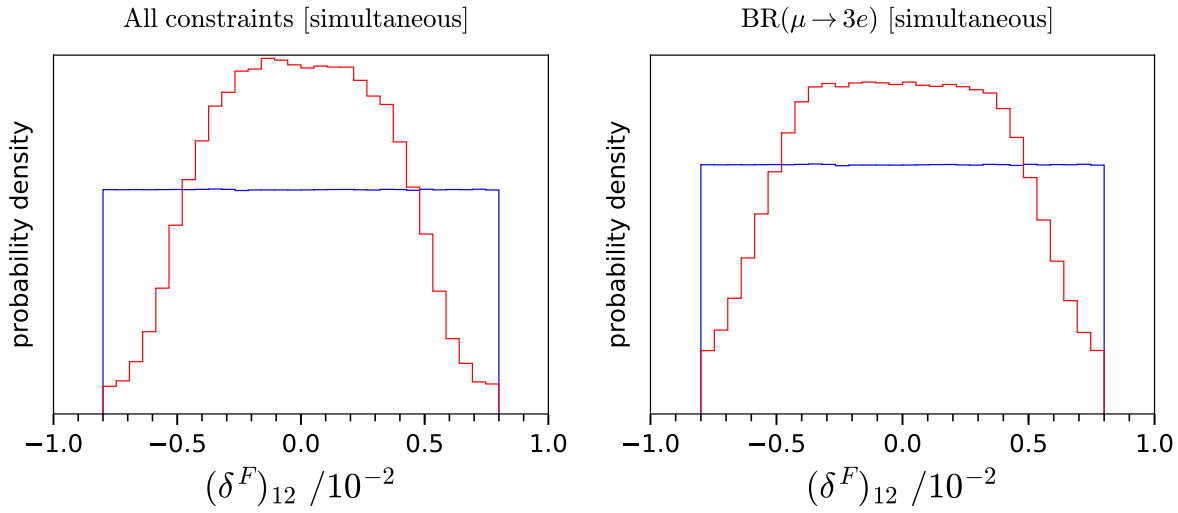

FIGURE 4.3: Dominant constraints on the parameter $(\delta^F)_{12}$ from simultaneous scan around Scenario 1. Prior distributions are given in blue and posterior distribution are given in red.

gives the same shape as the one obtained when imposing all constraints.

The fact that $\mu \to 3e$ may be the dominant constraint, as seen in the previous example, can be somewhat surprising. Although the experimental limit is more stringent (by about a factor of two) for the decay $\mu \to e\gamma$, the $\mu \to 3e$ decay has about the same constraining power and is in certain cases even the dominant constraint. This is explained as follows: The amplitude of $\mu \to e\gamma$ is helicity-suppressed, and therefore contains a suppression factor m_e/m_μ. While this is also the case for $\mu \to 3e$ diagrams related to those of $\mu \to e\gamma$, there are additional four-point diagrams, where the helicity suppression is lifted since no photon is involved. Despite the additional gauge coupling and the greater degree of loop suppression, these diagrams are numerically competitive to those of $\mu \to e\gamma$.

A somewhat unexpected posterior distribution appears for the parameter $(\delta^T)_{13}$ shown in Fig. 4.4. This parameter is constrained only by the neutralino relic density and the flavour constraints have no effect. Other NMFV parameters are allowed under flavour constraints to shift significantly away from zero. This has a marked effect in reducing superpartner masses which are determined by diagonalising the mass-squared matrices. This applies in particular to the "right-handed" smuon mass, as the initial smallness of $(M_T)_{22}$ means that small NMFV parameters can slightly lower the smuon mass. As a further consequence, the relic density is then reduced due to the smaller mass difference between smuon and neutralino, which increases the importance of co-annihilation and smuon pair annihilation. However, the smuon mass also is influenced by $(\delta^T)_{13}$, which by virtue of being unconstrained by flavour observables, may be non-zero. Moreover, this particular parameter increases the lightest smuon mass due to the specific hierarchies in the mass matrix. The smuon mass being decreased by other non-zero NMFV parameters, $(\delta^T)_{13}$ being non-zero then re-establishes the initial mass difference between the smuon and neutralino allowing the relic density to stay within the Planck limits. Relaxing the assumption that the neutralino $\tilde{\chi}_1^0$ is the only dark matter candidate, i.e. relax the lower limit on the relic density, the caracteristic shape observed for $(\delta^T)_{13}$ in Fig. 4.4 disappears.

We find that NMFV parameters mixing the first or second generation with the third generation are also mainly constrained by the decays $\mu \to e\gamma$ and $\mu \to 3e$ rather than by the corresponding τ decays such as $\tau \to \mu\gamma$ or $\tau \to e\gamma$. This can be traced to the better experimental precision of the muonic decay measurements with respect to the analogous tau decays.

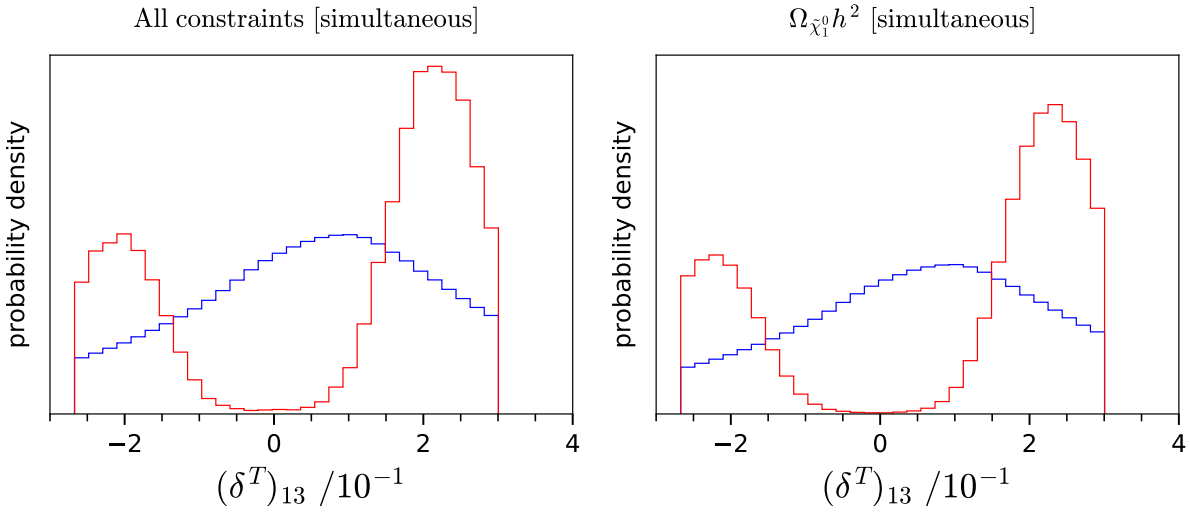

FIGURE 4.4: Dominant constraints on the parameter $(\delta^T)_{13}$ from simultaneous scan around Scenario 2. Prior distributions are given in blue and posterior distribution are given in red.

Even though NMFV parameters mediating $e-\tau$ or $\mu-\tau$ transitions lead to the dominant contributions of the tau decays, these parameters also can enter into the muon decay amplitudes. For example, if the $\mu \to e\gamma$ process includes a stau in the loop, the corresponding amplitude is proportional to terms including products of the type $(\delta)_{23}(\delta)_{13}$. Since the muon decay limits are stronger than the tau decay limits by four to five orders of magnitude, the $e-\tau$ and $\mu-\tau$ mixing parameters are constrained by the $e-\mu$ processes first.

Finally, it is to be noted that the constraints coming from the hadronic sector, such as the decays $B \to X_s\gamma$ or $B_s \to \mu^+\mu^-$, which are dominant in the case of NMFV in the squark sector alone as discussed in Sec. 2.2, are not competitive as compared to the leptonic constraints mentioned above. This can be traced to the greater experimental precision of dedicated leptonic measurements compared to meson decays.

Altogether, the simultaneous studies of all NMFV parameters for both reference scenarios of Table 4.1 lead to the viable ranges summarized in Table 4.3 for the different NMFV parameters.

Selected results: TeV-scale parameters

While from the model-building point of view it is useful to explore the allowed level of flavour violation at the GUT scale, it is equally important to explore the resulting physics at the SUSY scale. Renormalization group running from the GUT scale to the SUSY scale will break the unification conditions given in Eq. (4.5) and consequently in Eq. (4.6). The fact that these relations are not valid any more below the GUT scale is an essential and intrinsic part of Grand Unification. The present Section is devoted to highlighting selected results related to the NMFV parameters obtained at the SUSY scale. More precisely, we study the behaviour of different SUSY scale NMFV parameters which stem from a single NMFV parameter at the GUT scale.

In Fig. 4.5 we show the example of $\left(\delta^F\right)_{12}$, defined at the GUT scale, and the two resulting SUSY scale parameters $\left(\delta^L_{LL}\right)_{12}$ and $\left(\delta^D_{RR}\right)_{12}$, which belong to the slepton and down-type squark sectors, respectively. First, we see that the prior distribution is altered by the renormalization group effects between the GUT scale in panel a) and the SUSY scale distributions in panels b) and c). The imposed flat priors at the GUT scale are transformed into almost Gaussian-like distributions at the SUSY scale. Looking at the corresponding posteriors, the SUSY scale distributions look even more peaked than the corresponding GUT scale histrograms.

Parameters	Scenario 1	Most constraining obs. 1	Scenario 2	Most constraining obs. 2
$(\delta^T)_{12}$	[-0.015, 0.015]	$\mu \to 3e$, $\mu \to e\gamma$, $\Omega_{\tilde{\chi}_1^0}h^2$	[-0.12, 0.12]†	$\Omega_{\tilde{\chi}_1^0}h^2$, $\mu \to e\gamma$
$(\delta^T)_{13}$	]-0.06, 0.06[	$\Omega_{\tilde{\chi}_1^0}h^2$	[-0.3, 0.3]†	$\Omega_{\tilde{\chi}_1^0}h^2$
$(\delta^T)_{23}$	[0,0]*	$\Omega_{\tilde{\chi}_1^0}h^2$, $\mu \to 3e$, $\mu \to e\gamma$	[-0.1, 0.1]†	$\Omega_{\tilde{\chi}_1^0}h^2$, $\mu \to 3e$, $\mu \to e\gamma$,
$(\delta^F)_{12}$	[-0.008, 0.008]	$\mu \to 3e$, $\mu \to e\gamma$	[-0.015, 0.015]†	$\mu \to 3e$, $\mu \to e\gamma$
$(\delta^F)_{13}$	]-0.01, 0.01[	$\mu \to e\gamma$	[-0.15, 0.15]†	$\mu \to 3e$, $\mu \to e\gamma$
$(\delta^F)_{23}$	]-0.015, 0.015[	$\mu \to e\gamma$, $\Omega_{\tilde{\chi}_1^0}h^2$	[-0.15, 0.15]†	$\Omega_{\tilde{\chi}_1^0}h^2$, $\mu \to e\gamma$, $\mu \to 3e$
$(\delta^{TT})_{12}$	[-3, 3.5] $\times 10^{-5}$	prior	[-1, 1.5]† $\times 10^{-3}$	prior, $\Omega_{\tilde{\chi}_1^0}h^2$
$(\delta^{TT})_{13}$	]-6, 7[$\times 10^{-5}$	prior, $\Omega_{\tilde{\chi}_1^0}h^2$	[-4, 2.5]† $\times 10^{-3}$	prior, $\Omega_{\tilde{\chi}_1^0}h^2$
$(\delta^{TT})_{23}$	]-0.5, 4[$\times 10^{-5}$	prior, $\Omega_{\tilde{\chi}_1^0}h^2$	[-0.25, 0.2]†	prior, $\Omega_{\tilde{\chi}_1^0}h^2$
$(\delta^{FT})_{12}$	[-0.0015, 0.0015]	$\Omega_{\tilde{\chi}_1^0}h^2$	[-1.2, 1.2]† $\times 10^{-4}$	$\mu \to 3e$, $\Omega_{\tilde{\chi}_1^0}h^2$, $\mu \to e\gamma$
$(\delta^{FT})_{13}$	]-0.002, 0.002[	$\Omega_{\tilde{\chi}_1^0}h^2$	[-5, 5] $\times 10^{-4}$	$\Omega_{\tilde{\chi}_1^0}h^2$, $\mu \to 3e$, $\mu \to e\gamma$
$(\delta^{FT})_{21}$	[0,0]*	prior	[-1.2, 1.2]† $\times 10^{-4}$	$\Omega_{\tilde{\chi}_1^0}h^2$, prior
$(\delta^{FT})_{23}$	]-0.0022, 0.0022[	$\Omega_{\tilde{\chi}_1^0}h^2$	[-6, 6]† $\times 10^{-4}$	$\mu \to 3e$, $\Omega_{\tilde{\chi}_1^0}h^2$, $\mu \to e\gamma$
$(\delta^{FT})_{31}$	]-0.0004, 0.0004[	$\Omega_{\tilde{\chi}_1^0}h^2$	[-2, 2]† $\times 10^{-4}$	$\Omega_{\tilde{\chi}_1^0}h^2$
$(\delta^{FT})_{32}$	[0,0]*	prior	[-1.5, 1.5] $\times 10^{-4}$	$\Omega_{\tilde{\chi}_1^0}h^2$

TABLE 4.3: Estimated allowed GUT scale flavour violation for both reference scenarios and impactful constraints ordered from the most to the least constraining. Where square brackets are shown open, we scan up to these values but even if we noticed some impact from constraints, it seems that the allowed region can be larger and extrapolation to concrete limits is not straightforward. * denotes parameters fixed to 0 in order to satisfy LSP and physical mass spectrum requirements. The ranges marked with a † are extrapolated, meaning that the posterior does not actually drop to 0 but extrapolation to a limit is reasonable. A parameter that is constrained by 'prior' is limited by LSP and physical mass requirement.

Second, it is interesting to note that, at the SUSY scale, the allowed range for the hadronic parameter $\left(\delta^D_{RR}\right)_{12}$ is wider than that for the related leptonic parameter $\left(\delta^L_{LL}\right)_{12}$ in the simultaneous scan. This behaviour is somewhat unexpected, since the gluino running, which is blind to flavour, drives the diagonal squark mass parameters higher, while it leaves the leptonic ones unaffected. In turn, this is expected to reduce the squark NMFV parameters [115]. We find that this behaviour is confirmed for all NMFV parameters stemming from *individual* scans (see examples in Fig. 4.5 panels d) and e)), agreeing with the results presented in Ref. [115]. However, for the δ^F parameters, the reverse is true when considering the *simultaneous* scan. We suspect that strong renormalization group effects are the cause of this feature, due to the fact that mutliple NMFV parameters interact with each other during the evolution from the GUT scale to the SUSY scale.

Parameter correlations

We finally examine more closely the correlation between certain NMFV parameters, mentioned already several times in the above discussion, and being the reason that scanning over all parameters simultaneously is ultimately required. The key is that cancellations may exist between the contributions from certain parameters in the calculation of a given observable. However, dealing with analytical results for the different experimental constraints is difficult and beyond the scope of this work. Instead, we choose to take advantage of the numerical results, showing posterior distributions of more than one NMFV parameter together.

The first panel in Fig. 4.6 shows viable parameter points that seem to follow a line, with an increased density of points concentrated around a linear relationship between the GUT scale parameters $\left(\delta^F\right)_{12}$ and $\left(\delta^{FT}\right)_{12}$. Indeed, the impact of $\mathrm{BR}\left(\mu \to e\gamma\right)$ is suppressed in this line due to cancellation between the two parameters in the analytic expression for this observable. One can also see this in the right panel, only those points lying close to or along said correlation line are consistent with the experimental limits. Said correlation could provide an interesting hint for future SUSY GUT model building.

The analytic expression for the decay rate of $\mu \to e\gamma$ can be written as [115]

$$\frac{\mathrm{BR}(\ell_i \to \ell_j \gamma)}{\mathrm{BR}(\ell_i \to \ell_j \nu_i \nu_j)} = \frac{48\pi^3 \alpha}{G_F^2}\left(|F_L^{ij}|^2 + |F_R^{ij}|^2\right) \tag{4.7}$$

where the branching ratio of the decay $\ell_i \to \ell_j \nu_i \nu_j$ is a constant with respect to the NMFV parameters under consideration in the present work. For real NMFV parameters, the form factors $F_{L,R}$ are related to the flavour violating parameters at the SUSY scale according to

$$\begin{aligned} F_L^{ij} &= c_1(\delta^e_{LL})_{ij} + c_2(\delta^e_{RL})_{ij}\,, \\ F_R^{ij} &= c_3(\delta^e_{RR})_{ij} + c_4(\delta^e_{RL})_{ji}\,. \end{aligned} \tag{4.8}$$

The coefficients c_i $(i = 1, \ldots, 4)$ are combinations of loop factors, masses, and other numerical inputs which can be assumed to be constant in our analysis. Minimizing the form factors $F_{L,R}$ in Eq. (4.8) to yield small $\mu \to e\gamma$ branching ratios and hence satisfy the experimental constraint leads to relations of the form

$$(\delta^e_{LL})_{ij} = -\frac{2c_2}{c_1}\,(\delta^e_{RL})_{ij}\,, \tag{4.9}$$

corresponding to the observed lines in Figs. 4.6. As such, the correlation that we recover purely from our numerical analysis is consistent with the analytic formulae for this lepton flavour-violating decay.

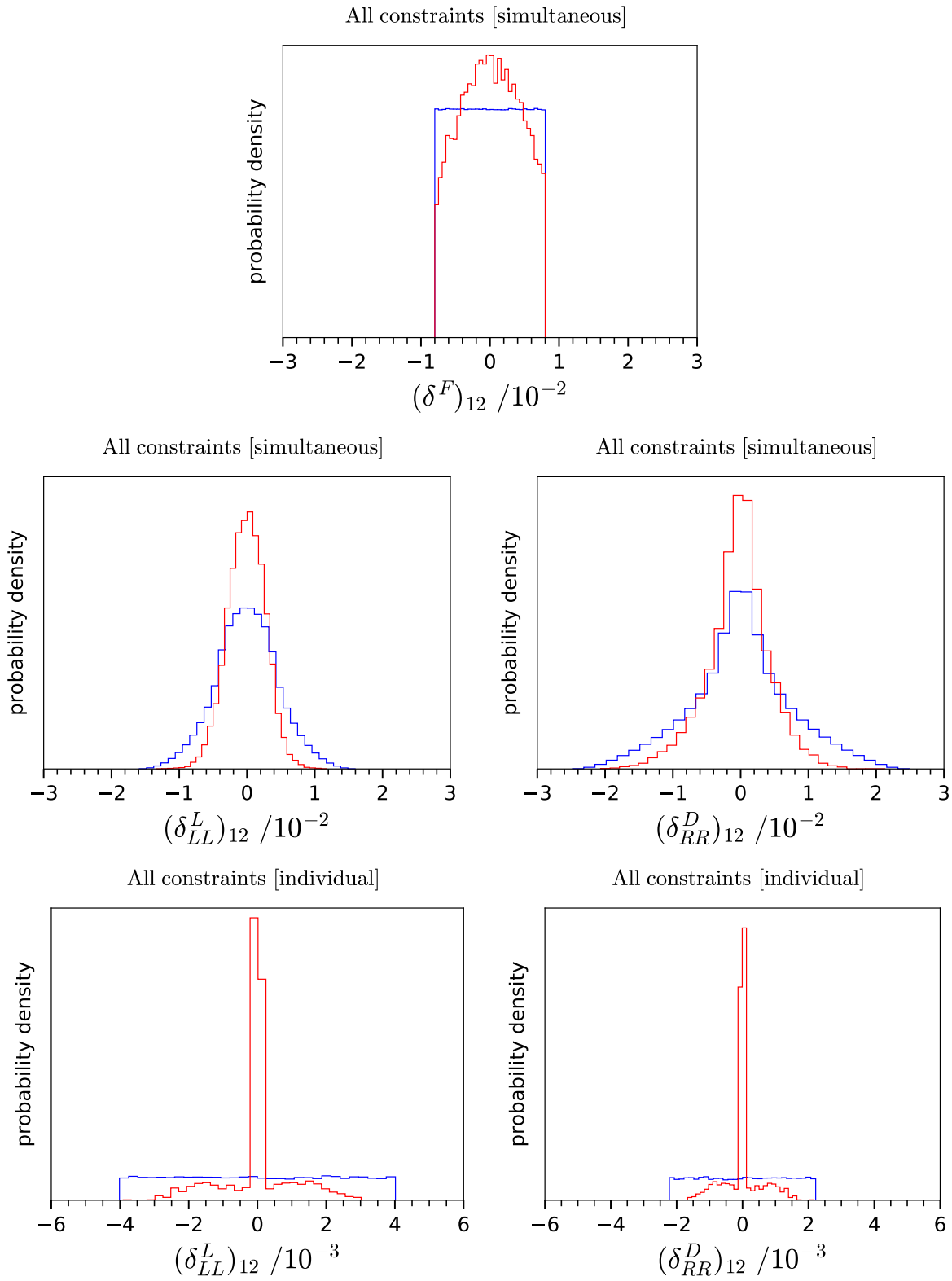

FIGURE 4.5: Distributions obtained for the GUT-scale parameter $(\delta^F)_{12}$ and the associated SUSY-scale parameters $(\delta^e_{LL})_{12}$ and $(\delta^d_{RR})_{12}$ (see Eq. (1.39)) from simultaneous and individual scan around Scenario 2 of Table 4.1. Analogously to other results, prior distributions are shown in blue and posterior distributions are shown in red.

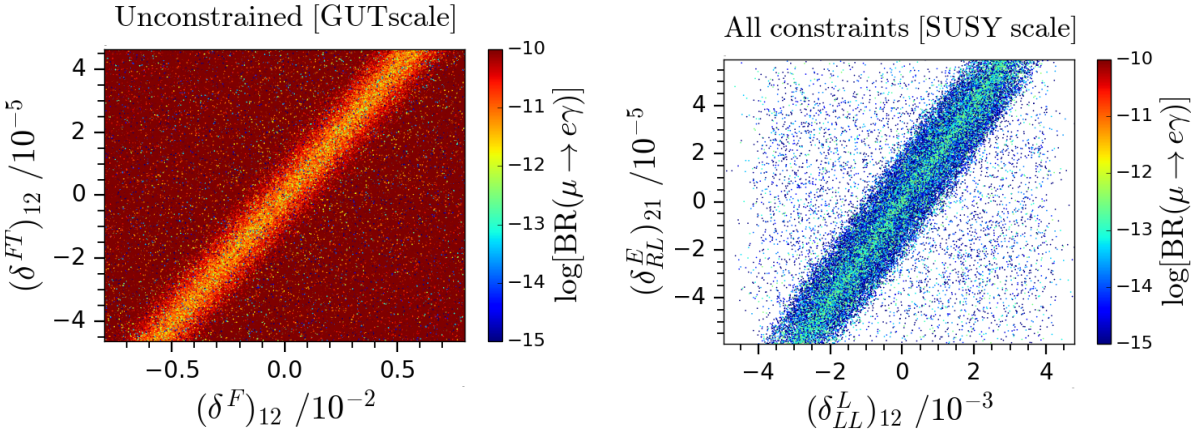

FIGURE 4.6: Correlation of the GUT-scale parameters $\left(\delta^{F}\right)_{12}$ and $\left(\delta^{FT}\right)_{12}$ (left panel) and associated correlation of the SUSY-scale parameters $\left(\delta^{e}_{LL}\right)_{12}$ and $\left(\delta^{e}_{RL}\right)_{12}$ (right panel) for Scenario 1. While the first plot shows the results for the full scan, the second one shows only the surviving points once the constraints of Table 2.1 are applied.

Concluding remarks

Precision flavour physics measurements could present challenges to this work and war- rant further attention. Particularly, situations such as this often predict small-but-non-zero branching ratios for the LFV decays $\mu \to e\gamma$ and $\mu \to 3e$, hence stricter bounds on such processes will further limit the amount of NMFV allowed in such scenarios. Figs. 4.6 is purely data-driven and shows the regions that experimental data prefers. A model which predicts such a correlation could allow reasonable flavour violation and still be preferred over other such models.

In general, we have examined the relation between GUT-scale and low-scale flavour-violating parameters, for both quarks and leptons, and shown how the usual expectations may be violated due to the correlations when multiple parameters are varied simultaneously. We have presented results in the framework of non-minimal flavour violation in $A_4 \times SU(5)$ inspired Supersymmetric Grand Unified Theories, with smuon-assisted dark matter. While such a framework is appealing since it allows both successful dark matter and contributions to $(g-2)_\mu$, as well as providing the smoking gun prediction of a light right-handed smuon accessible at LHC energies, it will be interesting to pursue similar studies in more complete frameworks relating the quark and lepton sectors.

Chapter 5

Outlook and perspectives

Having disucussed selected results in Chaps. 2 to 4, in this last part of the present Manuscript, I will address open questions as well as ideas and perspectives, mainly stemming from the presented work.

Generally, I see my mid-term future work in the direction of flavour-related observables in beyond the Standard Model physics, as well as the interplay between flavour physics, collider searches, and dark matter aspects of new physics. While almost all my previous work has been realized within supersymmetric models, I have started to broaden my activities to other models such as, some years ago, the Inert Doublet Model [53, 190] as an example of a non-supersymmetric Two-Higgs Doublet Model. More recently, I have become interested in extensions of the Standard Model where neutrino masses are generated radiatively by adding suitable fermionic and scalar singlets or doublets [191], such as, e.g., in the so-called scotogenic model [61], to cite a simple example of such a setup. Moreover, models including leptoquarks present interesting phenomenological aspects and are rather well-motivated from the point of view of the recent hints towards potential lepton-flavour non-universality [192].

In this perspective, my short- and mid-term research project mainly aims at methods to identify the underlying theory framework of beyond the Standard Model physics based on simple observables, at colliders but also in other sectors. A second aspect is the exploration of so-called *M*achine-Learning techniques, which provide promising computational techniques and are, in my opinion, under-explored in particle physics phenomenology.

In the following, I will briefly outline the directions and perspectives that I am planning to explore in the coming years.

5.1 Flavoured Grand Unification in Supersymmetry

As discussed in Chap. 4, models based on the gauge group $SU(5)$ at some high energy scale provide a viable unification framework together with a rich phenomenology. An example of a concrete model based on the flavour symmetry A_4 [177, 171] has been discussed including an approach to go beyond the Minimal Flavour Violation (MFV) paradigm. While this is a suitable starting point and gives insight on the structure of such a setup, the discussed framework is rather simple and its implementation in Ref. [171] has followed a somewhat simplifying phenomenological approach.

In this Section, I discuss potential ways to improve the analsysis presented in Chap. 4. Moreover, I briefly sketch ongoing and future work aiming at testing the hypothesis of Grand Unification at present and future colliders.

Study of a $S_4 \times SU(5)$ supersymmetric model

It has to be noted that models based on the gauge group $SU(5)$ are in certain cases disfavoured, since in such a setup proton decay may be allowed in contrast to experimental observation [193]. It should also be noted that, although the study presented in Chap. 4, based on Refs.

[177, 171] is a suitable and instructive starting point for this type of analysis, it is probably too restrictive concerning the covered parameter space on the one hand, and the somewhat *ad-hoc* implementation of the flavour violating terms at the unification scale on the other hand. Concerning the last point, the precise structure of the Non-Minimally Flavour Violating terms should in fact be governed by the flavons of the theory, which acquire a vacuum expectation value when the flavour symmetry is broken. Concerning the former point, extending the analyses towards other groups, e.g., $SO(10)$ or E_6, will be a logical step.

We are currently aiming at a more complete study of a more predictive model, still based on $SU(5)$-like unification, but including a S_4 flavour symmetry. We intend to perform a Markov-Chain Monte Carlo study of the full parameter space, i.e. varying the flavour-conserving and flavour-violating parameters at the same time. This will allow to better understand possible correlations between flavour-violating parameters at the GUT and the TeV scale, and give valuable hints in the context of further model building in this direction.

I would like to point out that the study of unified models are particularly interesting in the present experimental context, since leptonic constraints are, as seen in Chap. 4, in most cases more stringent than the hadronic ones, but the coloured sector might be easier accessible at the Large Hadron Collider. In all studies of this kind of models, it is therefore important not only to identify the viable regions of parameter space, but also to determine the associated collider phenomenology.

Footprints of $SU(5)$-like unification at the TeV scale

While studies carried out directly at the unification scale, as described above, are important in the understanding of the theory's structure, especially concerning flavour, the link to TeV-scale observables is of utmost importance. For this reason, I have become interested in developping methods allowing to test Grand Unification at TeV-scale collider, in particular the Large Hadron Collider.

Unravelling whether or not Nature is $SU(5)$-symmetric at short distances constitutes a challanging and interesting question. Many realizations of $SU(5)$-like Grand Unified Theories are possible, with various consequences at the TeV scale. Moreover, a large amount of information can be lost in the renormalization group evolution between the GUT and the TeV scales. A test of the $SU(5)$ hypothesis therefore has to face both challenges of avoiding a large model-dependence and being realizable based on low-scale observables.

As discussed in Chap. 4, the unification of matter fields implies certain relations at the level of the Yukawa couplings, see Eq. (4.3), as well as at the level of soft mass and trilinear matrices, see Eqs. (4.5). Let us first note that the relations

$$Y_d = Y_e^t \qquad \text{and} \qquad A_d = A_e^t \,, \tag{5.1}$$

which are exact at the GUT scale, provided that corrections arising from integrating out heavy GUT states are negligible, will be spoiled by the differences in the β-functions between the two sectors during the renormalization group evolution towards the TeV scale, and can therefore not serve as basis for a phenomenological test of the $SU(5)$ hypothesis.

Focusing instead on the sector of up-type squarks, let us recall that the top Yukawa coupling as well as the associated trilinear coupling are symmetric at the Grand Unification scale,

$$Y_u = Y_u^t \,, \qquad A_u = A_u^t \,, \tag{5.2}$$

if we assume that Supersymmetry breaking does not break the $SU(5)$ symmetry. While the symmetry of the Yukawa matrix is not particularly exploitable, the symmetry of the trilinear matrix will be able to provide tests of the $SU(5)$-hypothesis at the TeV scale.

The reason is that the two relations given in Eq. (5.2) are confined to the flavour space of the up-type (s)quarks, and are therefore more stable against quantum corrections as compared to the relations given in Eq. (5.1) which relate two different flavour sectors. Moreover, there is no connection between the symmetry of A_t and potentially dangerous flavour-changing neutral currents in the down-type sector. Consequently, the two matrices remain symmetric to good precision at the TeV scale. This can be understood by examining the corresponding β-functions,

$$16\pi^2\beta_{Y_u} = Y_u\left[3\mathrm{Tr}\{Y_u^\dagger Y_u\} + 3Y_u^\dagger Y_u + Y_d^\dagger Y_d - \frac{16}{3}g_3^2 - 3g_2^2 - \frac{13}{15}g_1^2\right], \tag{5.3}$$

$$\begin{aligned}16\pi^2\beta_{A_u} = {} & A_u\left[3\,\mathrm{Tr}\{Y_u^\dagger Y_u\} + 5\,Y_u^\dagger Y_u + Y_d^\dagger Y_d - \frac{16}{3}\,g_3^2 - 3\,g_2^2 - \frac{13}{15}\,g_1^2\right] \\ & + Y_u\left[6\,\mathrm{Tr}\{A_u Y_u^\dagger\} + 4\,Y_u^\dagger A_u + 2\,Y_d^\dagger A_d + \frac{32}{3}\,M_3^2 + 6\,M_2^2 + \frac{26}{15}\,M_1^2\right].\end{aligned} \tag{5.4}$$

In these expressions, the trace and gauge terms are flavour singlets, and the term $Y_u Y_u^\dagger Y_u$ is symmetric by hypothesis. The only non-symmetric term in Eq. (5.3) is $Y_u Y_d^\dagger Y_u$. In Supersymmetry, the relative magnitude of the up- and down-type Yukawa couplings depends on $\tan\beta$, so that the contribution of this term to the asymmetry grows with $\tan\beta$. Given the observed quark masses, one expects $Y_d^\dagger Y_d$ to compete with $Y_u^\dagger Y_u$ only for very large values of $\tan\beta$. Moreover, the $Y_u Y_d^\dagger Y_u$ contribution is suppressed by the elements of the CKM matrix, as Y_d and Y_u would commute if they were simultaneously diagonalizable. We can therefore expect that Y_u remains symmetric to a very good approximation at the TeV scale.

Coming to Eq. (5.4), all terms except the gauge and trace terms are generally non-symmetric. The trilinear coupling A_u stays symmetric to a good precision at low energies only if the renormalization group flow is dominated by gauge contributions, and having a symmetric A_u at the TeV scale does not seem such a generic feature. In practice, however, the beta function is often dominated by the large gluino mass contribution. Moreover, as this contribution is positive, it decreases A_u with the energy, such that the non-symmetric terms become smaller and smaller in the beta function. Therefore, we can expect that the asymmetry of A_u at the TeV scale remains small in many concrete cases.

For practical purposes, we introduce the quantities

$$\mathcal{A}_{ij} = \left.\frac{\left|(A_u)_{ij} - (A_u)_{ji}\right|}{\mathrm{Tr}\{\mathcal{M}_{\sqcap}\}^{1/2}}\right|_{Q=1\text{ TeV}} \qquad (i \neq j)\,, \tag{5.5}$$

parametrizing the asymmetry of the trilinear up-squark matrix A_u. The normalization to trace of the up-squark mass matrix $\mathrm{Tr}\{\mathcal{M}_{\sqcap}\}$, which is representative of the SUSY scale, renders the asymmetry dimensionless and independent of the overall scale of the reference scenarios. As flavour mixing involving the first generation of squarks is strongly suppressed, we focus on the asymmetry $\mathcal{A}_{23}$ stemming from potential top-charm mixing in the squark sector. The relation to be tested at the TeV scale, e.g., at collider experiments, is thus

$$\boxed{A_u \approx A_u^t \qquad \Longleftrightarrow \qquad \mathcal{A}_{23} \approx 0\,.} \tag{5.6}$$

The main dependence of $\mathcal{A}_{23}$ is with respect to the parameters $(A_u)_{23,32}$ and $(A_d)_{23,32}$. In order to evaluate numerically the resulting asymmetry at the TeV scale, we have varied these parameters around several reference scenarios assuming that the $SU(5)$ hypothesis is true, i.e. $(A_u)_{23} = (A_u)_{32}$ at the GUT scale. For simplicity, we also assume $(A_d)_{23} = (A_d)_{32}$. We evaluate the TeV-scale asymmetry $\mathcal{A}_{23}$ defined in Eq. (5.5) using the numerical spectrum calculator `SPheno` [121, 122]. We find that for typical scenarios featuring not too large values of $\tan\beta \lesssim 40$,

as expected from renormalization group considerations, the resulting asymmetry does not exceed a few percent. During the era of the Large Hadron Collider, a better experimental precision will be difficult to reach. For details on this numerical study, the interested reader is referred to Refs. [194, 195].

Testing $SU(5)$-like unification at colliders

Any strategy that can be set up to test the $SU(5)$ relation $a_u \approx a_u^t$ necessarily relies on a comparison involving at least two up-squarks. Apart from this relation, the squark matrix is in general arbitrary, so that each of the six up-type squarks can take any mass. Some of the squarks can be light enough to be produced on-shell at the LHC, while others may be too heavy such that they appear only virtually in intermediate processes.

As a result, a panel of possibilities for $SU(5)$ tests will appear, depending on the exact features of the up-squark spectrum. It can be convenient to split the possibilities of $SU(5)$ tests into three categories, depending on whether the tests involve only virtual, both virtual and real, or only real up-type squarks. Note that the $SU(5)$ tests on virtual up-type squarks will necessarily involve one-loop processes, because the interaction terms probed in the tests are R-parity conserving. In contrast, the $SU(5)$ tests on real squarks can in principle rely on tree-level processes only. The present discussion is inspired by the work presented in Refs. [196, 194], as well as the current follow-up study [195].

Instead of dealing with the full six-dimensional mass matrix $\mathcal{M}_{\tilde{u}}^2$ of Eq. (1.33), two expansions can be used in order to simplify the situation and depending on the pattern of $\mathcal{M}_{\tilde{u}}^2$: the mass insertion approximation (MIA) and the effective field theory (EFT) expansion.

The MIA is an expansion with respect to small eigenvalues-splittings, and is in particular valid in presence of small off-diagonal elements. In contrast, the EFT expansion can be applied if a large hierarchy is present in $\mathcal{M}_{\tilde{u}}^2$. The heavy up-type squarks with mass matrix M^2 are integrated out, the expansion parameter is $E^2\hat{M}^{-2}$, and M^2 can have arbitrary off-diagonal entries. The two expansions are therefore complementary.

It is clear that the feasibility of the $SU(5)$ tests we will setup depends crucially on the amount of data available – whether they involve real or virtual squarks. This feasibility needs to be quantified using appropriate statistical tools. Whenever a $SU(5)$ test can be obtained through a definite relation among observables, a frequentist p-value can be used in order to evaluate to which precision this relation can be tested, for given significance and amount of data.

The rather technical details associated with the squark effective theory and the mass insertion approximation are not presented in detail in this manuscript. The interested reader can find the relevant information and details in Refs. [196, 194, 195].

These techniques have allowed to set up tests for specific assumptions on the mass spectrum of the squarks. As a first example, assuming "natural" Supersymmetry, where first and second generation squarks are considerably heavier than those associated to the third generation, a test of the $SU(5)$ hypothesis has been defined based on the flavour-changing decays of a stop-like squark into a bino- or wino-like neutralino plus a jet containing up or charm flavour. As a second example, assuming two generations of squarks to be accessible at the Large Hadron Collider, a test can be defined based on the decays of charm-flavoured squarks into top-flavoured ones plus a Higgs boson. A third example is the case of heavy Supersymmetry, where no superpartner would be observed at the Large Hadron Collider, and they would only manifest as virtual effects in effective operators. In such a case, the $SU(5)$ relation can be tested using top polarimetry or ultraperipheral searches. A detailed discussion of these tests can be found in Refs. [196, 194, 195] and will not in detail be reproduced here.

The analysis of such specific mass orderings can be taken as a guideline to build more global tests of the $SU(5)$ hypothesis. In particular, the flavour-changing squark decays with

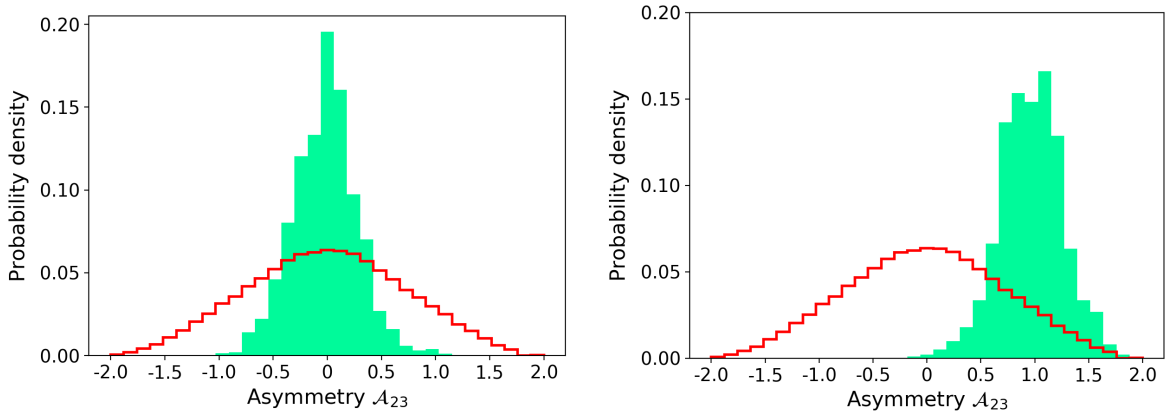

FIGURE 5.1: Posterior distributions of the asymmetry $\mathcal{A}_{23}$ obtained from a Markov Chain Monte Carlo scan for an $SU(5)$ example (left) and a non-$SU(5)$ counter-example (right).

Higgs-boson production are expected to always carry relevant information regarding the relation $A_u \approx A_u^t$ for any mass ordering. Such a global test constitutes a natural extension to the cases discussed above.

These tests, however, apply only to specific mass hierarchies, such as, e.g., natural Supersymmetry, where only the stops are relatively light, or the situation where all superpartners are too heavy to be produced at the Large Hadron Collider. In practice, however, it is not guaranteed that the mass spectrum respects such specific hierarchies. Moreover, before having observed a certain number of new states, the exact mass hierarchies are unknown. It is therefore necessary and interesting to set up techniques that allow to test Grand Unification hypothesis without specific assumptions on the physical masses.

First steps in this direction have been undertaken in collaboration with my former Ph.D. student Yannick Stoll [195]. We have constructed a test of the $SU(5)$ hypothesis based on Bayesian statistics. The latter gives the possibility to compare two models with respect to a certain amount of data by means of the Bayes factor, or in the present case of nested models the so-called Savage Dickey density ratio (SDDR). More precisely, we compare the $SU(5)$ case, where the asymmetry defined in Eq. (5.5) is $\mathcal{A}_{23} \approx 0$, to the non-$SU(5)$ case, where $\mathcal{A}_{23} \not\approx 0$.

In the present case, the SDDR can be computed as the ratio of the constrained and the unconstrained probability distrution functions evaluated at $\mathcal{A}_{23} = 0$. For the former, we have included observables assumed to be experimentally accessible, such as ratios of squark masses and event rates as already in Sec. 3. Moreover, the outcome of the test depends on the uncertainties associated to each observable. Figure 5.1 shows the result for a rather optimistic situation, i.e. assuming a high integrated luminosity of $\mathcal{L}^{\text{int}} = 3000\ \text{fb}^{-1}$ leading to rather small uncertainties below 1% for squark mass ratios, event rate ratios, and flavour decomposition of the lightest squark. Despite such optimistic conditions, the interpretation of the obtained SDDR using the empirical Jeffrey scale [197] leads to "moderate" evidence against the $SU(5)$ for the case of the counter-example, while the test remains inconclusive for the simulated $SU(5)$ case [195].

On the one hand, this example shows that Bayesian statistics can provide helpful information in questions related to model differenciation. On the other hand, it also shows that such a test has to rely on specific observables, which are sensitive to the quantity which is at the center of the hypothesis to be tested. The above example clearly has to be improved in this respect to be able to provide useful information in case of the observation of a squark-like state. For example, since the present asymmetry is defined within the trilinear coupling matrix A_u, processes of interest will be those involving Higgs bosons, since the trilinear matrix explicitely

appears in couplings of squarks to the physical Higgs bosons.

Generally, pursuing this research axis seems appealing, since ultimately, after studying simple cases such as the $SU(5)$ hypothesis, it will hopefully be possible to propose test quantities and procedures for other frameworks, typically based on the flavour structure within Grand Unification.

As it will also be discussed below, additional and complementary information can be obtained from *Machine Learning* methods. Especially in the present case of the differentiation of two models, such algorithms provide a powerful tool to efficiently classify data and define a seperation between two (or more) categories. In this respect, the identification of Grand Unified structures in a theory beyond the Standard Model based on TeV-scale observations seems an interesting and promising example for the application of Machine Learning techniques in particle phenomenology.

5.2 Lepton flavour violation and non-universality

While most of the research work presented in this manuscript has concerned the sector of quarks, flavour violation in the sector of leptons, and consequently the associated neutrino sector, bare an important potential in view of the search for new physics. Thanks to very clean signatures, measurements can be made in a more precise manner than in the hadronic sector, where the uncertainties, on both the experimental and theoretical side, are more important.

Moreover, recent experimental results, namely the so-called "flavour anomalies", related to the decays of B-mesons into D-mesons and kaons, namely the quantities

$$\begin{aligned} R_D &= \frac{\mathrm{BR}\left(B \to D\tau\nu\right)}{\mathrm{BR}\left(B \to D\ell\nu\right)}, & R_{D^*} &= \frac{\mathrm{BR}\left(B \to D^*\tau\nu\right)}{\mathrm{BR}\left(B \to D^*\ell\nu\right)}, \\ R_K &= \frac{\mathrm{BR}\left(B^+ \to K^+\mu^+\mu^-\right)}{\mathrm{BR}\left(B^+ \to K^+e^+e^-\right)}, & R_{K^*} &= \frac{\mathrm{BR}\left(B^0 \to K^{*0}\mu^+\mu^-\right)}{\mathrm{BR}\left(B^0 \to K^{*0}e^+e^-\right)}. \end{aligned} \tag{5.7}$$

More precisely, recent data suggest that [35]

$$\begin{aligned} R_K\big|_{q^2\in[0.045;1.1]\ \mathrm{GeV}^2} &= 0.66^{+0.11}_{-0.08}, & R_K\big|_{q^2\in[1.1;6.0]\ \mathrm{GeV}^2} &= 0.69^{+0.12}_{-0.09}, \\ R_{K^*}\big|_{q^2\in[1.0;6.0]\ \mathrm{GeV}^2} &= 0.74^{+0.10}_{-0.08}, \end{aligned} \tag{5.8}$$

at the 90% confidence level, which deviate from the Standard Model prediction which is unity (up to theory uncertainties) by about two to three standard deviations. Even more important, experimental data suggests [198]

$$R_D = 0.407 \pm 0.046, \qquad R_{D^*} = 0.304 \pm 0.07, \tag{5.9}$$

at the 90% confidence level, which differs from the Standard Model value by about four standard deviations. Moreover, the data points towards lepton flavour non-universality, which is contrary to the Standard Model description.

In addition, tensions persist between the Standard Model prediction and the experimentally observed values of the anomalous magnetic moments of the muon (see Table 2.1), and since recently potentially also the electron appearing via recent measurements of the fine-structure constant [199].

If the hints towards the abovementioned "flavour anomalies" are experimentally confirmed, the responsible physics cannot be explained within supersymmetric theories. It appears that, in the given context, frameworks including *leptoquarks* are particular appealing, allowing to

explain the observed "anomalies". Examples can be found in Refs. [200, 201, 202, 203, 204, 205, 206].

In this context, the possibility of lepton-flavour violation within non-supersymmetric models seems particularly interesting. In particular, the decay $\mu \to e\gamma$, which is experimentally determined to an extremely high precision, is a promising channel to detect new physics effects. Including related decay channels, and generalizing to all three lepton families, a detailed calculation of new physics contribution to the decays

$$\ell_i \to \ell_j \gamma\,, \qquad \ell_i \to \ell_j \gamma\gamma\,, \qquad \ell_i \to \ell_j \ell_k \bar{\ell}_k \tag{5.10}$$

will be a suitable starting point in order to examine appropriate models such as, e.g., extensions of the Standard Model including viable candidates for dark matter while at the same time allowing the radiative generation of neutrino masses and thus introducing lepton flavour violation. A classification of such models can be found in Ref. [191].

Performing a generic calculation of these decays will also allow to derive the new physics amplitudes to the anomalous magnetic moments of the leptons. This point is important because of two reasons: First, the experimental indications towards a tension with the Standard Model predictions, and second, the fact that no dedicated computational tool seems to be available allowing to perform a numerical calculation of the respective new physics contributions. Performing the associated calculation in a most generic manner, and implementing the associated numerical code in a modular way, will allow to apply the calculation to a large class of Standard Model extensions featuring lepton flavour violation.

5.3 Machine Learning in particle phenomenology

At the level of the more general view of new physics studies, it is important to remember that indications towards physics beyond the Standard Model arise from several independent directions, the most convincing ones relating to flavour physics, astroparticle physics, and cosmology. At the same time, collider searches remain the most important direct tool to access new physics. In addition, measuring variables related to Standard Model processes at collider experiments allows to obtain additional information on the impact of new physics parameters, e.g., through loop corrections to the processes under consideration.

Consequently, analysing and constraining new physics models requires the combination of a potentially large number of free parameters with the plethora of experimentally available data and constraints. Performing such a task in an efficient way is highly challenging on the technical and computational level. It is therefore of high importance to develop and exploit novel technologies, which allow efficient analyses of new physics models.

I therefore intend to explore the possibilities of using machine-learning techniques in phenomenological studies and in particular in the analyses of new physics models. While such methods already find applications in experimental analyses, see, e.g., Refs. [207, 208], and more recently in the field of astroparticle physics [209] and cosmology [210], they seem underexplored in the community of high-energy phenomenology.

In Secs. 3.3 and 3.4, first steps in this direction have been undertaken in order to access the flavour structure of an observed squark-like state at the Large Hadron Collider, see also Ref. [111]. While the proposed analysis remains rather simple and relies on rather optimistic assumptions, it clearly illustrates the power of the employed multi-variate analysis technique. It seems that methods relying on machine-learning algorithms are more powerful than, e.g., likelihood fits or Bayesian statistics, especially when it comes to handling large sets of observables or data. Moreover, they are complementary to other methods since they allow to efficiently classify the data, e.g., with respect to a certain number of observables or constraints, and will therefore be very useful in questions related to the distinction of different frameworks beyond

the Standard Model. As several new physics frameworks may lead to similar signatures at the LHC, such questions will be of utmost importance in case of the discovery of a new state.

However, several subtleties have to be addressed and understood in order to allow an efficient use of such techniques. First, different implementations of machine-learning based methods have to be scrutinized and compared in order to identify the techniques matching the different problems and questions arising in particle phenomenology. Second, and more important, the treatment of uncertainties has to be studied in highest detail. Third, the physics interpretation of the obtained results will be an important aspect to be addressed. Also, complementary studies using the more "traditional" techniques of simple parameter studies or Bayesian statistics need to be pursued, as they provide complementary information and interpretation.

Generally speaking, I am convinced that machine-learning techniques clearly deserve their place in studies related to the phenomenology of physics beyond the Standard Model. Moreover, I believe that in the future such techniques will be more and more relevant and used, in all the different contexts coming within phenomenological studies. I therefore have submitted a project to the French *A*gence Nationale de Recherche (ANR) covering in part this direction.

5.4 Non-standard signatures of new physics at colliders

Despite the extensive and extremely well-driven search for new physics at the LHC, and against the theory arguments that new physics should manifest at energy scales of a few TeV, no direct evidence for states beyond the Standard Model has been observed so far. The corresponding null results are presented in terms of mass limits within various new physics frameworks. A possible and widely spread interpretation of these null results remains that the expected new states are simply too heavy to be produced at the LHC. An alternative is that the new states are in principle reachable at current colliders, but the applied search strategies, which often rely on simplifying assumptions, are not adapted to their specific experimental signatures, such that the new states escape detection.

This has been demonstrated in Chap. 3 of the present manuscript for the case of intergenerational squark mixing, based on the analysis published in Ref. [128]. The assumed top-charm mixing strongly decreases the limits on squark masses, which have been obtained by the ATLAS collaboration based on the Minimal Flavour Violation paradigm. As has been shown in Sec. 3.2, including additional search strategies, related to the non-minimal flavour mixing, will alleviate this issue [128].

The Large Hadron Collider currently being prepared for its Run-3, starting presumably in 2021 with a centre-of-momentum energy of $\sqrt{s} = 14$ TeV and, more important, increased luminosity, it is important and timely to continue the study of such "exotic" non-covered, but theoretically well motivated, signatures of new physics.

Performing an inventory of current search strategies, and identifying simplifying assumptions therein, will allow to set up a list of starting points for such analyses. This must include supersymmetric and non-supersymmetric frameworks. Special care has to be taken when considering the implemented decay patterns of states associated to new physics. This will allow to point out relevant final states and associated research strategies to be included in the experimental searches. The decay modes can in particular be altered when considering non-trivial mixing patterns within the model under consideration. Such mixing patterns are likely to be related to the flavour structure of the theory, and may thus be motivated from a Grand Unification perspective.

5.5 Precision calculations beyond the Standard Model

As already mentioned above, the experimental and observational precision is constantly increasing, at collider-based experiments, low-energy measurements, in direct and indirect dark matter searches, as well as in cosmological observations. In the light of these experimental improvements, it is crucial that the associated theory predictions also become more precise, as they are to be confronted to the observations in order to potentially identify new physics effects.

Including higher-order radiative corrections to a huge number of theory and phenomenological predictions is of utmost importance in the quest of understanding and identifying physics beyond the Standard Model. This has to include radiative corrections to both Standard Model predictions, which correspond to the "background" in this context, but also the the contributions of new states to the same obervables.

To give an example, since my Ph.D. thesis and as a founding member of the DM@NLO collaboration [211], I have been involved in the calculation of higher-order corrections to the annihilation cross-section of neutralino dark matter in the Minimal Supersymmetric Standard Model (MSSM) and their impact on the resulting prediction of the neutralino relic density. The numerical DM@NLO code is designed to work as an extension of publicly available tools such as micrOMEGAs [184, 185, 186, 187, 212, 188] or DarkSUSY [213].

The common result of different studies of neutralino pair annihilation [214, 215, 216, 217], neutralino-squark co-annihilation [218, 219], and squark pair-annihilation [220] is that the impact of corrections of order α_s is more important than the current uncertainty on the relic density given by the Planck collaboration [48]. This clearly shows the importance of precision calculations when it comes to confronting a prediction with experimental data, or inversely extracting model parameters from observation.

Moreover, performing higher-order corrections also provides a way of estimating the theory uncertainty of the prediction, which is introduced by the choice of the renormalization scheme and the renormalization scale. For the above example, the analysis of the uncertainty has shown that, even at the one-loop level, the uncertainty of the predicted neutralino relic density cannot always meet the observational one [221]. Finally, the obtained results have been applied to evaluate the impact of the radiative corrections in the context of direct dark matter detection, i.e. for the scattering of a neutralino off a nucleus [222].

While the numerical implementation of the DM@NLO code is currently limited to neutralino dark matter in the Minimal Supersymmetric Standard Model, the question of correcting the dark matter annihilation cross-section in order to obtain a more precise prediction of the relic density is valid in any new physics model. We are currently implementing the last topologies associated to the pair-annihilation of scalar particles, e.g., the stops in the MSSM. Once this step is completed, all necessary topologies are represented in the numerical implementation. This will allow to generalize the implementation such that it can be applied to any other dark matter model.

In the implementation of a new model into the present DM@NLO framework, special care will need to be taken when defining the renormalization scheme. In particular, in models where co-annihilation can be sizeable, an adequate treatment of the involved masses is of utmost importance. Moreover, an efficient treatment of infrared singularities has to be implemented. While currently, the implementation in DM@NLO relies on phase-space slicing [223] and dipole subtraction à la Catani-Seymour [224, 225], it turns out that a more adequat solution would be the so-called Frixione-Kunst-Signer (FKS) subtraction scheme [226, 227].

Finally, let me mention that, while the DM@NLO projects focusses on corrections of order α_s, also electroweak corrections may be relevant in the given context. These corrections can be computed using the SloopS framework, which aims at automatizing the calculation at the one-loop level in a given renormalization scheme. Applications to the MSSM [228, 229, 230, 231,

232] have shown that the impact of electroweak corrections can be equally sizeable, depending on the region of parameter space. However, it turns out that in certain cases there is a rather important dependence on the renormalization scheme, which makes the exploitation of the results somewhat difficult.

As an ultimate goal, it will be interesting to provide a tool including both strong and electroweak corrections in the context of dark matter, not only for the relic density, but also for direct and indirect detection.

Bibliography

[1] S. L. Glashow. "Partial Symmetries of Weak Interactions". *Nucl. Phys.* 22 (1961), pp. 579–588. DOI: 10.1016/0029-5582(61)90469-2.

[2] S. Weinberg. "A Model of Leptons". *Phys. Rev. Lett.* 19 (1967), pp. 1264–1266. DOI: 10.1103/PhysRevLett.19.1264.

[3] S. L. Glashow, J. Iliopoulos, and L. Maiani. "Weak Interactions with Lepton-Hadron Symmetry". *Phys. Rev.* D2 (1970), pp. 1285–1292. DOI: 10.1103/PhysRevD.2.1285.

[4] S. Weinberg. "Effects of a neutral intermediate boson in semileptonic processes". *Phys. Rev.* D5 (1972), pp. 1412–1417. DOI: 10.1103/PhysRevD.5.1412.

[5] D. J. Gross and F. Wilczek. "Asymptotically Free Gauge Theories 1". *Phys. Rev.* D8 (1973), pp. 3633–3652. DOI: 10.1103/PhysRevD.8.3633.

[6] D. J. Gross and F. Wilczek. "Asymptotically Free Gauge Theories 2". *Phys. Rev.* D9 (1974), pp. 980–993. DOI: 10.1103/PhysRevD.9.980.

[7] H. D. Politzer. "Asymptotic Freedom: An Approach to Strong Interactions". *Phys. Rept.* 14 (1974), pp. 129–180. DOI: 10.1016/0370-1573(74)90014-3.

[8] B. Pontecorvo. "Mesonium and anti-mesonium". *Sov. Phys. JETP* 6 (1957). [Zh. Eksp. Teor. Fiz.33,549(1957)], p. 429.

[9] B. Pontecorvo. "Inverse beta processes and nonconservation of lepton charge". *Sov. Phys. JETP* 7 (1958). [Zh. Eksp. Teor. Fiz.34,247(1957)], pp. 172–173.

[10] Z. Maki, M. Nakagawa, and S. Sakata. "Remarks on the unified model of elementary particles". *Prog. Theor. Phys.* 28 (1962), pp. 870–880. DOI: 10.1143/PTP.28.870.

[11] B. Pontecorvo. "Neutrino Experiments and the Problem of Conservation of Leptonic Charge". *Sov. Phys. JETP* 26 (1968). [Zh. Eksp. Teor. Fiz.53,1717(1967)], pp. 984–988.

[12] Y. Fukuda et al. "Evidence for oscillation of atmospheric neutrinos". *Phys. Rev. Lett.* 81 (1998), pp. 1562–1567. DOI: 10.1103/PhysRevLett.81.1562. arXiv: hep-ex/9807003 [hep-ex].

[13] A. Aguilar-Arevalo et al. "Evidence for neutrino oscillations from the observation of anti-neutrino(electron) appearance in a anti-neutrino(muon) beam". *Phys. Rev.* D64 (2001), p. 112007. DOI: 10.1103/PhysRevD.64.112007. arXiv: hep-ex/0104049 [hep-ex].

[14] Q. R. Ahmad et al. "Direct evidence for neutrino flavor transformation from neutral current interactions in the Sudbury Neutrino Observatory". *Phys. Rev. Lett.* 89 (2002), p. 011301. DOI: 10.1103/PhysRevLett.89.011301. arXiv: nucl-ex/0204008 [nucl-ex].

[15] K. Eguchi et al. "First results from KamLAND: Evidence for reactor anti-neutrino disappearance". *Phys. Rev. Lett.* 90 (2003), p. 021802. DOI: 10.1103/PhysRevLett.90.021802. arXiv: hep-ex/0212021 [hep-ex].

[16] K. Abe et al. "Indication of Electron Neutrino Appearance from an Accelerator-produced Off-axis Muon Neutrino Beam". *Phys. Rev. Lett.* 107 (2011), p. 041801. DOI: 10.1103/PhysRevLett.107.041801. arXiv: 1106.2822 [hep-ex].

[17] Y. Abe et al. "Indication of Reactor $\bar{\nu}_e$ Disappearance in the Double Chooz Experiment". *Phys. Rev. Lett.* 108 (2012), p. 131801. DOI: 10.1103/PhysRevLett.108.131801. arXiv: 1112.6353 [hep-ex].

[18] F. P. An et al. "Observation of electron-antineutrino disappearance at Daya Bay". *Phys. Rev. Lett.* 108 (2012), p. 171803. DOI: 10.1103/PhysRevLett.108.171803. arXiv: 1203.1669 [hep-ex].

[19] J. K. Ahn et al. "Observation of Reactor Electron Antineutrino Disappearance in the RENO Experiment". *Phys. Rev. Lett.* 108 (2012), p. 191802. DOI: 10.1103/PhysRevLett.108.191802. arXiv: 1204.0626 [hep-ex].

[20] Y. Abe et al. "Reactor electron antineutrino disappearance in the Double Chooz experiment". *Phys. Rev.* D86 (2012), p. 052008. DOI: 10.1103/PhysRevD.86.052008. arXiv: 1207.6632 [hep-ex].

[21] K. Abe et al. "Observation of Electron Neutrino Appearance in a Muon Neutrino Beam". *Phys. Rev. Lett.* 112 (2014), p. 061802. DOI: 10.1103/PhysRevLett.112.061802. arXiv: 1311.4750 [hep-ex].

[22] P. Adamson et al. "Constraints on Oscillation Parameters from ν_e Appearance and ν_μ Disappearance in NOvA". *Phys. Rev. Lett.* 118.23 (2017), p. 231801. DOI: 10.1103/PhysRevLett.118.231801. arXiv: 1703.03328 [hep-ex].

[23] P. W. Higgs. "Broken symmetries, massless particles and gauge fields". *Phys. Lett.* 12 (1964), pp. 132–133. DOI: 10.1016/0031-9163(64)91136-9.

[24] F. Englert and R. Brout. "Broken Symmetry and the Mass of Gauge Vector Mesons". *Phys. Rev. Lett.* 13 (1964), pp. 321–323. DOI: 10.1103/PhysRevLett.13.321.

[25] P. W. Higgs. "Broken Symmetries and the Masses of Gauge Bosons". *Phys. Rev. Lett.* 13 (1964), pp. 508–509. DOI: 10.1103/PhysRevLett.13.508.

[26] G. S. Guralnik, C. R. Hagen, and T. W. B. Kibble. "Global Conservation Laws and Massless Particles". *Phys. Rev. Lett.* 13 (1964), pp. 585–587. DOI: 10.1103/PhysRevLett.13.585.

[27] P. W. Higgs. "Spontaneous Symmetry Breakdown without Massless Bosons". *Phys. Rev.* 145 (1966), pp. 1156–1163. DOI: 10.1103/PhysRev.145.1156.

[28] T. W. B. Kibble. "Symmetry breaking in non-Abelian gauge theories". *Phys. Rev.* 155 (1967), pp. 1554–1561. DOI: 10.1103/PhysRev.155.1554.

[29] G. Aad et al. "Observation of a new particle in the search for the Standard Model Higgs boson with the ATLAS detector at the LHC". *Phys. Lett.* B716 (2012), pp. 1–29. DOI: 10.1016/j.physletb.2012.08.020. arXiv: 1207.7214 [hep-ex].

[30] S. Chatrchyan et al. "Observation of a new boson at a mass of 125 GeV with the CMS experiment at the LHC". *Phys. Lett.* B716 (2012), pp. 30–61. DOI: 10.1016/j.physletb.2012.08.021. arXiv: 1207.7235 [hep-ex].

[31] N. Cabibbo. "Unitary Symmetry and Leptonic Decays". *Phys. Rev. Lett.* 10 (1963), pp. 531–533. DOI: 10.1103/PhysRevLett.10.531.

[32] M. Kobayashi and T. Maskawa. "CP Violation in the Renormalizable Theory of Weak Interaction". *Prog. Theor. Phys.* 49 (1973), pp. 652–657. DOI: 10.1143/PTP.49.652.

[33] L. Wolfenstein. "Parametrization of the Kobayashi-Maskawa Matrix". *Phys. Rev. Lett.* 51 (1983), p. 1945. DOI: 10.1103/PhysRevLett.51.1945.

[34] J. Hardy and I. S. Towner. "$|V_{ud}|$ from nuclear β decays". *PoS* CKM2016 (2016), p. 028. DOI: 10.22323/1.291.0028.

[35] M. Tanabashi et al. "Review of Particle Physics". *Phys. Rev.* D98.3 (2018), p. 030001. DOI: 10.1103/PhysRevD.98.030001.

[36] A. Abdesselam et al. "Precise determination of the CKM matrix element $|V_{cb}|$ with $\bar{B}^0 \to D^{*+} \ell^- \bar{\nu}_\ell$ decays with hadronic tagging at Belle" (2017). arXiv: 1702.01521 [hep-ex].

[37] F. Zwicky. "Die Rotverschiebung von extragalaktischen Nebeln". *Helv. Phys. Acta* 6 (1933), pp. 110–127.

[38] V. C. Rubin and W. K. Ford Jr. "Rotation of the Andromeda Nebula from a Spectroscopic Survey of Emission Regions". *Astrophys. J.* 159 (1970), pp. 379–403. DOI: 10.1086/150317.

[39] V. C. Rubin, W. K. Ford Jr., and N. Thonnard. "Extended rotation curves of high-luminosity spiral galaxies. IV. Systematic dynamical properties, Sa through Sc". *Astrophys. J.* 225 (1978), pp. L107–L111. DOI: 10.1086/182804.

[40] A. H. Jaffe et al. "Cosmology from MAXIMA-1, BOOMERANG and COBE / DMR CMB observations". *Phys. Rev. Lett.* 86 (2001), pp. 3475–3479. DOI: 10.1103/PhysRevLett.86.3475. arXiv: astro-ph/0007333 [astro-ph].

[41] D. N. Spergel et al. "First year Wilkinson Microwave Anisotropy Probe (WMAP) observations: Determination of cosmological parameters". *Astrophys. J. Suppl.* 148 (2003), pp. 175–194. DOI: 10.1086/377226. arXiv: astro-ph/0302209 [astro-ph].

[42] D. N. Spergel et al. "Wilkinson Microwave Anisotropy Probe (WMAP) three year results: implications for cosmology". *Astrophys. J. Suppl.* 170 (2007), p. 377. DOI: 10.1086/513700. arXiv: astro-ph/0603449 [astro-ph].

[43] E. Komatsu et al. "Five-Year Wilkinson Microwave Anisotropy Probe (WMAP) Observations: Cosmological Interpretation". *Astrophys. J. Suppl.* 180 (2009), pp. 330–376. DOI: 10.1088/0067-0049/180/2/330. arXiv: 0803.0547 [astro-ph].

[44] E. Komatsu et al. "Seven-Year Wilkinson Microwave Anisotropy Probe (WMAP) Observations: Cosmological Interpretation". *Astrophys. J. Suppl.* 192 (2011), p. 18. DOI: 10.1088/0067-0049/192/2/18. arXiv: 1001.4538 [astro-ph.CO].

[45] G. Hinshaw et al. "Nine-Year Wilkinson Microwave Anisotropy Probe (WMAP) Observations: Cosmological Parameter Results". *Astrophys. J. Suppl.* 208 (2013), p. 19. DOI: 10.1088/0067-0049/208/2/19. arXiv: 1212.5226 [astro-ph.CO].

[46] P. A. R. Ade et al. "Planck 2013 results. XVI. Cosmological parameters". *Astron. Astrophys.* 571 (2014), A16. DOI: 10.1051/0004-6361/201321591. arXiv: 1303.5076 [astro-ph.CO].

[47] P. A. R. Ade et al. "Planck 2015 results. XIII. Cosmological parameters". *Astron. Astrophys.* 594 (2016), A13. DOI: 10.1051/0004-6361/201525830. arXiv: 1502.01589 [astro-ph.CO].

[48] N. Aghanim et al. "Planck 2018 results. VI. Cosmological parameters" (2018). arXiv: 1807.06209 [astro-ph.CO].

[49] J. McDonald. "Electroweak baryogenesis and dark matter via a gauge singlet scalar". *Phys. Lett.* B323 (1994), pp. 339–346. DOI: 10.1016/0370-2693(94)91229-7.

[50] J. McDonald. "Gauge singlet scalars as cold dark matter". *Phys. Rev.* D50 (1994), pp. 3637–3649. DOI: 10.1103/PhysRevD.50.3637. arXiv: hep-ph/0702143 [HEP-PH].

[51] C. P. Burgess, M. Pospelov, and T. ter Veldhuis. "The Minimal model of nonbaryonic dark matter: A Singlet scalar". *Nucl. Phys.* B619 (2001), pp. 709–728. DOI: 10.1016/S0550-3213(01)00513-2. arXiv: hep-ph/0011335 [hep-ph].

[52] N. G. Deshpande and E. Ma. "Pattern of Symmetry Breaking with Two Higgs Doublets". *Phys. Rev.* D18 (1978), p. 2574. DOI: 10.1103/PhysRevD.18.2574.

[53] A. Goudelis, B. Herrmann, and O. Stål. "Dark matter in the Inert Doublet Model after the discovery of a Higgs-like boson at the LHC". *JHEP* 1309 (2013), p. 106. DOI: 10.1007/JHEP09(2013)106. arXiv: 1303.3010 [hep-ph].

[54] J. Wess and B. Zumino. "A Lagrangian Model Invariant Under Supergauge Transformations". *Phys. Lett.* B49 (1974), p. 52. DOI: 10.1016/0370-2693(74)90578-4.

[55] J. Wess and B. Zumino. "Supergauge Transformations in Four-Dimensions". *Nucl. Phys.* B70 (1974), pp. 39–50. DOI: 10.1016/0550-3213(74)90355-1.

[56] P. Minkowski. "$\mu \to e\gamma$ at a Rate of One Out of 10^9 Muon Decays?" *Phys. Lett.* 67B (1977), pp. 421–428. DOI: 10.1016/0370-2693(77)90435-X.

[57] M. Gell-Mann, P. Ramond, and R. Slansky. "Complex Spinors and Unified Theories". *Conf. Proc.* C790927 (1979), pp. 315–321. arXiv: 1306.4669 [hep-th].

[58] T. Yanagida. "Horizontal Symmetry and Masses of Neutrinos". *Prog. Theor. Phys.* 64 (1980), p. 1103. DOI: 10.1143/PTP.64.1103.

[59] R. N. Mohapatra and G. Senjanovic. "Neutrino Mass and Spontaneous Parity Nonconservation". *Phys. Rev. Lett.* 44 (1980). [,231(1979)], p. 912. DOI: 10.1103/PhysRevLett.44.912.

[60] R. N. Mohapatra and G. Senjanovic. "Neutrino Masses and Mixings in Gauge Models with Spontaneous Parity Violation". *Phys. Rev.* D23 (1981), p. 165. DOI: 10.1103/PhysRevD.23.165.

[61] E. Ma. "Verifiable radiative seesaw mechanism of neutrino mass and dark matter". *Phys. Rev.* D73 (2006), p. 077301. DOI: 10.1103/PhysRevD.73.077301. arXiv: hep-ph/0601225 [hep-ph].

[62] S. Esch et al. "Lepton flavor violation and scalar dark matter in a radiative model of neutrino masses". *Eur. Phys. J.* C78.2 (2018), p. 88. DOI: 10.1140/epjc/s10052-018-5577-7. arXiv: 1602.05137 [hep-ph].

[63] S. Esch, M. Klasen, and C. E. Yaguna. "A singlet doublet dark matter model with radiative neutrino masses". *JHEP* 10 (2018), p. 055. DOI: 10.1007/JHEP10(2018)055. arXiv: 1804.03384 [hep-ph].

[64] I. Esteban et al. "Updated fit to three neutrino mixing: exploring the accelerator-reactor complementarity". *JHEP* 01 (2017), p. 087. DOI: 10.1007/JHEP01(2017)087. arXiv: 1611.01514 [hep-ph].

[65] G. D'Ambrosio et al. "Minimal flavor violation: An Effective field theory approach". *Nucl. Phys.* B645 (2002), pp. 155–187. DOI: 10.1016/S0550-3213(02)00836-2. arXiv: hep-ph/0207036 [hep-ph].

[66] S. P. Martin. "A Supersymmetry primer". *Adv. Ser. Direct. High Energy Phys.* 21 (2010), pp. 1–153. DOI: 10.1142/9789814307505_0001. arXiv: hep-ph/9709356 [hep-ph].

[67] M. Drees, R. Godbole, and P. Roy. *Theory and phenomenology of sparticles: An account of four-dimensional N=1 supersymmetry in high energy physics*. Hackensack, USA: World Scientific (2004) 555 p, 2004.

[68] H. P. Nilles. "Supersymmetry, Supergravity and Particle Physics". *Phys. Rept.* 110 (1984), pp. 1–162. DOI: 10.1016/0370-1573(84)90008-5.

[69] A. Djouadi, J.-L. Kneur, and G. Moultaka. "SuSpect: A Fortran code for the supersymmetric and Higgs particle spectrum in the MSSM". *Comput. Phys. Commun.* 176 (2007), pp. 426–455. DOI: 10.1016/j.cpc.2006.11.009. arXiv: hep-ph/0211331 [hep-ph].

[70] A. Djouadi. "The Anatomy of electro-weak symmetry breaking. II. The Higgs bosons in the minimal supersymmetric model". *Phys. Rept.* 459 (2008), pp. 1–241. DOI: 10.1016/j.physrep.2007.10.005. arXiv: hep-ph/0503173 [hep-ph].

[71] L. J. Hall, V. A. Kostelecky, and S. Raby. "New Flavor Violations in Supergravity Models". *Nucl. Phys.* B267 (1986), p. 415. DOI: 10.1016/0550-3213(86)90397-4.

[72] G. Bozzi et al. "Squark and gaugino hadroproduction and decays in non-minimal flavour violating supersymmetry". *Nucl. Phys.* B787 (2007), pp. 1–54. DOI: 10.1016/j.nuclphysb.2007.05.031. arXiv: arXiv:0704.1826 [hep-ph].

[73] B. Fuks, B. Herrmann, and M. Klasen. "Flavour Violation in Gauge-Mediated Supersymmetry Breaking Models: Experimental Constraints and Phenomenology at the LHC". *Nucl.Phys.* B810 (2009), pp. 266–299. DOI: 10.1016/j.nuclphysb.2008.11.020. arXiv: arXiv:0808.1104 [hep-ph].

[74] M. Bruhnke, B. Herrmann, and W. Porod. "Signatures of bosonic squark decays in non-minimally flavour-violating supersymmetry". *JHEP* 1009 (2010), p. 006. DOI: 10.1007/JHEP09(2010)006. arXiv: arXiv:1007.2100 [hep-ph].

[75] G. Bertone, D. Hooper, and J. Silk. "Particle dark matter: Evidence, candidates and constraints". *Phys. Rept.* 405 (2005), pp. 279–390. DOI: 10.1016/j.physrep.2004.08.031. arXiv: hep-ph/0404175 [hep-ph].

[76] J. Harz. "Supersymmetric QCD Corrections and Phenomenological Studies in Relation to Coannihilation of Dark Matter". PhD thesis. Universität Hamburg, 2013. URL: http://www-library.desy.de/cgi-bin/showprep.pl?thesis13-048.

[77] U. Amaldi, W. de Boer, and H. Fürstenau. "Comparison of grand unified theories with electroweak and strong coupling constants measured at LEP". *Phys. Lett.* B260 (1991), pp. 447–455. DOI: 10.1016/0370-2693(91)91641-8.

[78] J. Hisano et al. "Lepton flavor violation in the supersymmetric standard model with seesaw induced neutrino masses". *Phys. Lett.* B357 (1995), pp. 579–587. DOI: 10.1016/0370-2693(95)00954-J. arXiv: hep-ph/9501407 [hep-ph].

[79] Y. Grossman and H. E. Haber. "Sneutrino mixing phenomena". *Phys. Rev. Lett.* 78 (1997), pp. 3438–3441. DOI: 10.1103/PhysRevLett.78.3438. arXiv: hep-ph/9702421 [hep-ph].

[80] J. A. Casas and A. Ibarra. "Oscillating neutrinos and muon —> e, gamma". *Nucl. Phys.* B618 (2001), pp. 171–204. DOI: 10.1016/S0550-3213(01)00475-8. arXiv: hep-ph/0103065 [hep-ph].

[81] J. R. Ellis et al. "A New parametrization of the seesaw mechanism and applications in supersymmetric models". *Phys. Rev.* D66 (2002), p. 115013. DOI: 10.1103/PhysRevD.66.115013. arXiv: hep-ph/0206110 [hep-ph].

[82] A. Masiero, S. K. Vempati, and O. Vives. "Massive neutrinos and flavor violation". *New J. Phys.* 6 (2004), p. 202. DOI: 10.1088/1367-2630/6/1/202. arXiv: hep-ph/0407325 [hep-ph].

[83] E. Arganda et al. "Lepton flavor violating Higgs boson decays from massive seesaw neutrinos". *Phys. Rev.* D71 (2005), p. 035011. DOI: 10.1103/PhysRevD.71.035011. arXiv: hep-ph/0407302 [hep-ph].

[84] F. R. Joaquim and A. Rossi. "Gauge and Yukawa mediated supersymmetry breaking in the triplet seesaw scenario". *Phys. Rev. Lett.* 97 (2006), p. 181801. DOI: 10.1103/PhysRevLett.97.181801. arXiv: hep-ph/0604083 [hep-ph].

[85] F. R. Joaquim and A. Rossi. "Phenomenology of the triplet seesaw mechanism with Gauge and Yukawa mediation of SUSY breaking". *Nucl. Phys.* B765 (2007), pp. 71–117. DOI: 10.1016/j.nuclphysb.2006.11.030. arXiv: hep-ph/0607298 [hep-ph].

[86] J. R. Ellis and O. Lebedev. "The Seesaw with many right-handed neutrinos". *Phys. Lett.* B653 (2007), pp. 411–418. DOI: 10.1016/j.physletb.2007.08.031. arXiv: 0707.3419 [hep-ph].

[87] A. Dedes, H. E. Haber, and J. Rosiek. "Seesaw mechanism in the sneutrino sector and its consequences". *JHEP* 11 (2007), p. 059. DOI: 10.1088/1126-6708/2007/11/059. arXiv: 0707.3718 [hep-ph].

[88] K. De Causmaecker et al. "General squark flavour mixing: constraints, phenomenology and benchmarks". *JHEP* 11 (2015), p. 125. DOI: 10.1007/JHEP11(2015)125. arXiv: 1509.05414 [hep-ph].

[89] W. Porod. private communication.

[90] Y. Amhis et al. "Averages of b-hadron, c-hadron, and τ-lepton properties as of summer 2014" (2014). arXiv: 1412.7515 [hep-ex].

[91] J. P. Lees et al. "Measurement of the $B \to X_s \ell^+ \ell^-$ branching fraction and search for direct CP violation from a sum of exclusive final states". *Phys. Rev. Lett.* 112 (2014), p. 211802. DOI: 10.1103/PhysRevLett.112.211802. arXiv: 1312.5364 [hep-ex].

[92] R. Aaij et al. "Differential branching fraction and angular analysis of the decay $B^0 \to K^{*0}\mu^+\mu^-$". *JHEP* 08 (2013), p. 131. DOI: 10.1007/JHEP08(2013)131. arXiv: 1304.6325 [hep-ex].

[93] The LHCb Collaboration. "Angular analysis of the $B^0 \to K^{*0}\mu^+\mu^-$ decay" (2015).

[94] L. Di Luzio, M. Kirk, and A. Lenz. "Updated B_s-mixing constraints on new physics models for $b \to s\ell^+\ell^-$ anomalies". *Phys. Rev.* D97.9 (2018), p. 095035. DOI: 10.1103/PhysRevD.97.095035. arXiv: 1712.06572 [hep-ph].

[95] J. Brod and M. Gorbahn. "Next-to-Next-to-Leading-Order Charm-Quark Contribution to the CP Violation Parameter ϵ_K and ΔM_K". *Phys. Rev. Lett.* 108 (2012), p. 121801. DOI: 10.1103/PhysRevLett.108.121801. arXiv: 1108.2036 [hep-ph].

[96] B. Herrmann, M. Klasen, and Q. Le Boulc'h. "Impact of squark flavour violation on neutralino dark matter". *Phys.Rev.* D84 (2011), p. 095007. DOI: 10.1103/PhysRevD.84.095007. arXiv: arXiv:1106.6229 [hep-ph].

[97] D. Choudhury, R. Garani, and S. K. Vempati. "Flavored Co-annihilations". *JHEP* 06 (2012), p. 014. DOI: 10.1007/JHEP06(2012)014. arXiv: 1104.4467 [hep-ph].

[98] M. Artuso et al. "B, D and K decays". *Eur. Phys. J.* C57 (2008), pp. 309–492. DOI: 10.1140/epjc/s10052-008-0716-1. arXiv: 0801.1833 [hep-ph].

[99] S. Heinemeyer et al. "Electroweak precision observables in the MSSM with nonminimal flavor violation". *Eur. Phys. J.* C37 (2004), pp. 481–493. DOI: 10.1140/epjc/s2004-02006-1. arXiv: hep-ph/0403228 [hep-ph].

[100] T. Hurth and W. Porod. "Flavour violating squark and gluino decays". *JHEP* 0908 (2009), p. 087. DOI: 10.1088/1126-6708/2009/08/087. arXiv: 0904.4574 [hep-ph].

[101] A. Bartl et al. "Impact of squark generation mixing on the search for gluinos at LHC". *Phys. Lett.* B679 (2009), pp. 260–266. DOI: 10.1016/j.physletb.2009.07.050. arXiv: 0905.0132 [hep-ph].

[102] A. Bartl et al. "Impact of squark generation mixing on the search for squarks decaying into fermions at LHC". *Phys.Lett.* B698 (2011), pp. 380–388. DOI: 10.1016/j.physletb.2011.04.051. arXiv: arXiv:1007.5483 [hep-ph].

[103] A. Bartl et al. "Flavour violating gluino three-body decays at LHC". *Phys.Rev.* D84 (2011), p. 115026. DOI: 10.1103/PhysRevD.84.115026. arXiv: arXiv:1107.2775 [hep-ph].

[104] B. Fuks, B. Herrmann, and M. Klasen. "Phenomenology of anomaly-mediated supersymmetry breaking scenarios with non-minimal flavour violation". *Phys.Rev.* D86 (2012), p. 015002. DOI: 10.1103/PhysRevD.86.015002. arXiv: arXiv:1112.4838 [hep-ph].

[105] A. Bartl et al. "Flavour violating bosonic squark decays at LHC" (2012). arXiv: arXiv:1212.4688 [hep-ph].

[106] M. Blanke et al. "Flavoured Naturalness". *JHEP* 1306 (2013), p. 022. DOI: 10.1007/JHEP06(2013)022. arXiv: 1302.7232 [hep-ph].

[107] M. Blanke. "Squark flavour violation and naturalness at the LHC" (2013). arXiv: 1306.4497 [hep-ph].

[108] A. Bartl et al. "$h^0 \to c\bar{c}$ as a test case for quark flavor violation in the MSSM". *Phys. Rev.* D91.1 (2015), p. 015007. DOI: 10.1103/PhysRevD.91.015007. arXiv: 1411.2840 [hep-ph].

[109] H. Eberl et al. "The decays $h^0 \to b\bar{b}$ and $h^0 \to c\bar{c}$ in the light of the MSSM with quark flavour violation". *JHEP* 06 (2016), p. 143. DOI: 10.1007/JHEP06(2016)143. arXiv: 1604.02366 [hep-ph].

[110] H. Eberl, E. Ginina, and K. Hidaka. "Two-body decays of gluino at full one-loop level in the quark-flavour violating MSSM". *Eur. Phys. J.* C77.3 (2017), p. 189. DOI: 10.1140/epjc/s10052-017-4754-4. arXiv: 1702.00348 [hep-ph].

[111] J. Bernigaud and B. Herrmann. "First steps towards the reconstruction of the squark flavour structure". *SciPost Phys.* 6 (2019), p. 066. DOI: 10.21468/SciPostPhys.6.6.066. arXiv: 1809.04370 [hep-ph].

[112] M. Arana-Catania, S. Heinemeyer, and M. J. Herrero. "Updated Constraints on General Squark Flavor Mixing". *Phys. Rev.* D90.7 (2014), p. 075003. DOI: 10.1103/PhysRevD.90.075003. arXiv: 1405.6960 [hep-ph].

[113] K. Kowalska. "Phenomenology of SUSY with General Flavour Violation". *JHEP* 09 (2014), p. 139. DOI: 10.1007/JHEP09(2014)139. arXiv: 1406.0710 [hep-ph].

[114] G. Brooijmans et al. "Les Houches 2013: Physics at TeV Colliders: New Physics Working Group Report" (2014). arXiv: 1405.1617 [hep-ph].

[115] M. Ciuchini et al. "Soft SUSY breaking grand unification: Leptons versus quarks on the flavor playground". *Nucl. Phys.* B783 (2007), pp. 112–142. DOI: 10.1016/j.nuclphysb.2007.05.032. arXiv: hep-ph/0702144 [HEP-PH].

[116] A. A. Markov. *Extension of the limit theorems of probability theory to a sum of variables connected in a chain*. reprinted in Appendix B of: R. Howard, *Dynamic Probabilistic Systems, volume 1: Markov Chains*, John Wiley and Sons, 1971.

[117] N. Metropolis et al. "Equation of state calculations by fast computing machines". *J. Chem. Phys.* 21 (1953), pp. 1087–1092. DOI: 10.1063/1.1699114.

[118] W. K. Hastings. "Monte Carlo Sampling Methods Using Markov Chains and Their Applications". *Biometrika* 57 (1970), pp. 97–109. DOI: 10.1093/biomet/57.1.97.

[119] F. Mahmoudi. "SuperIso: A Program for calculating the isospin asymmetry of B —> K* gamma in the MSSM". *Comput. Phys. Commun.* 178 (2008), pp. 745–754. DOI: 10.1016/j.cpc.2007.12.006. arXiv: 0710.2067 [hep-ph].

[120] F. Mahmoudi. "SuperIso v2.3: A Program for calculating flavor physics observables in Supersymmetry". *Comput. Phys. Commun.* 180 (2009), pp. 1579–1613. DOI: 10.1016/j.cpc.2009.02.017. arXiv: 0808.3144 [hep-ph].

[121] W. Porod. "SPheno, a program for calculating supersymmetric spectra, SUSY particle decays and SUSY particle production at e^+e^- colliders". *Comput.Phys.Commun.* 153 (2003), pp. 275–315. DOI: 10.1016/S0010-4655(03)00222-4. arXiv: hep-ph/0301101 [hep-ph].

[122] W. Porod and F. Staub. "SPheno 3.1: Extensions including flavour, CP-phases and models beyond the MSSM". *Comput.Phys.Commun.* 183 (2012), pp. 2458–2469. DOI: 10.1016/j.cpc.2012.05.021. arXiv: 1104.1573 [hep-ph].

[123] F. Mahmoudi et al. "Flavour Les Houches Accord: Interfacing Flavour related Codes". *Comput. Phys. Commun.* 183 (2012), pp. 285–298. DOI: 10.1016/j.cpc.2011.10.006. arXiv: 1008.0762 [hep-ph].

[124] A. Gelman and D. B. Rubin. "Inference from Iterative Simulation Using Multiple Sequences". *Statist. Sci.* 7.4 (Nov. 1992), pp. 457–472. DOI: 10.1214/ss/1177011136. URL: http://dx.doi.org/10.1214/ss/1177011136.

[125] B. C. Allanach et al. "Precise determination of the neutral Higgs boson masses in the MSSM". *JHEP* 09 (2004), p. 044. DOI: 10.1088/1126-6708/2004/09/044. arXiv: hep-ph/0406166 [hep-ph].

[126] J. Alwall et al. "The automated computation of tree-level and next-to-leading order differential cross sections, and their matching to parton shower simulations". *JHEP* 07 (2014), p. 079. DOI: 10.1007/JHEP07(2014)079. arXiv: 1405.0301 [hep-ph].

[127] G. Brooijmans et al. "Les Houches 2017: Physics at TeV Colliders New Physics Working Group Report". *10th Les Houches Workshop on Physics at TeV Colliders (PhysTeV 2017) Les Houches, France, June 5-23, 2017*. 2018. arXiv: 1803.10379 [hep-ph]. URL: http://lss.fnal.gov/archive/2017/conf/fermilab-conf-17-664-ppd.pdf.

[128] A. Chakraborty et al. "Flavour-violating decays of mixed top-charm squarks at the LHC" (2018). arXiv: 1808.07488 [hep-ph].

[129] A. M. Sirunyan et al. "Search for new phenomena with the M_{T2} variable in the all-hadronic final state produced in proton-proton collisions at $\sqrt{s} = 13$ TeV". *Eur. Phys. J.* C77.10 (2017), p. 710. DOI: 10.1140/epjc/s10052-017-5267-x. arXiv: 1705.04650 [hep-ex].

[130] M. Aaboud et al. "Search for supersymmetry in final states with two same-sign or three leptons and jets using 36 fb^{-1} of $\sqrt{s} = 13$ TeV pp collision data with the ATLAS detector". *JHEP* 09 (2017), p. 084. DOI: 10.1007/JHEP09(2017)084. arXiv: 1706.03731 [hep-ex].

[131] A. M. Sirunyan et al. "Search for top squark pair production in pp collisions at $\sqrt{s} = 13$ TeV using single lepton events". *JHEP* 10 (2017), p. 019. DOI: 10.1007/JHEP10(2017)019. arXiv: 1706.04402 [hep-ex].

[132] A. M. Sirunyan et al. "Search for direct production of supersymmetric partners of the top quark in the all-jets final state in proton-proton collisions at $\sqrt{s} = 13$ TeV". *JHEP* 10 (2017), p. 005. DOI: 10.1007/JHEP10(2017)005. arXiv: 1707.03316 [hep-ex].

[133] A. M. Sirunyan et al. "Search for the pair production of third-generation squarks with two-body decays to a bottom or charm quark and a neutralino in proton–proton collisions at $\sqrt{s} = 13$ TeV". *Phys. Lett.* B778 (2018), pp. 263–291. DOI: 10.1016/j.physletb.2018.01.012. arXiv: 1707.07274 [hep-ex].

[134] M. Aaboud et al. "Search for direct top squark pair production in final states with two leptons in $\sqrt{s} = 13$ TeV pp collisions with the ATLAS detector". *Eur. Phys. J.* C77.12 (2017), p. 898. DOI: 10.1140/epjc/s10052-017-5445-x. arXiv: 1708.03247 [hep-ex].

[135] M. Aaboud et al. "Search for supersymmetry in events with b-tagged jets and missing transverse momentum in pp collisions at $\sqrt{s} = 13$ TeV with the ATLAS detector". *JHEP* 11 (2017), p. 195. DOI: 10.1007/JHEP11(2017)195. arXiv: 1708.09266 [hep-ex].

[136] M. Aaboud et al. "Search for a scalar partner of the top quark in the jets plus missing transverse momentum final state at $\sqrt{s}$=13 TeV with the ATLAS detector". *JHEP* 12 (2017), p. 085. DOI: 10.1007/JHEP12(2017)085. arXiv: 1709.04183 [hep-ex].

[137] A. M. Sirunyan et al. "Search for supersymmetry in proton-proton collisions at 13 TeV using identified top quarks". *Phys. Rev.* D97.1 (2018), p. 012007. DOI: 10.1103/PhysRevD.97.012007. arXiv: 1710.11188 [hep-ex].

[138] A. M. Sirunyan et al. "Search for top squarks and dark matter particles in opposite-charge dilepton final states at $\sqrt{s} = 13$ TeV". *Phys. Rev.* D97.3 (2018), p. 032009. DOI: 10.1103/PhysRevD.97.032009. arXiv: 1711.00752 [hep-ex].

[139] M. Aaboud et al. "Search for dark matter and other new phenomena in events with an energetic jet and large missing transverse momentum using the ATLAS detector". *JHEP* 01 (2018), p. 126. DOI: 10.1007/JHEP01(2018)126. arXiv: 1711.03301 [hep-ex].

[140] M. Aaboud et al. "Search for top-squark pair production in final states with one lepton, jets, and missing transverse momentum using 36 fb^{-1} of $\sqrt{s} = 13$ TeV pp collision data with the ATLAS detector". *JHEP* 06 (2018), p. 108. DOI: 10.1007/JHEP06(2018)108. arXiv: 1711.11520 [hep-ex].

[141] M. Aaboud et al. "Search for squarks and gluinos in final states with jets and missing transverse momentum using 36 fb^{-1} of $\sqrt{s} = 13$ TeV pp collision data with the ATLAS detector". *Phys. Rev.* D97.11 (2018), p. 112001. DOI: 10.1103/PhysRevD.97.112001. arXiv: 1712.02332 [hep-ex].

[142] A. M. Sirunyan et al. "Search for supersymmetry in multijet events with missing transverse momentum in proton-proton collisions at 13 TeV". *Phys. Rev.* D96.3 (2017), p. 032003. DOI: 10.1103/PhysRevD.96.032003. arXiv: 1704.07781 [hep-ex].

[143] M. Aaboud et al. "Search for supersymmetry in final states with charm jets and missing transverse momentum in 13 TeV pp collisions with the ATLAS detector". *JHEP* 09 (2018), p. 050. DOI: 10.1007/JHEP09(2018)050. arXiv: 1805.01649 [hep-ex].

[144] *CMS Supersymmetry Physics Results*. 2018. URL: https://twiki.cern.ch/twiki/bin/view/CMSPublic/PhysicsResultsSUS.

[145] C. Borschensky et al. "Squark and gluino production cross sections in pp collisions at $\sqrt{s}$ = 13, 14, 33 and 100 TeV". *Eur. Phys. J.* C74.12 (2014), p. 3174. DOI: 10.1140/epjc/s10052-014-3174-y. arXiv: 1407.5066 [hep-ph].

[146] N. D. Christensen and C. Duhr. "FeynRules - Feynman rules made easy". *Comput. Phys. Commun.* 180 (2009), pp. 1614–1641. DOI: 10.1016/j.cpc.2009.02.018. arXiv: 0806.4194 [hep-ph].

[147] A. Alloul et al. "FeynRules 2.0 - A complete toolbox for tree-level phenomenology". *Comput. Phys. Commun.* 185 (2014), pp. 2250–2300. DOI: 10.1016/j.cpc.2014.04.012. arXiv: 1310.1921 [hep-ph].

[148] C. Degrande et al. "UFO - The Universal FeynRules Output". *Comput. Phys. Commun.* 183 (2012), pp. 1201–1214. DOI: 10.1016/j.cpc.2012.01.022. arXiv: 1108.2040 [hep-ph].

[149] R. D. Ball et al. "Parton distributions for the LHC Run II". *JHEP* 04 (2015), p. 040. DOI: 10.1007/JHEP04(2015)040. arXiv: 1410.8849 [hep-ph].

[150] L. Lönnblad and S. Prestel. "Matching Tree-Level Matrix Elements with Interleaved Showers". *JHEP* 03 (2012), p. 019. DOI: 10.1007/JHEP03(2012)019. arXiv: 1109.4829 [hep-ph].

[151] T. Sjöstrand et al. "An Introduction to PYTHIA 8.2". *Comput. Phys. Commun.* 191 (2015), pp. 159–177. DOI: 10.1016/j.cpc.2015.01.024. arXiv: 1410.3012 [hep-ph].

[152] S. Alioli et al. "A general framework for implementing NLO calculations in shower Monte Carlo programs: the POWHEG BOX". *JHEP* 06 (2010), p. 043. DOI: 10.1007/JHEP06(2010)043. arXiv: 1002.2581 [hep-ph].

[153] M. Cacciari, G. P. Salam, and G. Soyez. "The Anti-k(t) jet clustering algorithm". *JHEP* 04 (2008), p. 063. DOI: 10.1088/1126-6708/2008/04/063. arXiv: 0802.1189 [hep-ph].

[154] M. Cacciari, G. P. Salam, and G. Soyez. "FastJet User Manual". *Eur. Phys. J.* C72 (2012), p. 1896. DOI: 10.1140/epjc/s10052-012-1896-2. arXiv: 1111.6097 [hep-ph].

[155] J. de Favereau et al. "DELPHES 3, A modular framework for fast simulation of a generic collider experiment". *JHEP* 02 (2014), p. 057. DOI: 10.1007/JHEP02(2014)057. arXiv: 1307.6346 [hep-ex].

[156] *The ATLAS Experiment at the CERN Large Hadron Collider*. 2008, S08003. DOI: 10.1088/1748-0221/3/08/S08003.

[157] *Expected Performance of the ATLAS Experiment - Detector, Trigger and Physics*. CERN-OPEN-2008-020. 2009. arXiv: 0901.0512 [hep-ex].

[158] P. Pani and G. Polesello. "Dark matter production in association with a single top-quark at the LHC in a two-Higgs-doublet model with a pseudoscalar mediator". *Phys. Dark Univ.* 21 (2018), pp. 8–15. DOI: 10.1016/j.dark.2018.04.006. arXiv: 1712.03874 [hep-ph].

[159] *Expected performance of the ATLAS b-tagging algorithms in Run-2*. ATL-PHYS-PUB-2015-022. 2015. URL: https://cds.cern.ch/record/2037697.

[160] *Optimisation and performance studies of the ATLAS b-tagging algorithms for the 2017-18 LHC run*. ATL-PHYS-PUB-2017-013. 2017. URL: https://cds.cern.ch/record/2273281.

[161] A. L. Read. "Presentation of search results: The CL(s) technique". *J. Phys.* G28 (2002). [,11(2002)], pp. 2693–2704. DOI: 10.1088/0954-3899/28/10/313.

[162] L. Moneta et al. "The RooStats Project". *PoS* ACAT2010 (2010), p. 057. arXiv: 1009.1003 [physics.data-an].

[163] A. Hocker et al. *TMVA - Toolkit for Multivariate Data Analysis with ROOT: Users guide. TMVA - Toolkit for Multivariate Data Analysis*. Tech. rep. physics/0703039. TMVA-v4 Users Guide: 135 pages, 19 figures, numerous code examples and references. Geneva: CERN, Mar. 2007. URL: https://cds.cern.ch/record/1019880.

[164] *Toolkit for Multivariate Data Analysis with* ROOT *(*TMVA*)*. https://root.cern/tmva.

[165] R. Brun and F. Rademakers. "ROOT: An object oriented data analysis framework". *Nucl. Instrum. Meth.* A389 (1997), pp. 81–86. DOI: 10.1016/S0168-9002(97)00048-X.

[166] H. Georgi and S. L. Glashow. "Unity of All Elementary Particle Forces". *Phys. Rev. Lett.* 32 (1974), pp. 438–441. DOI: 10.1103/PhysRevLett.32.438.

[167] H. Fritzsch and P. Minkowski. "Unified Interactions of Leptons and Hadrons". *Annals Phys.* 93 (1975), pp. 193–266. DOI: 10.1016/0003-4916(75)90211-0.

[168] M. Gell-Mann, P. Ramond, and R. Slansky. "Color Embeddings, Charge Assignments, and Proton Stability in Unified Gauge Theories". *Rev. Mod. Phys.* 50 (1978), p. 721. DOI: 10.1103/RevModPhys.50.721.

[169] R. Slansky. "Group Theory for Unified Model Building". *Phys. Rept.* 79 (1981), pp. 1–128. DOI: 10.1016/0370-1573(81)90092-2.

[170] S. Raby. "Searching for the Standard Model in the String Landscape: SUSY GUTs". *Rept. Prog. Phys.* 74 (2011), p. 036901. DOI: 10.1088/0034-4885/74/3/036901. arXiv: 1101.2457 [hep-ph].

[171] J. Bernigaud et al. "Non-minimal flavour violation in $A_4 \times SU(5)$ SUSY GUTs with smuon assisted dark matter" (2018). arXiv: 1812.07463 [hep-ph].

[172] I. K. Cooper, S. F. King, and C. Luhn. "SUSY SU(5) with singlet plus adjoint matter and A4 family symmetry". *Phys. Lett.* B690 (2010), pp. 396–402. DOI: 10.1016/j.physletb.2010.05.066. arXiv: 1004.3243 [hep-ph].

[173] I. K. Cooper, S. F. King, and C. Luhn. "A4xSU(5) SUSY GUT of Flavour with Trimaximal Neutrino Mixing". *JHEP* 06 (2012), p. 130. DOI: 10.1007/JHEP06(2012)130. arXiv: 1203.1324 [hep-ph].

[174] B. D. Callen and R. R. Volkas. "Large lepton mixing angles from a 4+1-dimensional $SU(5) \times A(4)$ domain-wall braneworld model". *Phys. Rev.* D86 (2012), p. 056007. DOI: 10.1103/PhysRevD.86.056007. arXiv: 1205.3617 [hep-ph].

[175] S. Antusch, S. F. King, and M. Spinrath. "Spontaneous CP violation in $A_4 \times SU(5)$ with Constrained Sequential Dominance 2". *Phys. Rev.* D87.9 (2013), p. 096018. DOI: 10.1103/PhysRevD.87.096018. arXiv: 1301.6764 [hep-ph].

[176] F. Björkeroth et al. "Towards a complete $A_4 \times SU(5)$ SUSY GUT". *JHEP* 06 (2015), p. 141. DOI: 10.1007/JHEP06(2015)141. arXiv: 1503.03306 [hep-ph].

[177] M. Dimou, S. F. King, and C. Luhn. "Approaching Minimal Flavour Violation from an $SU(5) \times S_4 \times U(1)$ SUSY GUT". *JHEP* 02 (2016), p. 118. DOI: 10.1007/JHEP02(2016)118. arXiv: 1511.07886 [hep-ph].

[178] G. Aad et al. "Search for direct production of charginos, neutralinos and sleptons in final states with two leptons and missing transverse momentum in pp collisions at $\sqrt{s} = 8$ TeV with the ATLAS detector". *JHEP* 05 (2014), p. 071. DOI: 10.1007/JHEP05(2014)071. arXiv: 1403.5294 [hep-ex].

[179] F. Staub. "SARAH" (2008). arXiv: 0806.0538 [hep-ph].

[180] F. Staub. "From Superpotential to Model Files for FeynArts and CalcHep/CompHep". *Comput. Phys. Commun.* 181 (2010), pp. 1077–1086. DOI: 10.1016/j.cpc.2010.01.011. arXiv: 0909.2863 [hep-ph].

[181] F. Staub. "Automatic Calculation of supersymmetric Renormalization Group Equations and Self Energies". *Comput. Phys. Commun.* 182 (2011), pp. 808–833. DOI: 10.1016/j.cpc.2010.11.030. arXiv: 1002.0840 [hep-ph].

[182] F. Staub. "SARAH 3.2: Dirac Gauginos, UFO output, and more". *Computer Physics Communications* 184 (2013), pp. 1792–1809. DOI: 10.1016/j.cpc.2013.02.019. arXiv: 1207.0906 [hep-ph].

[183] F. Staub. "SARAH 4: A tool for (not only SUSY) model builders". *Comput. Phys. Commun.* 185 (2014), pp. 1773–1790. DOI: 10.1016/j.cpc.2014.02.018. arXiv: 1309.7223 [hep-ph].

[184] G. Bélanger et al. "MicrOMEGAs: A Program for calculating the relic density in the MSSM". *Comput. Phys. Commun.* 149 (2002), pp. 103–120. DOI: 10.1016/S0010-4655(02)00596-9. arXiv: hep-ph/0112278 [hep-ph].

[185] G. Bélanger et al. "micrOMEGAs: Version 1.3". *Comput. Phys. Commun.* 174 (2006), pp. 577–604. DOI: 10.1016/j.cpc.2005.12.005. arXiv: hep-ph/0405253 [hep-ph].

[186] G. Bélanger et al. "MicrOMEGAs 2.0: A Program to calculate the relic density of dark matter in a generic model". *Comput. Phys. Commun.* 176 (2007), pp. 367–382. DOI: 10.1016/j.cpc.2006.11.008. arXiv: hep-ph/0607059 [hep-ph].

[187] G. Bélanger et al. "micrOMEGAs 2.0.7: A program to calculate the relic density of dark matter in a generic model". *Comput. Phys. Commun.* 177 (2007), pp. 894–895. DOI: 10.1016/j.cpc.2007.08.002.

[188] D. Barducci et al. "Collider limits on new physics within micrOMEGAs 4.3". *Comput. Phys. Commun.* 222 (2018), pp. 327–338. DOI: 10.1016/j.cpc.2017.08.028. arXiv: 1606.03834 [hep-ph].

[189] B. C. Allanach et al. "SUSY Les Houches Accord 2". *Comput. Phys. Commun.* 180 (2009), pp. 8–25. DOI: 10.1016/j.cpc.2008.08.004. arXiv: 0801.0045 [hep-ph].

[190] G. Bélanger et al. "Dilepton constraints in the Inert Doublet Model from Run 1 of the LHC". *Phys. Rev.* D91.11 (2015), p. 115011. DOI: 10.1103/PhysRevD.91.115011. arXiv: 1503.07367 [hep-ph].

[191] D. Restrepo, O. Zapata, and C. E. Yaguna. "Models with radiative neutrino masses and viable dark matter candidates". *JHEP* 11 (2013), p. 011. DOI: 10.1007/JHEP11(2013)011. arXiv: 1308.3655 [hep-ph].

[192] D. Ghosh, M. Nardecchia, and S. A. Renner. "Hint of Lepton Flavour Non-Universality in B Meson Decays". *JHEP* 12 (2014), p. 131. DOI: 10.1007/JHEP12(2014)131. arXiv: 1408.4097 [hep-ph].

[193] K. Abe et al. "Search for proton decay via $p \to e^+\pi^0$ and $p \to \mu^+\pi^0$ in 0.31 megaton·years exposure of the Super-Kamiokande water Cherenkov detector". *Phys. Rev.* D95.1 (2017), p. 012004. DOI: 10.1103/PhysRevD.95.012004. arXiv: 1610.03597 [hep-ex].

[194] S. Fichet, B. Herrmann, and Y. Stoll. "Tasting the $SU(5)$ nature of supersymmetry at the LHC". *JHEP* 05 (2015), p. 091. DOI: 10.1007/JHEP05(2015)091. arXiv: 1501.05307 [hep-ph].

[195] Y. Stoll. "New phenomenological tests for supersymmetric theories with $SU(5)$-like unification". Theses. Université Grenoble Alpes, Sept. 2015. URL: https://tel.archives-ouvertes.fr/tel-01292577.

[196] S. Fichet, B. Herrmann, and Y. Stoll. "A new flavour imprint of $SU(5)$-like Grand Unification and its LHC signatures". *Phys. Lett.* B742 (2015), pp. 69–73. DOI: 10.1016/j.physletb.2015.01.013. arXiv: 1403.3397 [hep-ph].

[197] H. Jeffreys. *The Theory of Probability*. Oxford Classic Texts in the Physical Sciences. 1939. ISBN: 9780198503682. URL: https://global.oup.com/academic/product/the-theory-of-probability-9780198503682?cc=au&lang=en&#.

[198] Y. Amhis et al. "Averages of b-hadron, c-hadron, and τ-lepton properties as of summer 2016". *Eur. Phys. J.* C77.12 (2017), p. 895. DOI: 10.1140/epjc/s10052-017-5058-4. arXiv: 1612.07233 [hep-ex].

[199] R. H. Parker et al. "Measurement of the fine-structure constant as a test of the Standard Model". *Science* 360 (2018), p. 191. DOI: 10.1126/science.aap7706. arXiv: 1812.04130 [physics.atom-ph].

[200] Y. Sakaki et al. "Testing leptoquark models in $\bar{B} \to D^{(*)}\tau\bar{\nu}$". *Phys. Rev.* D88.9 (2013), p. 094012. DOI: 10.1103/PhysRevD.88.094012. arXiv: 1309.0301 [hep-ph].

[201] M. Bauer and M. Neubert. "Minimal Leptoquark Explanation for the $R_{D^{(*)}}$, R_K , and $(g-2)_g$ Anomalies". *Phys. Rev. Lett.* 116.14 (2016), p. 141802. DOI: 10.1103/PhysRevLett.116.141802. arXiv: 1511.01900 [hep-ph].

[202] S. Fajfer and N. Košnik. "Vector leptoquark resolution of R_K and $R_{D^{(*)}}$ puzzles". *Phys. Lett.* B755 (2016), pp. 270–274. DOI: 10.1016/j.physletb.2016.02.018. arXiv: 1511.06024 [hep-ph].

[203] S. Sahoo, R. Mohanta, and A. K. Giri. "Explaining the R_K and $R_{D^{(*)}}$ anomalies with vector leptoquarks". *Phys. Rev.* D95.3 (2017), p. 035027. DOI: 10.1103/PhysRevD.95.035027. arXiv: 1609.04367 [hep-ph].

[204] D. Bečirević et al. "Leptoquark model to explain the B-physics anomalies, R_K and R_D". *Phys. Rev.* D94.11 (2016), p. 115021. DOI: 10.1103/PhysRevD.94.115021. arXiv: 1608.08501 [hep-ph].

[205] I. de Medeiros Varzielas and J. Talbert. "Simplified Models of Flavourful Leptoquarks" (2019). arXiv: 1901.10484 [hep-ph].

[206] C. Cornella, J. Fuentes-Martin, and G. Isidori. "Revisiting the vector leptoquark explanation of the B-physics anomalies" (2019). arXiv: 1903.11517 [hep-ph].

[207] M. Paganini, L. de Oliveira, and B. Nachman. "Accelerating Science with Generative Adversarial Networks: An Application to 3D Particle Showers in Multilayer Calorimeters". *Phys. Rev. Lett.* 120.4 (2018), p. 042003. DOI: 10.1103/PhysRevLett.120.042003. arXiv: 1705.02355 [hep-ex].

[208] K. Albertsson et al. "Machine Learning in High Energy Physics Community White Paper". *J. Phys. Conf. Ser.* 1085.2 (2018), p. 022008. DOI: 10.1088/1742-6596/1085/2/022008. arXiv: 1807.02876 [physics.comp-ph].

[209] F. Calore, P. D. Serpico, and B. Zaldivar. "Dark matter constraints from dwarf galaxies: a data-driven analysis". *JCAP* 1810.10 (2018), p. 029. DOI: 10.1088/1475-7516/2018/10/029. arXiv: 1803.05508 [astro-ph.HE].

[210] M. Ntampaka et al. "The Role of Machine Learning in the Next Decade of Cosmology" (2019). arXiv: 1902.10159 [astro-ph.IM].

[211] DM@NLO *project webpage*. URL: http://projects.hepforge.org/dmnlo.

[212] G. Bélanger et al. "micrOMEGAs 3: A program for calculating dark matter observables". *Comput. Phys. Commun.* 185 (2014), pp. 960–985. DOI: 10.1016/j.cpc.2013.10.016. arXiv: 1305.0237 [hep-ph].

[213] P. Gondolo et al. "DarkSUSY: Computing supersymmetric dark matter properties numerically". *JCAP* 0407 (2004), p. 008. DOI: 10.1088/1475-7516/2004/07/008. arXiv: astro-ph/0406204 [astro-ph].

[214] B. Herrmann and M. Klasen. "SUSY-QCD Corrections to Dark Matter Annihilation in the Higgs Funnel". *Phys. Rev.* D76 (2007), p. 117704. DOI: 10.1103/PhysRevD.76.117704. arXiv: 0709.0043 [hep-ph].

[215] B. Herrmann, M. Klasen, and K. Kovařík. "Neutralino Annihilation into Massive Quarks with SUSY-QCD Corrections". *Phys. Rev.* D79 (2009), p. 061701. DOI: 10.1103/PhysRevD.79.061701. arXiv: 0901.0481 [hep-ph].

[216] B. Herrmann, M. Klasen, and K. Kovařík. "SUSY-QCD effects on neutralino dark matter annihilation beyond scalar or gaugino mass unification". *Phys. Rev.* D80 (2009), p. 085025. DOI: 10.1103/PhysRevD.80.085025. arXiv: 0907.0030 [hep-ph].

[217] B. Herrmann et al. "One-loop corrections to gaugino (co)annihilation into quarks in the MSSM". *Phys. Rev.* D89.11 (2014), p. 114012. DOI: 10.1103/PhysRevD.89.114012. arXiv: 1404.2931 [hep-ph].

[218] J. Harz et al. "Neutralino-stop coannihilation into electroweak gauge and Higgs bosons at one loop". *Phys.Rev.* D87.5 (2013), p. 054031. DOI: 10.1103/PhysRevD.87.054031. arXiv: 1212.5241.

[219] J. Harz et al. "One-loop corrections to neutralino-stop coannihilation revisited". *Phys. Rev.* D91.3 (2015), p. 034028. DOI: 10.1103/PhysRevD.91.034028. arXiv: 1409.2898 [hep-ph].

[220] J. Harz et al. "SUSY-QCD corrections to stop annihilation into electroweak final states including Coulomb enhancement effects". *Phys. Rev.* D91.3 (2015), p. 034012. DOI: 10.1103/PhysRevD.91.034012. arXiv: 1410.8063 [hep-ph].

[221] J. Harz et al. "Theoretical uncertainty of the supersymmetric dark matter relic density from scheme and scale variations" (2016). arXiv: 1602.08103 [hep-ph].

[222] M. Klasen, K. Kovařík, and P. Steppeler. "SUSY-QCD corrections for direct detection of neutralino dark matter and correlations with relic density". *Phys. Rev.* D94.9 (2016), p. 095002. DOI: 10.1103/PhysRevD.94.095002. arXiv: 1607.06396 [hep-ph].

[223] B. W. Harris and J. F. Owens. "The Two cutoff phase space slicing method". *Phys. Rev.* D65 (2002), p. 094032. DOI: 10.1103/PhysRevD.65.094032. arXiv: hep-ph/0102128 [hep-ph].

[224] S. Catani and M. H. Seymour. "The Dipole formalism for the calculation of QCD jet cross-sections at next-to-leading order". *Phys. Lett.* B378 (1996), pp. 287–301. DOI: 10.1016/0370-2693(96)00425-X. arXiv: hep-ph/9602277 [hep-ph].

[225] S. Catani et al. "The Dipole formalism for next-to-leading order QCD calculations with massive partons". *Nucl. Phys.* B627 (2002), pp. 189–265. DOI: 10.1016/S0550-3213(02)00098-6. arXiv: hep-ph/0201036 [hep-ph].

[226] S. Frixione, Z. Kunszt, and A. Signer. "Three jet cross-sections to next-to-leading order". *Nucl. Phys.* B467 (1996), pp. 399–442. DOI: 10.1016/0550-3213(96)00110-1. arXiv: hep-ph/9512328 [hep-ph].

[227] S. Frixione. "A General approach to jet cross-sections in QCD". *Nucl. Phys.* B507 (1997), pp. 295–314. DOI: 10.1016/S0550-3213(97)00574-9. arXiv: hep-ph/9706545 [hep-ph].

[228] F. Boudjema, A. Semenov, and D. Temes. "Self-annihilation of the neutralino dark matter into two photons or a Z and a photon in the MSSM". *Phys. Rev.* D72 (2005), p. 055024. DOI: 10.1103/PhysRevD.72.055024. arXiv: hep-ph/0507127 [hep-ph].

[229] N. Baro, F. Boudjema, and A. Semenov. "Full one-loop corrections to the relic density in the MSSM: A Few examples". *Phys. Lett.* B660 (2008), pp. 550–560. DOI: 10.1016/j.physletb.2008.01.031. arXiv: 0710.1821 [hep-ph].

[230] N. Baro, F. Boudjema, and A. Semenov. "Automatised full one-loop renormalisation of the MSSM. I. The Higgs sector, the issue of tan(beta) and gauge invariance". *Phys. Rev.* D78 (2008), p. 115003. DOI: 10.1103/PhysRevD.78.115003. arXiv: 0807.4668 [hep-ph].

[231] N. Baro et al. "Relic density at one-loop with gauge boson pair production". *Phys. Rev.* D81 (2010), p. 015005. DOI: 10.1103/PhysRevD.81.015005. arXiv: 0910.3293 [hep-ph].

[232] N. Baro and F. Boudjema. "Automatised full one-loop renormalisation of the MSSM II: The chargino-neutralino sector, the sfermion sector and some applications". *Phys. Rev.* D80 (2009), p. 076010. DOI: 10.1103/PhysRevD.80.076010. arXiv: 0906.1665 [hep-ph].